

**Advanced Controller Designs for Head Positioning and
Tension Regulation in Tape Drive Systems**

by

Hua Zhong

B.A., Tsinghua University, China 1999

M.S., University of Colorado Boulder, 2001

A thesis submitted to the
Faculty of the Graduate School of the
University of Colorado in partial fulfillment
of the requirements for the degree of
Doctor of Philosophy

Department of Electrical, Computer, and Energy Engineering

2014

This thesis entitled:
Advanced Controller Designs for Head Positioning and Tension Regulation in Tape Drive Systems
written by Hua Zhong
has been approved for the Department of Electrical, Computer, and Energy Engineering

Lucy Y. Pao

Dr. Mark Watson

Date _____

The final copy of this thesis has been examined by the signatories, and we find that both the content and the form meet acceptable presentation standards of scholarly work in the above mentioned discipline.

Zhong, Hua (Ph.D., Electrical, Computer, and Energy Engineering)

Advanced Controller Designs for Head Positioning and Tension Regulation in Tape Drive Systems

Thesis directed by Prof. Lucy Y. Pao

High density digital tape systems provide a cost-efficient and reliable solution for massive data backup. To maintain a competitive position against other data storage technologies, the tape industry aims to enable higher track densities and shorter data access time. The servomechanisms of the tape transport system and the head positioning system need to be improved for these purposes. This thesis investigates combined feedforward and feedback control in the tape transport dynamics and the head actuator, respectively. As the tape winds from one reel to the other, the reel radii vary due to the winding of the tape and the reel runouts. These variations can cause tension errors. As the tape is very thin, the variations between two consecutive revolutions can be considered negligible. A feedforward-inspired control scheme is developed to take into account the time-varying radius to reduce tape tension error caused by the variations in radii. In order to better align the write/read head with the desired data track, a combined feedforward/feedback control scheme to improve the tape head positioning servo system in the presence of lateral tape motion is also developed. Approximate dynamic inversion techniques and model matching methods are investigated to design the feedforward controller. The feedforward control is computed based upon an estimate of the lateral tape motion displacements (LTMDs) at the head that is calculated using measurements of the upstream and downstream lateral tape motion displacements near the head. To find the correlation between successive LTMDs, linear and polynomial regression methods are first studied. The nonlinear partial differential equation modeling tape motion in the lateral direction is then explored to solve the displacements for a short segment of tape surrounding the head using measurements of the upstream and downstream displacements as boundary conditions. The equation is discretized in the spatial domain using the finite element method (FEM) and integrated using the Wilson theta approximation. Performance and effectiveness of the controllers

are demonstrated in simulations. Feasibility analysis of implementing the feedforward controller on an actual tape drive is also conducted.

Acknowledgements

Foremost, I would like to thank my advisor Professor Lucy Pao for her continuous support and guidance throughout this thesis research. I am extremely grateful for her contributions of time, ideas, and funding to make my Ph.D. experience possible. Her passion, enthusiasm, and dedication toward her work, students, and family are supreme. She is a role model in both research and personal life. I will forever appreciate the opportunity I have had to be her student.

I would like to thank Dr. Mark Watson for his tremendous support of this project. As the industry mentor, he does not only provide advice on the research but also plays a key role to fund this project.

I also thank the professors who are kind enough to serve on my thesis committee: Professor Eric Frew, Professor Dale Lawrence, and Professor Andrew Pleszkun.

Finally, I thank the Information Storage Industry Consortium, Oracle Corporation, and the National Science Foundation for funding my research at various stages.

Contents

Chapter

1	Introduction	1
1.1	Tape Technology and Data Storage	1
1.2	Regulating Tape Tension	3
1.3	Positioning Tape Head	4
1.4	Contribution	5
1.5	Organization of the Thesis	8
2	Controller Designs to Attenuate Tension Errors in Tape Reel-to-reel Servo Systems	10
2.1	Tape Model and Tension Loop	10
2.1.1	Time-varying Reel Radii in Tape Systems	12
2.1.2	Tape Tension Loop	13
2.2	Adaptive Control Algorithm in Continuous-time Domain	15
2.3	Feedforward Control Algorithms in Discrete-time Domain	18
2.3.1	Time-varying Reference Input Filter	19
2.3.2	Control to Address Reel Eccentricities	20
2.4	Conclusions and Discussion	27
3	Feedforward Control Designs to Reduce Position Error in Tape Head Positioning Systems	29

3.1	Tape Head Dynamics Model and Lateral Tape Motion	29
3.1.1	Head Actuator Plant Model	29
3.1.2	Lateral Tape Motion	30
3.2	Feedback Control	33
3.2.1	Basic PID Controller	33
3.2.2	More Advanced Feedback Controller	34
3.3	Feedforward/Feedback Control Scheme	35
3.4	Feedforward Control Designs	35
3.4.1	Approximate Dynamic Inversion Techniques	37
3.4.2	Model Matching Methods	40
3.5	Simulation Results	46
3.5.1	Feedback Controller	46
3.5.2	Approximate Dynamic Inversion	48
3.5.3	H_2 -norm Model Matching	53
3.6	Conclusions and Discussion	60
4	Least Squares Algorithm to Estimate LTMD	61
4.1	Least Squares Algorithm	62
4.2	Prediction Performance	63
4.2.1	Synthesized LTMD Data	64
4.2.2	Actual LTMD Data	64
4.3	Implementation Feasibility	66
4.4	Polynomial Regression	68
4.5	Conclusions and Discussion	69
5	Partial Differential Equation to Solve for LTMD	70
5.1	LTM Model	70
5.2	Discretization in Spatial Domain - Finite Element Method	71

5.2.1	Meshing	72
5.2.2	Selecting Displacement Models	73
5.2.3	Deriving Elemental Matrices	76
5.2.4	Obtaining Global Matrices	76
5.2.5	Solving for Unknown Displacements	78
5.3	Numerical Integration - Wilson Theta Method	78
5.4	Simulation Results	80
5.4.1	Full Path Simulation	80
5.4.2	Simulation of a Short Segment of Tape	83
5.4.3	Combined Feedforward/Feedback Control	85
5.5	Conclusions and Discussion	86
6	Overall Conclusions and Future Work	89
	Bibliography	91

Tables**Table**

2.1	Tape system parameters for simulation	14
2.2	Magnitude of steady-state tension error (N)	28

Figures

Figure

1.1 Schematic of a reel-to-reel tape system. Diagram created using [39].	2
2.1 Lumped-parameter model of a tape system.	11
2.2 Decoupling algorithm for the tension loop and the velocity loop.	13
2.3 Reel eccentricity data is interpolated from an industry sample.	15
2.4 The time-varying tension control loop in continuous-time domain.	16
2.5 C_A is a time-varying controller that adapts the frequency ω_a and magnitude m_a to synthesize an input u_a whose plant response ideally is the additive inverse of the tension error.	16
2.6 The adapted magnitude and frequency follows that of the disturbance.	17
2.7 Block diagram of the tension loop in the discrete-time domain.	18
2.8 Tension error is essentially eliminated by the time-varying filter that addresses both nominal reel radius variations and reel runout.	20
2.9 The tension error is on the order of 10^{-3} N when R_k only addresses the nominal variations in the radius.	21
2.10 Nominal radius fixed (purely periodic system), reel runout unknown: the initial compensation input computed from tension errors in two revolutions reduces the error by three orders of magnitude.	23
2.11 The tension error is reduced by the initial compensation input sequence first and then grows as the tape winds.	24

2.12 A revolution is completed when the angular position of a sampling point crosses over that of the first sampling point in the same revolution.	25
2.13 The nominal radius varies and reel eccentricities are unknown. The compensation input is updated every revolution and the steady-state tension error is reduced by three orders of magnitude from 10^{-3} N to 10^{-6} N.	26
2.14 When the nominal radius is fixed, the steady-state tension error is effectively zero.	27
3.1 One of the zeros in the discrete tape head actuator model becomes non-minimum phase as the sampling frequency increases.	31
3.2 The tape head actuator model has two resonances and one NMP zero when the sampling frequency is at 10 KHz.	32
3.3 Lateral tape motion causes position error.	32
3.4 A typical head positioning system in a tape drive uses feedback control only.	33
3.5 Bode plots of the output sensitivity function of the closed-loop head positioning system with C_{PID} or C_R	34
3.6 Block diagram of the combined feedforward/feedback control scheme for a tape head positioning system.	35
3.7 The feedforward controller C_{ff} aims to reduce the position error caused by the lateral tape motion disturbance.	36
3.8 A feedback controller is included before the feedforward control is designed.	36
3.9 In this closed-loop inversion architecture, the feedforward controller is designed to be the (approximate) inversion of the output sensitivity function.	38
3.10 (a) The setup of the classic H_2 optimal control problem; (b) The model matching problem can be converted to an optimal control problem.	43
3.11 Amplitude spectrum of the first set of measured LTMD data near the head, Meas. 1. .	47
3.12 Amplitude spectrum of the second set of measured LTMD data near the head, Meas. 2. The tape is running at a higher speed than when Meas. 1 is taken.	47

3.13 Meas. 1: The REACT feedback controller is introduced at 2 second and it further reduces the RMS of the position error signal from $0.33 \mu\text{m}$ to $0.19 \mu\text{m}$	48
3.14 Meas. 2: Since the LTM data contains noticeable frequency content that is beyond the crossover frequency of the closed-loop, the position error is only reduced by a small proportion by the feedback controllers.	49
3.15 Meas. 1 data set: ZPETC feedforward controller reduces the position error to $10^{-1} \mu\text{m}$; 3 extra steps of delay are needed.	50
3.16 Meas. 1 data set: ZMETC feedforward controller requires 1 extra step of delay and reduces the position error to $10^{-1} \mu\text{m}$	50
3.17 Meas. 1 data set: the feedforward controller designed using the Taylor series approximation requires large feedforward control input and does not improve the disturbance rejection performance.	51
3.18 Meas. 2 data set: ZPETC feedforward controller.	52
3.19 Meas. 2 data set: ZMETC feedforward controller.	52
3.20 Meas. 2 data set: Taylor series approximation method.	53
3.21 The ZMETC feedforward controller reduces the disturbance by more than 80% when the gain and the zeros of the plant contains a 10% error.	54
3.22 The ZMETC feedforward controller improves disturbance rejection performance when the poles of the plant each contains no more than 1% error.	54
3.23 The feedforward controller is designed by the non-augmented H_2 model matching method and no penalty is imposed on the control input. The magnitude of the input current is on the order of 10 A.	55
3.24 The augmented model matching method limits the size of the feedforward control input. The position error is reduced by more than one order of magnitude.	56
3.25 With a longer preview period, the feedforward controller reduces the position error by two orders of magnitude and the size of the control input is on the order of 1 A. . .	57

3.26 The feedforward controller solved by the augmented model matching method still reduces the position error caused by LTM disturbance when the gain and the zeros of the plant each contains a 10% error.	57
3.27 The feedforward controller reduces the position error when the poles of the plant each contains no more than 1% error.	58
3.28 Meas. 2 data set: the feedforward controller reduces the position error by more than 1 order of magnitude while the feedforward input is restricted within the allowable range.	59
3.29 Simulation results of applying combined feedforward/feedback control scheme to Meas. 1 data set. The REACT feedback controller is designed to reduced the position error for this particular LTM data set. The feedforward controller further reduces position error by one order of magnitude.	59
4.1 Edge sensors can be placed near the head to measure upstream and downstream lateral tape displacements.	61
4.2 The performance of the prediction algorithm depends on M_t and k_p . From these results, $M_t = 100$ and $k_p = 10$ predicts \hat{w}_h 10 samples ahead of time reasonably well.	65
4.3 Actual upstream and downstream LTMD measurements from a tape drive system. The magnitude is normalized due to intellectual property protection reasons.	66
4.4 The NRMS of the prediction error w_{ed} decreases when M_t and k_p increase.	67
4.5 The required total number of floating point operations needed to solve the least squares problem with different combinations of M_t and k_p values.	68
5.1 The tape path is divided into N_e elements and has $N_e + 1$ nodes. The numbers on the top of the schematic represent the nodes and at the bottom represent the elements.	72
5.2 The tape path in the simulations include the source reel, the take-up reel, two head assemblies (labeled as H1 and H2 in the figure), and 5 rollers (labeled as R1, R2, R3, R4, R5).	73

5.3	Wilson Theta method assumes that the acceleration of the system varies linearly between two instants of time.	79
5.4	When the number of elements increases, the simulation is generally more accurate. .	81
5.5	The non-uniform mesh contains 130 elements.	82
5.6	Lateral displacements of the entire tape span for a duration of 0.1 seconds.	83
5.7	Successive LTMDs near the head.	84
5.8	Estimation error increases significantly once the number of elements between the head and the sensor exceeds 6.	85
5.9	Estimation error at the head by solving the equation of motion a short segment of tape around the head.	86
5.10	Estimation error of the LTMD at the head is about 8% of the actual data when the boundary conditions have a 10% distortion.	87
5.11	Estimation error of the LTMD at the head is about 15% of the actual data when the boundary conditions have a 20% distortion.	87
5.12	The feedforward controller designed using the H_2 model matching method is enabled at 0.4 sec. The input to the feedforward controller is the estimated LTMD at the head.	88

Chapter 1

Introduction

This chapter begins with an overview of tape storage systems followed by a brief introduction of the servomechanisms in a tape drive. Moreover, the motivation and contribution of this thesis are provided.

1.1 Tape Technology and Data Storage

High density digital tape storage systems face tough competition from other data storage technologies, especially hard disk drive (HDD) systems. Compared with hard disk drive storage, tape systems provide a data storage solution with lower media cost, less energy consumption, longer data life, and higher reliability, mostly due to the fact that the storage medium (the cartridge) and the read/write mechanism (the drive) are separated. The cartridge is removed from the drive once the data is recorded and no power is needed until it is loaded into a drive again. Unlike HDDs, mechanical failures of a drive do not result in data loss as the tape cartridges are removable and interchangeable. However, tape systems are surpassed by HDDs in storage density and data access time. The areal density of current tape technology is about $1\text{-}10 \text{ Gbit/in}^2$ and two orders of magnitude lower than that of HDDs. The nature of linear and sequential recording in tape storage limits the access time of data. Considering both the advantages and limitations, tape technology is still the most cost-effective and reliable data storage solution for long-term archiving and backup of large amounts of data.

Due to the explosion of digital data information, mass data archiving applications using tape

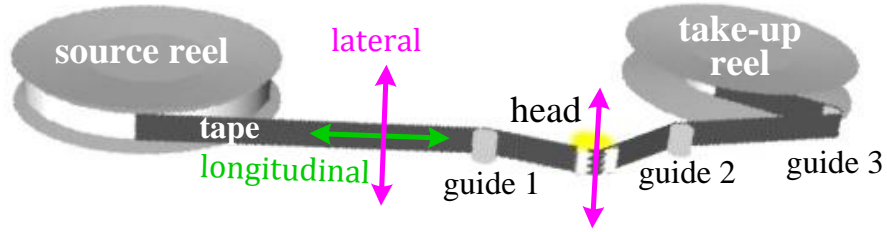


Figure 1.1: Schematic of a reel-to-reel tape system. Diagram created using [39].

storage systems are rapidly growing. These applications include satellite imagery storage, atmospheric model archiving, and consumer data records. Beyond traditional data backup applications, tape is also suited for other forms of applications such as streaming video where the data may be large and primarily sequential and cloud-based archive in which a small number of HDDs is used as the cache for the tape-based data repository. To retain a competitive position in the data storage business, the tape industry aims to increase areal data capacity. Recent studies indicate that improvements in technology may allow the tape areal density to reach the range of 100 Gb/in^2 [2] [12]. To achieve this target, better servomechanisms are necessary for both the tape reel-to-reel transportation and the head actuation.

The schematic in Fig. 1.1 illustrates an example of a reel-to-reel tape system [39]. The source reel and the take-up reel are driven by DC motors, respectively. The tape segment between the two tangential points of the reels is supported by a number of guiding rollers. Data is recorded in tracks parallel to the edges of the tape and each data track spans the entire length of the tape. When tape winds longitudinally from the source reel to the take-up reel, a voice coil motor moves the tape head assembly laterally across the width of the tape to align the head with the desired data track so as to read or write data to or from the tape.

There are two servo systems in the tape drive. The first one is the tape transport servo control, also known as the reel-to-reel control. This control system focuses on regulating the longitudinal velocity and tension of the tape at prescribed values. The other servo system, commonly known as

the track-following mechanism or head positioning control, adjusts the position of the read/write head assembly in the lateral direction so as to reduce the misalignment between the head and the desired track on the tape. These two servo systems operate independently. As techniques are being developed to increase the tape winding speed and decrease the thickness of the tape in order to achieve higher data transfer rates and larger data capacity, more advanced control techniques to regulate the tape tension are required. Increasing data track density on tape is a critical step to improve the areal storage density. The narrower track pitches necessitate an improved head positioning accuracy in the presence of lateral tape motion. This dissertation investigates advanced controller designs to improve the performance of these two independent servomechanisms, respectively.

1.2 Regulating Tape Tension

One of the main control objectives in tape reel-to-reel servo systems is to increase as much as possible the tape transport velocity while simultaneously regulating the tape tension. Thinner tape and faster winding speed make the tape more fragile and hence more sensitive to tension variations. More advanced control techniques to regulate the tension are needed.

While some work has been conducted on tension control in web-winding systems including tape systems, most of that work assumes: (A) the plant is a linear time-invariant (LTI) system and/or (B) the reels of the web-winding system are perfectly circular [3, 9, 19, 20, 42, 48]. Iterative learning control has been developed to compensate for reel eccentricities in coil-to-coil rolling processes that operate in a repetitive fashion [9]. Adaptive control has been explored to reject quasi-periodic tension disturbances in LTI web-winding systems [42, 48], where the disturbances are considered as either an input or an output disturbance. Tape systems are time-varying as the radii of both reels vary when the tape winds. Reel eccentricities due to non-perfectly circular reels aggravate the time-varying nature of the system. The adaptive control algorithm in [48] works for a plant that includes radius variations due to tape winding. However, the adaptation fails when reel eccentricities are included in the plant because the convergence speed of the adaptation loop is

much slower than the rate at which the eccentricities vary. Little research has been conducted on regulating tape tension in the time-varying tape system that includes variations in nominal radius and reel eccentricities.

1.3 Positioning Tape Head

Increasing track densities has been identified as a critical step to achieve the target areal density projected by the tape industry. Track density is defined as the number of data tracks per inch (TPI) laterally across the width of the tape. The current track density in a typical modern commercial tape system, where the tape is 0.5 inches wide, is about 5,000 TPI. The most recent tape industry roadmap [12] envisions that tape track densities must reach 53,000 TPI by 2022. The increase in track densities causes significant reduction in the width of the track pitch. To enable higher track densities and narrower track pitch, more precise positioning of the read/write assembly is needed. This requires further rejection of various disturbances that cause misalignment of the head with respect to the desired track. Lateral tape motion (LTM) is one of the major disturbances that must be further addressed [2][12]. The typical peak-to-peak amplitude of the lateral tape motion displacement (LTMD) in an operating tape system can be as large as $10 \mu\text{m}$ and the frequency can be above 1000 Hz [12][14][26].

Two different approaches have been investigated to reduce position error arising from LTM. The first approach tries to improve the hardware design to either reduce the lateral motion itself or improve the mechanism of the head assembly. Studies have been conducted to understand the correlations between guiding rollers and LTM. The behavior of a tape interacting with a guide is studied in [35] where results show that friction between the tape and the roller affects the lateral displacements of the tape. LTM is correlated with the axial roller runout in [25]. In [27], the effect of friction and other design parameters on the lateral motion of the tape moving over a stationary cylindrical roller is studied. Roller radius and tape wrapping angle are found to be the primary factors that effect LTM while the influences from tape velocity, tape thickness, and the nominal tape tension are secondary. Larger roller radius and/or larger tape wrapping angle increase the

contact length and friction force that consequently attenuate LTM at the cost of more severe tape wear.

The use of externally-pressurized porous air bearing guides and friction guiding are discussed in [14]. In [41], an active steering system that compensates the lateral tape motion by tilting the guides is described. A piezo-electric actuator that allows a higher bandwidth is prototyped in [15] to replace the conventional voice coil motor actuator. Flangeless rollers are discussed in [2] to eliminate the interaction between the roller flanges and the tape so as to reduce LTM. However, the LTM can increase as tape moves up and down without the constraint of the flanges. To implement these approaches in a tape system, some new hardware components need to be installed and often the tape transport path will be changed.

Rather than changing the tape transport path to reduce lateral tape motion directly, the second approach aims to reduce the effects of the LTM on the position error by improving the track-following performance of the head servo mechanism. The current tape head position servo systems typically use a proportional-integral-derivative (PID) feedback controller and the bandwidth of the closed-loop system is usually below the higher-frequency components in the lateral tape motion displacements. In [24], an H_∞ control framework is used to design the track-following controller for a flangeless tape path and a primitive feedforward control architecture is discussed.

1.4 Contribution

This thesis is motivated by the urgent need of the tape industry to improve the servomechanisms in tape drives. We investigate advanced controller designs that include feedforward control schemes for the tape servo systems in reel-to-reel control and the head positioning control, respectively. The issues addressed in the dissertation and the main contributions are listed below.

- (1) *A feedforward inspired control scheme to attenuate tape tension error caused by the psuedo-periodic reel eccentricities in the time-varying tape transport system.* The tape system is time-varying as tape winds from one reel to the other. The variations in the reel radii consist

of (i) the known nominal reel radii change due to tape winding and (ii) the unknown additive reel eccentricities as a result of non-circular reels. These variations introduce disturbances in the tape tension. A control scheme that takes into account the time-varying reel radius to regulate tape tension is developed. The known variations are taken into account by a time-varying feedforward filter to the reference input. The unknown reel eccentricities are addressed by investigating tension errors of previous revolutions. Since the tape is thin, the tension error caused by reel eccentricities can be considered as repetitive in two consecutive revolutions. The compensation input is first computed from the tension error from the previous revolutions and then carefully interpolated for the current revolution. To take into account the slowly time-varying period of the system, a new definition of one revolution is introduced. Simulation results with actual tape reel eccentricity data demonstrates that the time-varying feedforward filter leads to zero tension error if all the variations in reel radius are known, and the compensation scheme for unknown reel eccentricities reduces the tension error by three orders of magnitude. The algorithm can also be applied to regulate web tension in other web-winding processes.

- (2) *Feedforward combined with feedback control scheme to reduce the position error between the head and the track caused by lateral tape motion.* Higher track densities reduce the track pitch significantly and require the tape head servo system to position the head assembly more precisely. A combined feedforward/feedback control scheme to improve the tape head positioning servo system in the presence of lateral tape motion is developed. In this architecture, the feedback controller is designed to guarantee system stability and take into account the lower frequency components in the disturbances. To design the feedforward controller, a number of different methods including approximate dynamic inversion techniques and model matching methods are discussed, implemented, and compared. The solvability of the H_2 -norm model matching problem is discussed and a conclusion is drawn on the necessary and sufficient conditions of the problem to have a non-trivial solution when

the disturbance dynamics is a pure delay. Compared to using feedback-only control, the combined feedforward/feedback controller effectively reduces position error in the presence of LTM.

- (3) *Algorithms to predict the lateral tape motion displacement at the head.* The feedforward controller requires as its input an estimate of the lateral tape motion displacement (LTMD) at the head assembly. Numerical and analytic methods are explored to estimate the LTMD at the head from a history of upstream and downstream LTMD measurements adjacent to the head. A least squares algorithm is first developed under the assumption that the correlation between successive LTMDs is linear. To address the nonlinear relationship in the correlation, the partial differential equation of motion for the tape in the lateral direction of the entire tape path is studied. A method is then developed to solve the LTMDs for a short segment of tape near the head, given the knowledge of upstream and downstream LTMDs as the boundary conditions. The equation is discretized in the spatial domain using the finite element method and integrated in the time-domain using the Wilson-theta approximation. The dynamic boundary conditions at upstream and downstream locations are implemented using the penalty method. The solution of the lateral tape motion at the head is applied to the feedforward controller to align the head with the data track more precisely.

- (4) *Proof of concept of implementing feedforward combined with feedback controller in a tape drive.* A proof of concept of applying feedforward control to mitigate the position error in the presence of the lateral tape motion is demonstrated. The feedforward controller is designed by the model matching method and the LTMD at the head is estimated from the upstream and downstream LTMDs by solving the partial differential equations of lateral tape motion for a short segment of tape surrounding the head. In practice, optical edge sensors can be placed at upstream and downstream positions near the head to measure the LTMDs. As the first-order derivatives of the LTMDs in the spatial domain are needed to

define the boundary conditions, at least two edge sensors are required at each end of the segment. Computational complexity of solving the partial differential equation online is investigated.

1.5 Organization of the Thesis

Chapter 2 presents a brief review of the reel-to-reel control in the tape system and a model of the tape tension loop decoupled from the velocity control loop. The feedforward inspired control that simultaneously addresses the variations in both nominal radius and the reel runout is discussed, followed by simulation results that demonstrate the tension error caused by reel runout can be reduced by three orders of magnitude.

Chapter 3 first introduces the dynamics of the head actuator and the structure of the feed-forward combined with feedback control scheme aiming to reduce the position error between the head and the track in the presence of LTM. Approximate dynamic inversion techniques and model matching methods are explored to design the feedforward controller. The model matching methods suit this application better as the controller is causal and the input amplitude can be regulated.

Chapter 4 and Chapter 5 describe the algorithms to estimate the LTMDs at the head from the measured upstream and downstream LTMDs. The linear regression method is developed in Chapter 4. Chapter 5 explores how to solve the partial differential equation describing the lateral motion of a short segment of tape surrounding the head. Simulation results to demonstrate the effectiveness of the feedforward control in reducing the position error caused by the lateral tape motion are presented. The feedforward controller, obtained through the H_2 -norm model matching method, uses as its input the LTMD at the head estimated by solving the partial differential equation.

Finally, discussion on feasibility of implementing the feedforward controller and possible future work is included in Chapter 6.

Portions of this work have been presented in other publications by the author. Chapter 2 is a combination and revision of [43] and [44]. The least-squares based algorithm to estimate the

LTMD at the head included in Chapter 4 has been presented in [45]. The feedforward schemes discussed in Chapter 3 are presented in [47] and [46].

Chapter 2

Controller Designs to Attenuate Tension Errors in Tape Reel-to-reel Servo Systems

This chapter presents the feedforward inspired control schemes to reduce tension error caused by reel eccentricities in the time-varying tape system. It first reviews a classic tape model and discusses the characteristics of the variations in the reel radii; then introduces a decoupled tape tension loop from this study. An adaptive control algorithm to reject disturbances with time-varying frequencies in an linear time-invariant system is then presented. The adaptive algorithm works for a plant that includes the nominal radius variation due to tape winding. However, the adaptation fails when reel eccentricities are included in the plant because the convergence speed of the adaptation loop is much slower than the rate at which the eccentricities vary. To account for both nominal radius variations and reel eccentricities simultaneously, a feedforward inspired control scheme is presented. The control scheme includes a time-varying reference input filter to address the nominal radius variations and a feedforward compensation that attenuates the quasi-periodic tension error caused by the unknown reel eccentricities. Simulation results and comparison are presented to demonstrate the effectiveness of the final feedforward control scheme.

2.1 Tape Model and Tension Loop

The schematic in Fig. 2.1 illustrates a classic lumped-parameter model of a tape system [3][20]. The tape winds from the source reel (left) to the take-up reel. $J_i(t)$, $r_i(t)$, and $\omega_i(t)$ ($i = 1, 2$) are the rotating inertia, radius, and angular velocity of each reel, respectively. The unsupported tape

between the two reels is modeled by a parallel dashpot and spring with damping coefficient D and spring constant K , respectively.

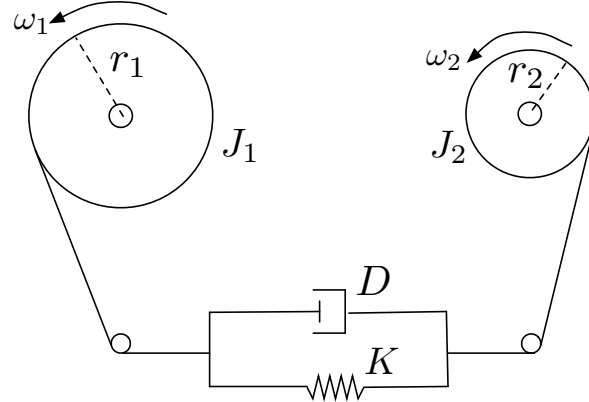


Figure 2.1: Lumped-parameter model of a tape system.

Each reel is driven by a DC motor whose motor friction viscosity coefficient is denoted as β_i and the torque constant is denoted as K_{ti} . The current applied to each motor is $u_i(t)$. Define $T(t)$ as the tape tension, $V_i(t)$ as the tangential velocity of the tape at each reel, and $V(t)$ as the linear tape velocity. Let the state $X = [T(t), V_1(t), V_2(t)]^\top$, the input $U = [u_1(t), u_2(t)]^\top$, the output $Y = [T(t), V(t)]^\top$, and $\eta(t) = \frac{r_1^2(t)}{J_1(t)} + \frac{r_2^2(t)}{J_2(t)}$, where $^\top$ denotes transpose. A state-space equation of the tape system is then [3]

$$\begin{cases} \dot{X}(t) &= \mathbf{A}(t)X(t) + \mathbf{B}(t)U(t) \\ Y(t) &= C_0X(t) \end{cases}, \quad (2.1)$$

$$\mathbf{A}(t) = \begin{bmatrix} -D\eta(t) & -K+D\frac{\beta_1}{J_1(t)} & K-D\frac{\beta_2}{J_2(t)} \\ \frac{r_1^2(t)}{J_1(t)} & -\frac{\beta_1}{J_1(t)} & 0 \\ -\frac{r_2^2(t)}{J_2(t)} & 0 & -\frac{\beta_2}{J_2(t)} \end{bmatrix},$$

$$\mathbf{B}(t) = \begin{bmatrix} -D\frac{r_1(t)K_{t1}}{J_1(t)} & D\frac{r_2(t)K_{t2}}{J_2(t)} \\ \frac{r_1(t)K_{t1}}{J_1(t)} & 0 \\ 0 & \frac{r_2(t)K_{t2}}{J_2(t)} \end{bmatrix},$$

$$C_0 = \begin{bmatrix} 1 & 0 & 0 \\ 0 & 0.5 & 0.5 \end{bmatrix}.$$

When the tape winds, both r_i and J_i change. D , K , and other parameters might also vary [3]. However, this research aims at investigating the tension error caused by the time-varying reel radii in steady state. Hence only the time-varying dynamics from r_i and J_i are taken into account. Other parameters are considered as constants.

2.1.1 Time-varying Reel Radii in Tape Systems

The variations in the reel radius $r_i(t)$ consist of two components: (a) the nominal time-varying radius $r_{ni}(t)$ as a result of tape winding and (b) the reel eccentricities $r_{ri}(t)$ due to non-perfectly circular reels. The changing rate of $r_{ni}(t)$ is a function of the angular velocity $\omega_i(t)$ and tape thickness ϵ . With these notations, the radius of each reel $r_i(t)(i = 1, 2)$ is

$$\begin{aligned} r_i(t) &= r_{ni}(t) + r_{ri}(t) \\ &= r_i(t_0) \mp \int_{t_0}^t \frac{\epsilon\omega_i(\tau)}{2\pi} d\tau + r_{ri}(t). \end{aligned}$$

In the tape industry, the nominal radius $r_{ni}(t)$ is usually known and used in controller design to regulate the tangential velocity and tape tension. The reel eccentricities, also known as reel runout, are usually unknown and not addressed. They introduce tension ripples that can lead to lateral shifts in the tape. If the reel rotates at a constant angular velocity and the nominal radius is invariant, the same reel runout behavior repeats in every revolution.

The rotating inertia of each reel is related to the radii by

$$J_i(t) = J_0 + K_J(r_i(t)^4 - r_0^4),$$

where r_0 and J_0 are the radius and inertia of an empty reel, respectively. K_J is the tape pack inertia constant. In general, the variations in the reel inertia are very slow and can be ignored for many systems. This study accounts for them because this adds only trivial complications. Moreover, since the magnitude of the reel runout is much smaller than that of the nominal radius, the inertia variations caused by the reel runout can be neglected and hence only the variations in the reel inertia caused by the time-varying nominal radius are taken into account.

2.1.2 Tape Tension Loop

By pre-multiplying the input U in Equation (2.1) with a time-varying matrix

$$D_c(t) = \begin{bmatrix} -\frac{r_2(t)J_1(t)}{r_1(t)J_2(t)} & \frac{r_2(t)J_1(t)}{r_1(t)J_2(t)} \\ 1 & 1 \end{bmatrix},$$

as shown in Fig. 2.2, the tension loop and the velocity loop can be decoupled [18]. This decoupling method is designed to work perfectly at mid-pack where both reel radii are equal, but also works reasonably well at all operating points of the tape drive. At mid-pack, the tension loop is perfectly decoupled from the velocity loop and the transfer function from u_T to T is

$$G_T(s) = \frac{2K_tDr_m(s + \frac{K}{D})}{J_ms^2 + (\beta + 2Dr_m^2)s + 2Kr_m^2},$$

where r_m and J_m are the reel radius and the inertia at mid-pack, respectively.

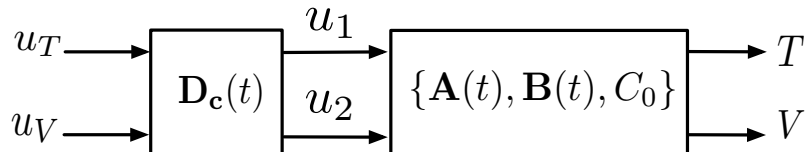


Figure 2.2: Decoupling algorithm for the tension loop and the velocity loop.

To simulate the time-varying tension loop in *Matlab* [1], G_T is put in the observer canonical state-space form in which tension T is the first state. The other state is a function of the difference between the tangential velocities of the two reels. Replacing the constants r_m and J_m with the time-varying $r(t)$ and $J(t)$, respectively, the system model is

$$\begin{cases} \dot{X}_T(t) = \mathbf{A}_T(t)X_T(t) + \mathbf{B}_T u(t) \\ Y(t) = CX_T(t) \end{cases}, \quad (2.2)$$

$$\mathbf{A}_T(t) = \begin{bmatrix} -\frac{\beta+2Dr(t)^2}{J(t)} & 1 \\ -\frac{2Kr(t)^2}{J(t)} & 0 \end{bmatrix},$$

$$\mathbf{B}_T(t) = \begin{bmatrix} \frac{2K_t Dr(t)}{J(t)} \\ \frac{2K_t Kr(t)}{J(t)} \end{bmatrix},$$

$$C = \begin{bmatrix} 1 & 0 \end{bmatrix}.$$

The system matrices $\mathbf{A}_T(t)$ and $\mathbf{B}_T(t)$ are functions of $r(t)$ and $J(t)$.

In this study, the tension loop is implemented as in Equation (2.2) with parameters such as those in Table 2.1.

Table 2.1: Tape system parameters for simulation

Parameter	Label	Value
ϵ	Thickness of the tape	$7.7e-6$ m
K_t	Motor torque constant	0.0189 N m/Amp
β	Motor viscosity coefficient	$6e-5$ N m sec/rad
D	Dashpot constant	0.9 N sec/m
K	Spring constant	600 N/m
$r(t)$	Radius of the reel	0.014m to 0.028 m
r_m	Mid-pack radius of the reel	0.02389 m
r_0	Radius of an empty reel	0.014 m
K_J	Tape pack inertia constant	33.49 kg/m^2
J_0	Inertia of an empty reel	$2.2e-5 \text{ kg m}^2$

The reel eccentricity data used is from an actual tape industry reel. The 48 discrete runout samples over one revolution are linearly interpolated as shown in Fig. 2.3. The peak-to-peak runout

is on the order of 10^{-4} m.

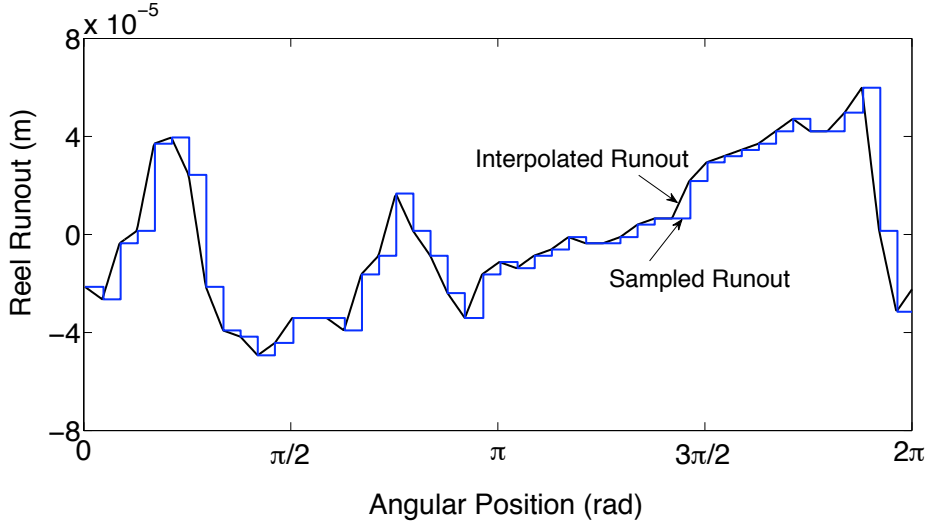


Figure 2.3: Reel eccentricity data is interpolated from an industry sample.

2.2 Adaptive Control Algorithm in Continuous-time Domain

This section introduces an extension of an existing adaptive control algorithm in the continuous-time domain to address disturbances with time-varying frequencies in the tension loop. The block diagram of the tension loop in the continuous-time domain is depicted in Fig. 2.4. G_T is the plant with time-varying radius as in Equation (2.2). T_d is the desired tension value at steady state and y is the tension output. The controller C_T is a notch controller designed for the plant at mid-pack and also guarantees system stability. $d(t)$ is the input disturbance to the plant. The adaptive controller C_A generates the compensation input u_a to mitigate the effects from $d(t)$ to the tension output.

The algorithm in [4] rejects sinusoidal input disturbances with fixed magnitude and frequency to a LTI system by generating a synthesized control input u_a whose magnitude and frequency are adapted to those of the disturbances from the output error. In this application, ideally, the system response to $u_a(t)$ should be the additive inverse of the tension error T_e at any time.

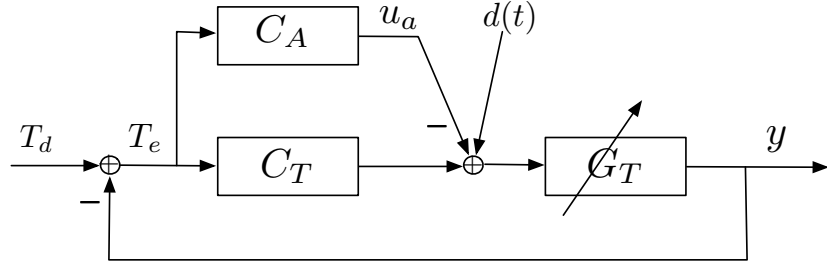


Figure 2.4: The time-varying tension control loop in continuous-time domain.

We extend the algorithm in [4] to construct the adaptive controller C_A , shown in Fig. 2.5. Here, m_a , ω_a , and θ_a denote the estimates of magnitude, frequency, and phase angle of the

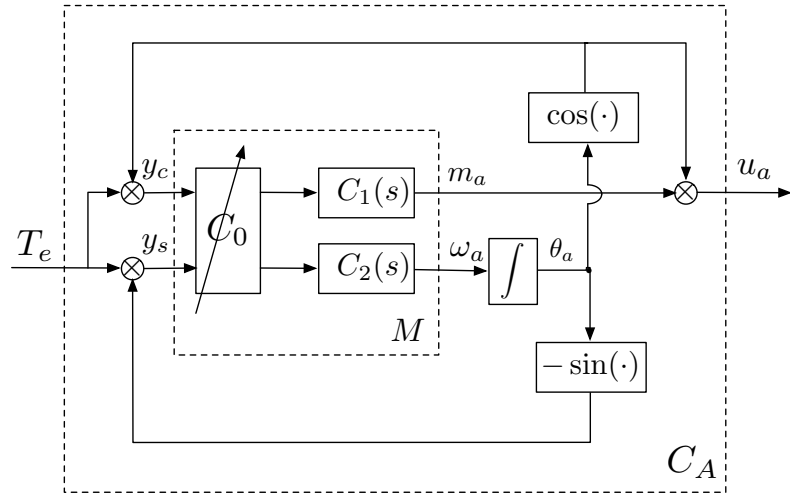


Figure 2.5: C_A is a time-varying controller that adapts the frequency ω_a and magnitude m_a to synthesize an input u_a whose plant response ideally is the additive inverse of the tension error.

compensation input, respectively. In contrast to the original algorithm, C_0 is now time-varying:

$$C_0 = \left[\begin{array}{cc} 0.5P_R(j\omega) & -0.5P_I(j\omega) \\ 0.5P_I(j\omega) & 0.5P_R(j\omega) \end{array} \right]^{-1} \Bigg|_{\omega=\omega_d(t)}.$$

Here, P is transfer function of the model G_T in Equation (2.2) evaluated at the mid-pack radius r_m . $P_R(j\omega) \doteq \text{Re}(P(j\omega))$ and $P_I(j\omega) \doteq \text{Im}(P(j\omega))$. $\omega_d(t)$ is the time-varying frequency of the

disturbance. $C_1(s)$ and $C_2(s)$ are two fixed compensators chosen to guarantee the stability and the convergence speed of the adaptation loops. In this structure, the vector $[y_c, y_s]^\top$ is mapped into the adapted parameters $[m_a, \omega_a]^\top$. The detailed derivation of this algorithm can be found in [4, 48].

The extended adaptive control algorithm can reject time-varying disturbances to a LTI tension loop, as shown in Fig. 2.6. In the simulation, G_T is evaluated at the mid-pack radius. $d(t)$ is a sinusoidal disturbance and the frequency increases at a constant rate. The adapted magnitude and frequency follows that of the disturbance and the tension error is reduced by 2 orders of magnitude after the adaptation converges.

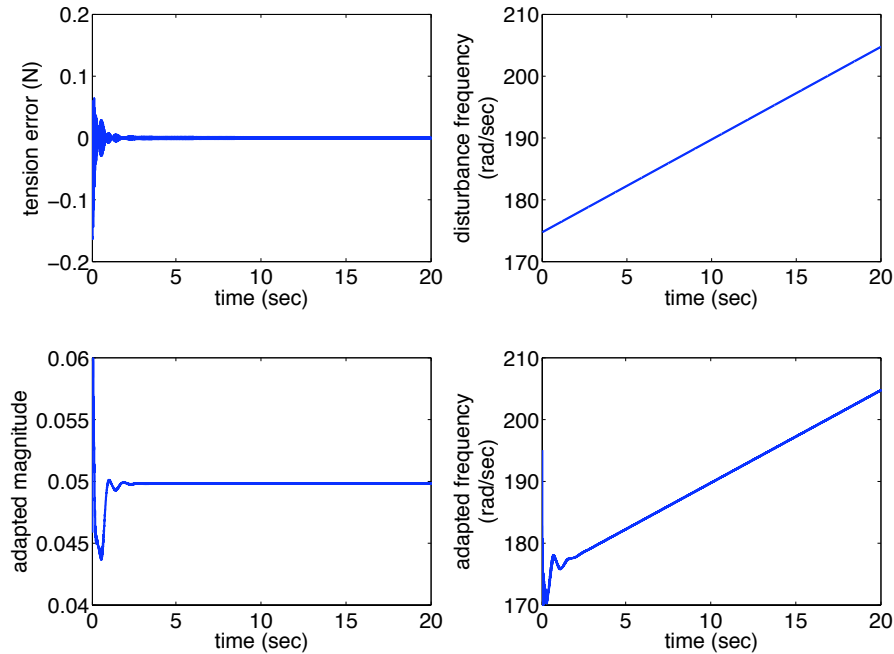


Figure 2.6: The adapted magnitude and frequency follows that of the disturbance.

When G_T contains variations in the nominal radius due to tape winding, the performance of the algorithm is about the same. However, when reel eccentricities are included in G_T , the adaptation fails. This is because the nominal radius variations due to tape winding are much slower than the convergence speed of the adaptation loop while reel eccentricities vary at a faster

rate [31]. This can also been seen in the tension error signal T_e as it contains the frequency components due to reel eccentricities. It is a challenge to obtain an adaptive controller that can effectively reduce the tension errors caused by the unknown time-varying reel eccentricities.

2.3 Feedforward Control Algorithms in Discrete-time Domain

In this section, feedforward-inspired control algorithms to address both the known and unknown variations in reel radii in the discrete-time domain are discussed. A discrete-time model of the tape tension loop is obtained by freezing the parameters of the time-varying matrices in Equation (2.2) at every time step [8]:

$$\begin{cases} X_{k+1} = A_k X_k + B_k \tilde{u}_k \\ Y_k = C X_k \end{cases} .$$

The system block diagram is shown in Fig. 2.7. Here, K_{fd} is a full-state feedback controller designed to guarantee the stability of the tension loop at all operating points. R_k is a time-varying filter for the reference input to generate \hat{u} that takes into account the known variations in the radius; C_{ff} is a feedforward controller that generates the compensation input \tilde{u} based on past outputs to address the unknown reel eccentricities; and z^{-k_v} is a delay to the output Y_k where the delay constant k_v varies across revolutions. The input u to the closed-loop system is the sum of \hat{u} and \tilde{u} .

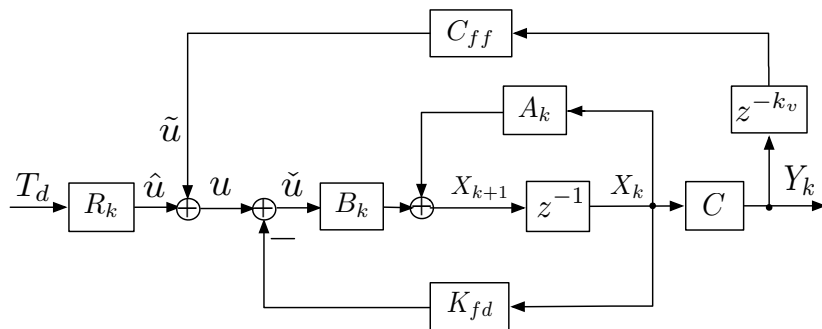


Figure 2.7: Block diagram of the tension loop in the discrete-time domain.

In most simulations presented in this thesis, the sampling rate is 12,000 Hz. The continuous-time system is periodic when the nominal radius is fixed. However, the sampled system is periodic

only at particular sampling frequencies that depend on upon the nominal radius and reel rotating frequency. Based on the values of these two parameters when the nominal radius is fixed, the sampling frequency is chosen to be 12,015 Hz so as to maintain the periodicity of the sampled system. The full-state feedback K_{fd} is designed to be $[-0.7766, 0.0109]$ so that the poles of the tension loop are within the unit circle at all operating points. The desired tension and velocity values are $T_d = 1$ N and $V_d = 4$ m/sec, respectively. The actual tangential velocity of the tape in steady state is assumed to track V_d perfectly as a result of a separate velocity control loop such as in [3].

2.3.1 Time-varying Reference Input Filter

For the time-varying discrete tension loop represented in Fig. 2.7, when the compensation input \tilde{u} is zero, the input to the plant at step k is:

$$\check{u}_k = R_k T_d - K_{fd} X_k. \quad (2.3)$$

We define the desired final value of the state as X_{ss_k} and the control input for the system $\{A_k, B_k, C\}$ at sampling step k and \check{u}_{ss_k} . After the system has reached steady state, the discrete-time system equations are

$$\begin{cases} X_{ss_k} &= A_k X_{ss_k} + B_k \check{u}_{ss_k} \\ T_d &= C X_{ss_k} \end{cases}.$$

Hence, the time-varying reference input filter is

$$R_k = (K_{fd} X_{ss_k} + \check{u}_{ss_k}) / T_d$$

and

$$\begin{bmatrix} X_{ss_k} \\ \check{u}_{ss_k} \end{bmatrix} = \begin{bmatrix} A_k - I & B_k \\ C & 0 \end{bmatrix}^{-1} \begin{bmatrix} \mathbf{0} \\ T_d \end{bmatrix}.$$

Theoretically, if the state matrices are accurately known at every sampling step, the feedforward filter R_k will lead to zero steady-state tension error.

If the reel runout data is collected during an initialization procedure when the tape cartridge is inserted into a drive, R_k can address both the time-varying nominal radius and the reel runout. Fig. 2.8 shows that the effects on the tension from all variations in the source reel radius are effectively canceled.

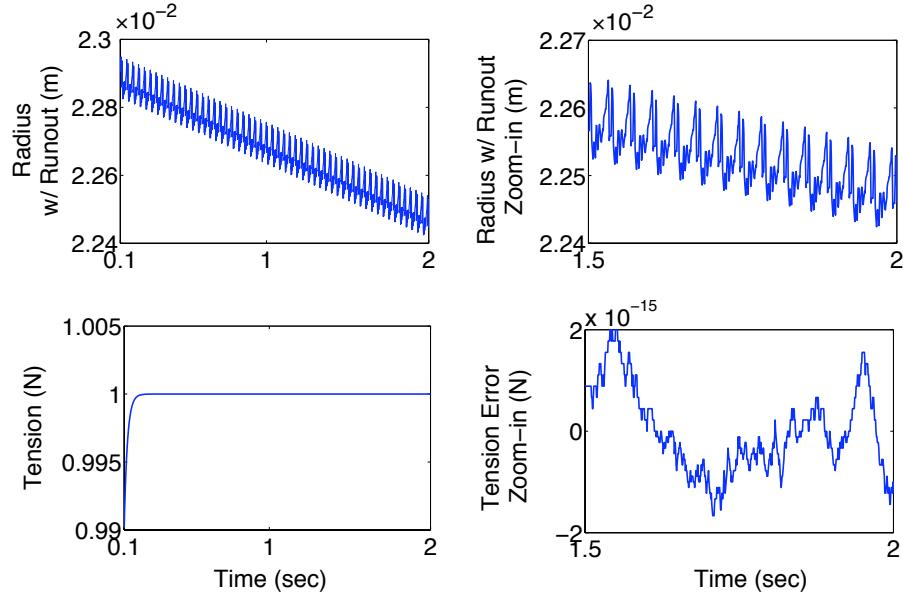


Figure 2.8: Tension error is essentially eliminated by the time-varying filter that addresses both nominal reel radius variations and reel runout.

This scheme requires knowledge of the nominal radius and the eccentricities to compute the control input. In practice, reel eccentricity data is unavailable and R_k only addresses the variations in nominal radius. In this case, the tension error is on the order of 10^{-3} N, as shown in Fig. 2.9. To reduce this error, one can take advantage of the pseudo-periodicity of the system.

2.3.2 Control to Address Reel Eccentricities

As the nominal reel radius varies and tape tangential velocity is fixed, the reel rotating frequency varies every revolution and the tension loop is not a purely periodic system. However, since tape is very thin, the system can be considered as periodic between two adjacent revolutions. The proposed algorithm starts with calculating an initial compensation input for the first two

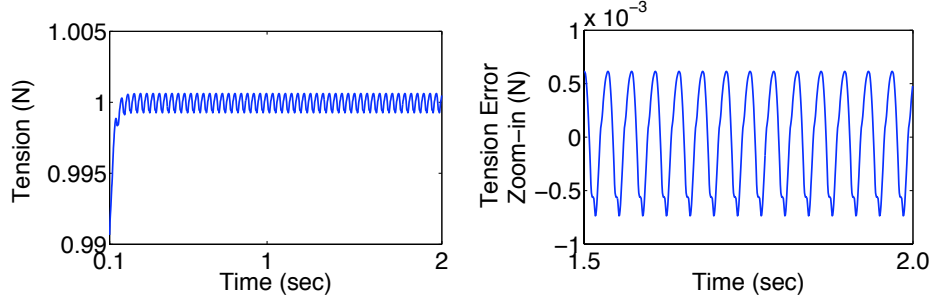


Figure 2.9: The tension error is on the order of 10^{-3} N when R_k only addresses the nominal variations in the radius.

revolutions. For future revolutions, an additional input sequence is added on top of the initial compensation input. Moreover, since the period of each revolution varies, the compensation input is carefully interpolated and a new definition of a full revolution is introduced. The compensation input before interpolation is denoted as \tilde{u}_0 .

2.3.2.1 Initial Compensation Input

Define the closed-loop system in Fig. 2.7 at step k as $\{A_{clk}, B_k, C\}$ where $A_{clk} = A_k - B_k K_{fd}$. Consider the system of one revolution, denoted as μ . Denote the initial state of revolution μ as X_1 . Then the output is

$$Y_k = C \prod_{i=1}^{k-1} A_{cli} X_1 + C \sum_{j=1}^{k-2} \prod_{i=j+1}^{k-1} A_{cli} B_j u_j + C B_{k-1} u_{k-1}.$$

The desired output of the system is T_d and the output error in $Y_k (k > 1)$ is $\tilde{Y}_k = T_d - Y_k$. Denote the compensation input to cancel \tilde{Y}_k as u_{pk} , the new input \bar{u}_k with the compensation input at the k th step then is

$$\bar{u}_k = u_k + u_{pk}.$$

The state-space equations for the new system become

$$\begin{cases} \bar{X}_{k+1} = A_{clk} \bar{X}_k + B_k \bar{u}_k \\ \bar{Y}_k = C \bar{X}_k \end{cases}.$$

If the initial state of the new system is X_1 as in the original system, the new output at the k th step is

$$\begin{aligned}\bar{Y}_k &= C \prod_{i=1}^{k-1} A_{cli} X_1 + C \sum_{j=1}^{k-2} \prod_{i=j+1}^{k-1} A_{cli} B_j \bar{u}_j + CB_{k-1} \bar{u}_{k-1} \\ &= Y_k + C \sum_{j=1}^{k-2} \prod_{i=j+1}^{k-1} A_{cli} B_j u_{pj} + CB_{k-1} u_{pk-1}.\end{aligned}$$

and is equal to T_d , ideally. Hence,

$$\begin{aligned}\tilde{Y}_k &= T_d - Y_k = \bar{Y}_k - Y_k \\ &= C \sum_{j=1}^{k-2} \prod_{i=j+1}^{k-1} A_{cli} B_j u_{pj} + CB_{k-1} u_{pk-1}.\end{aligned}$$

If CB_{k-1} is non-singular, u_p can be solved by

$$u_p(k-1) = \frac{1}{CB_{k-1}} \left(\tilde{Y}_k - C \sum_{j=1}^{k-2} \prod_{i=j+1}^{k-1} A_{cli} B_j u_{pj} \right) \quad (2.4)$$

when $k > 1$.

If the closed-loop system is purely periodic with a period N_p , a compensation input sequence $u_p(i)$ ($i = 1, 2, \dots, N_p$) for period μ can be computed using the output errors of this period. This compensation sequence can then be applied to any following periods $\bar{\mu}$ ($\bar{\mu} > \mu$) to cancel the output error, given the initial state of period $\bar{\mu}$ is the same as the initial state of period μ . Once the compensation input sequence is applied to period $\bar{\mu}$, the initial state of the following period $\bar{\mu} + 1$ does not equal that of period μ and the compensation input sequence $u_p(i)$ will not cancel the error in period $\bar{\mu} + 1$. Thus, at least one more period after the output of the compensated system reaches the steady state should be investigated to generate the compensation input sequence.

For the studied tension loop, using more than two periods of tension error to compute the $u_p(i)$ series is found not to yield much further improvement than using two periods. Hence, two periods (μ and $\mu + 1$) of the output error are investigated to compute the initial compensation input sequence $u_p(i)$ ($i = 1, 2, \dots, 2N_p$) using Equation (2.4). This initial compensation input sequence is then applied to periods $\mu + 2$ and $\mu + 3$.

Define the pair (m, n) as the index of the sampled n th step in the m th revolution; (m, n) may be in subscripts in some equations to save space. The compensation input $\tilde{u}_0(m, n)$ for revolution $\mu + 2$ and $\mu + 3$ is

$$\tilde{u}_0(m, n) = \begin{cases} u_p(n), & m = \mu + 2 \\ u_p(N_p + n), & m = \mu + 3 \end{cases}. \quad (2.5)$$

When the nominal radius is fixed and the system is purely periodic, repeating the same compensation input sequence after revolution $\mu + 3$ reduces the tension error by about three orders of magnitude to 10^{-6} N, as shown in Fig. 2.10.

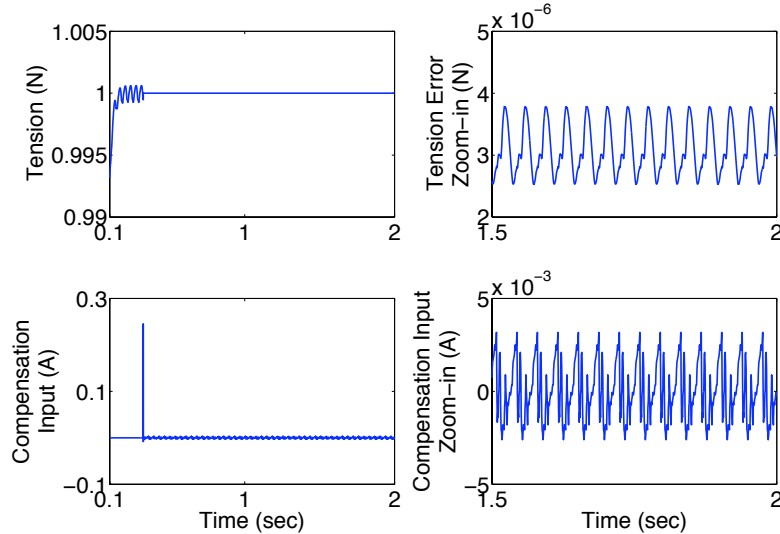


Figure 2.10: Nominal radius fixed (purely periodic system), reel runout unknown: the initial compensation input computed from tension errors in two revolutions reduces the error by three orders of magnitude.

There are two issues that are needed to be addressed. First, note that the state matrices used to compute $\tilde{u}_p(k)$ are the nominal state matrices that do not include the (unknown) reel eccentricities in the radius. Thus the computed compensation input is not ideally accurate and hence 10^{-6} N residual tension error exists. Second, a real tape system is not purely periodic because the nominal radius keeps varying. In this case, the repeated initial compensation input first reduces the tension to 10^{-6} N. Then the tension error grows as the variation in the nominal radius increases

over time and the difference between the current system becomes and when the initial compensation input sequence was computed becomes larger, as shown in Fig. 2.11. The plots show a simulation duration of 4 seconds so that the increase is more visible. To address the variation, we update the

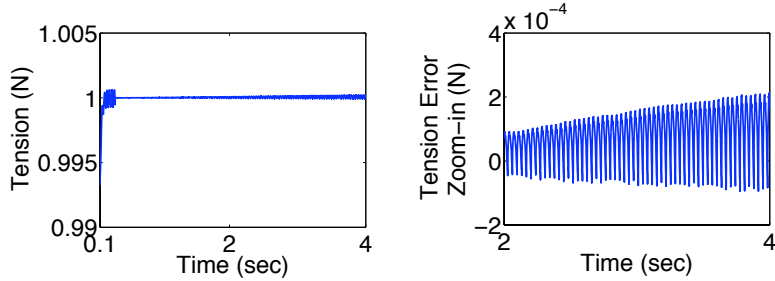


Figure 2.11: The tension error is reduced by the initial compensation input sequence first and then grows as the tape winds.

compensation input every revolution after revolution $\mu + 3$.

2.3.2.2 Additional Compensation Input

The residual tension error $\tilde{Y}_{(m,n)}$ at step (m, n) when a compensation input is applied is $\tilde{Y}_{(m,n)} = T_d - Y_{(m,n)}$. Similarly to Equation (2.4), the additional input $v(m, n-1)$ at step $(m, n-1)$ that should have canceled $\tilde{Y}_{(m,n)}$ can be solved by

$$v_{(m,n-1)} = \frac{\left(\tilde{Y}_{(m,n)} - C \sum_{j=1}^{n-2} \prod_{i=j+1}^{n-1} A_{cl(m,i)} B_{(m,j)} v_{(m,j)} \right)}{C B_{(m,n-1)}}.$$

when $C B_{m,n-1}$ is non-singular. Same as computing the initial compensation input, the state matrices used to compute $v_{(m,n-1)}$ are the nominal state matrices that are available.

As the tension loop can be considered as periodic for two consecutive revolutions, applying the additional $v_{m,n-1}$ at step $(m+1, n-1)$ will reduce the tension error at step $(m+1, n)$. Hence, the compensation input $\tilde{u}_0(m, n)$ for revolutions $m \geq \mu + 4$ is

$$\tilde{u}_0(m, n) = \tilde{u}_0(m-1, n) + v(m-1, n). \quad (2.6)$$

2.3.2.3 Interpolation

Since the nominal radius varies and the period of each revolution changes slowly, no fixed sampling rate can guarantee an integer number of sample points for every rotation of 2π radians in the discrete-time domain. In this case, a full revolution is considered completed when the angular position of the sample point crosses over that of the first sampling point in the same revolution. The angular position of the first sample in revolution m relative to that in revolution $m - 1$ is defined as $\alpha_0(m)$, as shown in Fig. 2.12. The angles are not drawn to scale. For the first revolution, $\alpha_0(1)$ is zero. The angle the reel rotates in revolution m is thus $2\pi + \alpha_0(m+1)$. Define N_m as the total number of the sampled points in revolution m , then the sampling interval δ_m of revolution m is

$$\delta_m = \frac{2\pi + \alpha_0(m+1)}{N_m}.$$

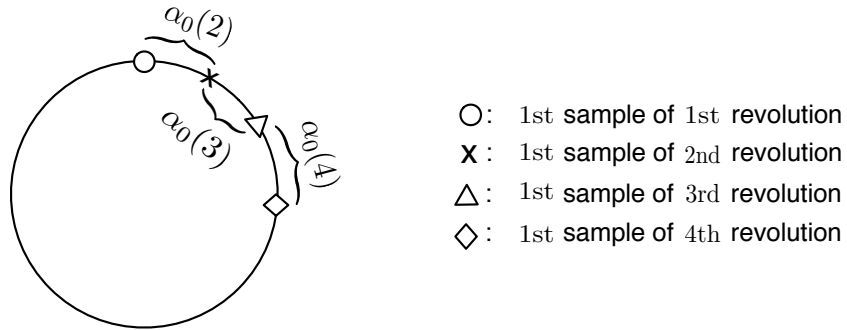


Figure 2.12: A revolution is completed when the angular position of a sampling point crosses over that of the first sampling point in the same revolution.

Let $\theta(m, n)$ be the angle that the reel has rotated at the n th step in the m th revolution. θ is reset to zero when a new revolution starts, i.e., $\theta(:, 1)$ is always zero. Suppose the physical angular location on the reel at $\theta(m, n)$ lies between the angular positions of steps n_e and n_e+1 in the previous revolution $m-1$. Specifically,

$$n_e = \left\lfloor \frac{\theta(m, n) + \alpha_0(m)}{\delta(m-1)} \right\rfloor + 1$$

where $\lfloor \cdot \rfloor$ is the floor operator. The 2nd term of this equation is due to the fact that the first index in each revolution is 1 (and not 0).

Instead of directly applying the compensation input from Equation (2.5) and (2.6) to the system, $\tilde{u}_0(m, n_e)$ and $\tilde{u}_0(m, n_e + 1)$ computed using Equation (2.6) are linearly interpolated to generate the final compensation input $\tilde{u}(m, n)$ at step (m, n) , as illustrated in Equation (2.7).

$$\begin{cases} \tilde{u}(m, n) = \tilde{u}_0(m, n_e) + \frac{\theta(m, n) - \theta(m-1, n_e)}{\delta(m-1)} \cdot \Delta \tilde{u}_0 \\ \Delta \tilde{u}_0 = \tilde{u}_0(m, n_e + 1) - \tilde{u}_0(m, n_e) \end{cases}. \quad (2.7)$$

Fig. 2.13 shows that the tension error is reduced by three orders of magnitude to 10^{-6} N when the interpolated compensation input $\tilde{u}(m, n)$ is applied. The compensation input sequence contains the initial compensation input and the interpolated additional compensation input that is updated every revolution based on the tension error of the immediately previous revolution, as illustrated in Equations (2.5), (2.6), and (2.7). Here, the reference input filter R_k addresses the known variations in the nominal radius.

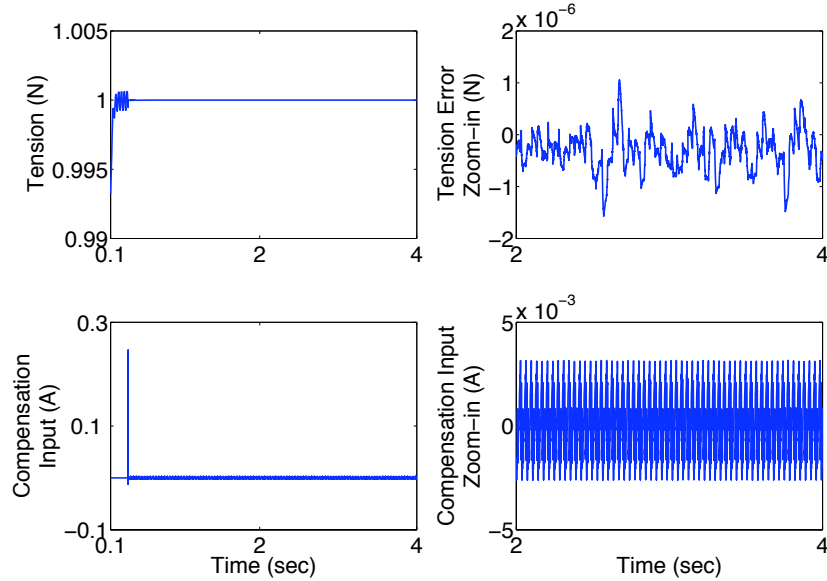


Figure 2.13: The nominal radius varies and reel eccentricities are unknown. The compensation input is updated every revolution and the steady-state tension error is reduced by three orders of magnitude from 10^{-3} N to 10^{-6} N.

In the special case when the nominal radius is fixed and the sampling points of each period are the same, this algorithm can achieve perfect error rejection performance, as shown in Fig. 2.14. Comparing to applying the repeated initial compensation input only (Fig. 2.11), the tension error is completely eliminated when the ideal compensation input sequence to cancel the residual tension error is achieved after a certain number of revolutions, without knowing the reel eccentricities. In this case, the algorithm is also robust to parameter uncertainties at the cost of a longer convergence time. Simulation results (not presented) show when the parameters D and β each contain a 10% error, it takes a few more revolutions for the compensation input sequence to converge.

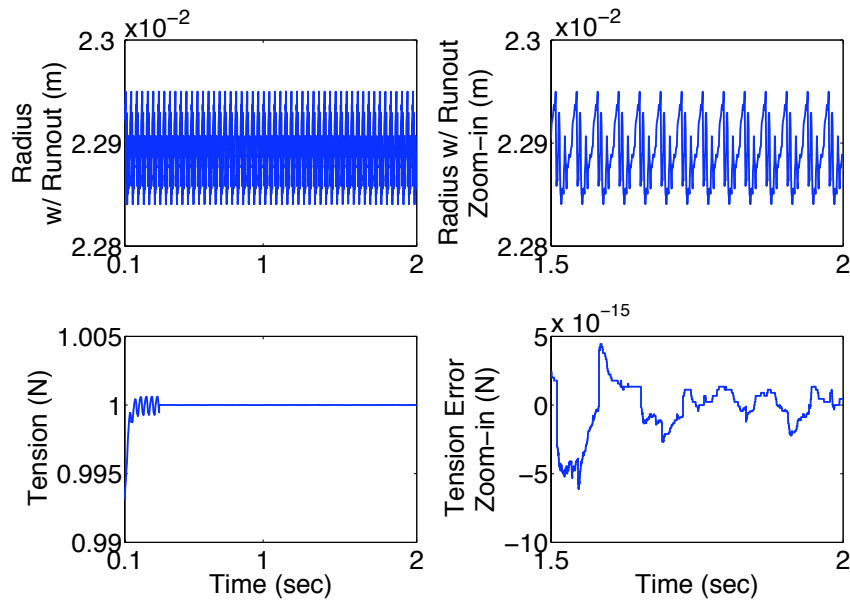


Figure 2.14: When the nominal radius is fixed, the steady-state tension error is effectively zero.

2.4 Conclusions and Discussion

It is difficult for an adaptive control algorithm to address tension errors caused by the time-varying and unknown reel runout because the varying rate of the radius is usually faster than the convergence speed of the adaptation algorithm. The developed control scheme regulates tape tension in a time-varying tape system by simultaneously taking into account the nominal radius

variations and the reel eccentricities. The known nominal radius variations are addressed by a time-varying feedforward filter R_k to the reference input to generate \hat{u}_k . The unknown reel runout can be considered as nearly repetitive in two consecutive revolutions since the change in the nominal radius is negligible compared to the reel runout. The compensation input computed from the tension error of the previous revolution is applied to the current revolution.

Simulation results of regulating tension in the time-varying tape system are summarized in Table 2.2. When all the variations in the reel radius are known, \hat{u}_k leads to a steady-state tension error that is effectively zero (Fig. 2.8). When the reel runout is unknown and the nominal radius is fixed, repeating the compensation input $\tilde{u}_0(m, n)$ after $\mu + 3$ revolution reduces the tension error by three orders of magnitude to 10^{-6} N (Fig. 2.10). When the nominal radius varies, the extended compensation input $\tilde{u}(m, n)$ that is updated every revolution to account for the time-varying period of the system also reduces the tension error by three orders of magnitude (Fig. 2.13).

Table 2.2: Magnitude of steady-state tension error (N)

Algorithm	r_r Known	$\frac{r_r}{r_n}$ Unknown	
	Fixed	Varying	
\hat{u}_k in Equation (2.3)	10^{-15}	10^{-3}	10^{-3}
$\tilde{u}_0(m, n)$ in Equation (2.5)	N/A	10^{-6}	Unstable
$\tilde{u}(m, n)$ in Equation (2.7)	N/A	10^{-15}	10^{-6}

Smaller tension error allows thinner tape and enables higher data capacity and transfer rate. The proposed control schemes are independent of the characteristics of the reel eccentricities. They can also be applied to other web-winding processes.

Chapter 3

Feedforward Control Designs to Reduce Position Error in Tape Head Positioning Systems

This chapter first introduces the model of the tape head actuator and the characteristics of the lateral tape motion that causes misalignment between the head and the desired data track. The structure of a feedforward controller in combination with a feedback controller to further reduce the position error caused by LTM is then discussed. A number of methods to design the feedforward controller are explored and compared.

3.1 Tape Head Dynamics Model and Lateral Tape Motion

When tape transports longitudinally between the two reels, it tends to vibrate in the lateral direction as well, as shown in Fig. 1.1. One primary purpose of the head positioning servo system is to follow the desired data track as accurately as possible during read/write operations in spite of disturbances such as the lateral tape motion. Both the tape and the head assembly can exhibit out-of-plane motions (not shown in Fig. 1.1) that are beyond the scope of this dissertation.

3.1.1 Head Actuator Plant Model

A voice coil actuator moves the head assembly laterally with respect to the tape. The motion of the head is restrained by flex circuits that provide signals from the head to the read/write channel. Considering this coupling, the motion of the head actuator in the lateral direction can be modeled as a spring-mass-damper system with two resonances. Hence, a transfer function model

from the voice coil motor current to the head position is

$$G(s) = \frac{g \omega_1^2 \omega_2^2}{(s^2 + 2\zeta_1 \omega_1 s + \omega_1^2)(s^2 + 2\zeta_2 \omega_2 s + \omega_2^2)},$$

where ω_i ($i = 1, 2$) are the natural frequencies of the two resonances and g is a gain. The two resonances in a typical modern tape head positioning system are usually in the 10-100 Hz range and the 1-10 KHz range, respectively.

In this research, we have identified the two resonances of an actual tape head actuator and have designed a feedforward controller using the actuator model. For intellectual property reasons, we do not present the actual model in this dissertation. Instead, we use generic values of the parameters to illustrate the methods investigated. The two resonances are set to be $\omega_1 = 2\pi \cdot 100$ rad/sec and $\omega_2 = 2\pi \cdot 1000$ rad/sec. The damping ratios are $\zeta_1 = 0.0796$ and $\zeta_2 = 0.05$, respectively. The system gain g is set to be 2000. This model in the continuous-time domain is then converted to a discrete-time transfer function, as shown in Equation (3.1), by using a zero-order-hold (ZOH) on all inputs [8] and a sampling rate of 10 KHz:

$$G(z) = \frac{0.12633(z + 9.52)(z + 0.9853)(z + 0.102)}{(z^2 - 1.986z + 0.99)(z^2 - 1.569z + 0.9391)}. \quad (3.1)$$

Due to the fast sampling rate, the discrete-time model contains one non-minimum phase (NMP) zero at -9.52 [28]. Fig. 3.1 shows that one zero of the plant stays outside of the unit circle when the sampling frequency is higher than 570 Hz.

All four poles of the transfer function are within the unit circle and the plant is stable. Fig. 3.2 depicts the Bode plot of $G(z)$. While other discretization methods such as the bilinear transformation can preserve the minimum phase property of the continuous-time model, the zero-order-hold is used in order to be compatible with industry standards of how continuous-time plants are incorporated into sampled-data systems [8].

3.1.2 Lateral Tape Motion

Lateral tape motion has been identified as one of the main limiting factors for increasing the track densities on a magnetic tape [12]. Sources that excite LTM include friction between the tape

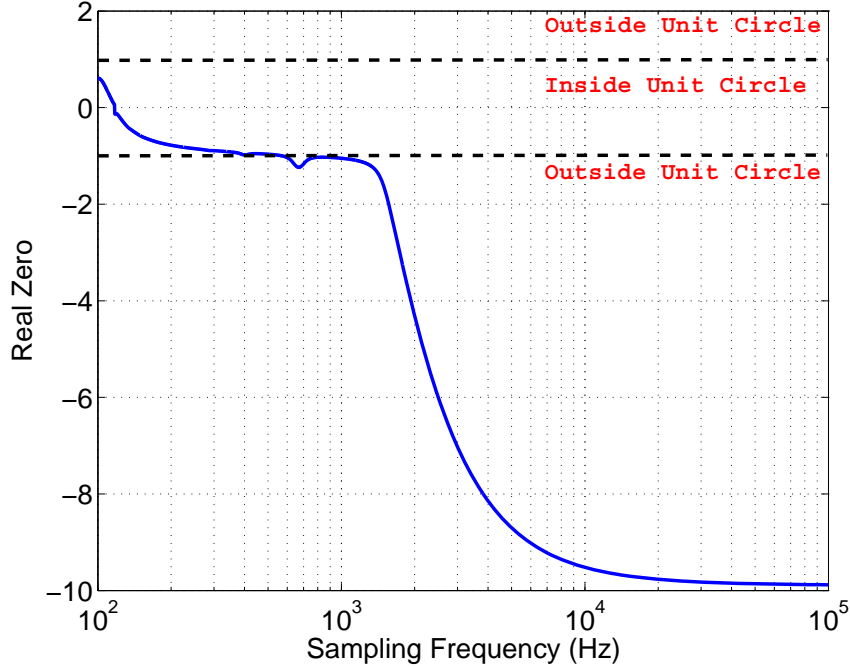


Figure 3.1: One of the zeros in the discrete tape head actuator model becomes non-minimum phase as the sampling frequency increases.

and the rollers; the radial runout of reels/rollers; and the impact between the tape and the flanges of the rollers. If LTM is not addressed correctly, it generates position error between the head and the desired track, as depicted in Fig. 3.3.

The dark line shows the data track position variation due to lateral motion and the grey line is the controlled head position without addressing LTM. The lateral displacement w_h represents the misalignment between the head and the desired track. Here, we assume that the data tracks on the tape are perfectly parallel with the edges of the tape. This is usually not true in a real tape cartridge because a) the edge of the tape is not perfectly straight due to manufacturing constraints; and b) tracks on the tape contain written-in error. However, the majority of the position error due to the misalignment between the tape edges and the track is in a lower frequency range that can be addressed by the feedback controller for the head actuator.

Lateral vibration models for magnetic tape have been intensively studied in the literature

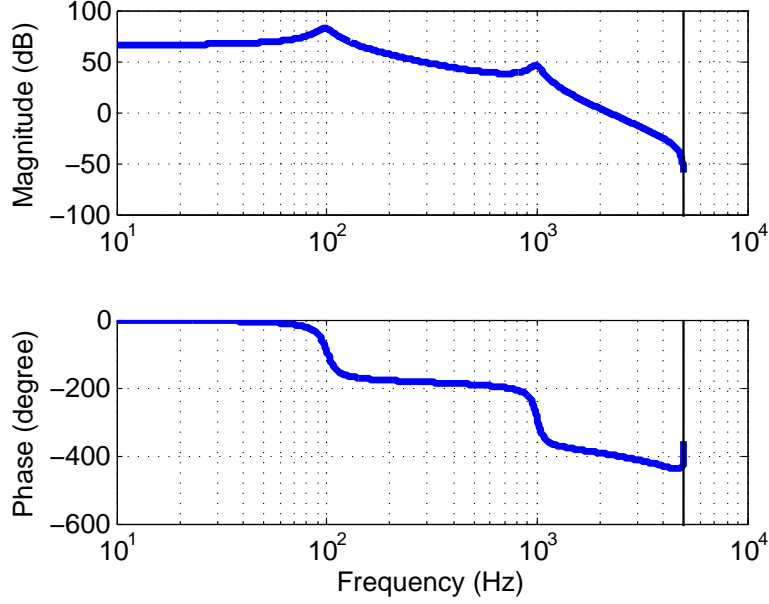


Figure 3.2: The tape head actuator model has two resonances and one NMP zero when the sampling frequency is at 10 KHz.

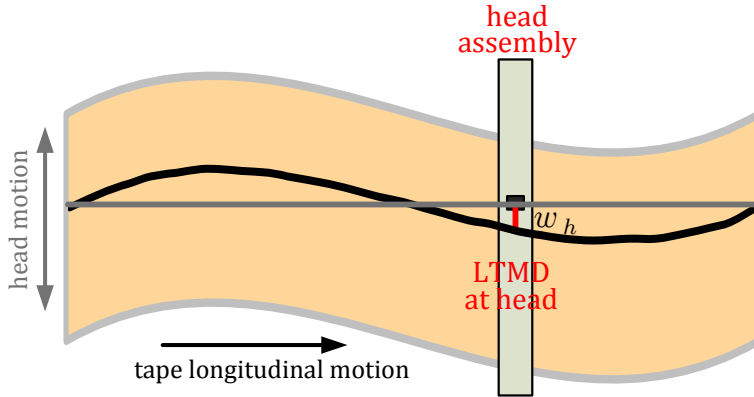


Figure 3.3: Lateral tape motion causes position error.

[5][21][25][32][33][39]. The author of [5] developed a system level model of lateral tape motion that includes the non-straight natural shape of the tape, the viscoelastic damping of the tape, nonlinear rollers, and flange impacts. The characteristics of lateral tape motion and disturbances exhibiting in the position error signal are studied in [13]. The typical peak-to-peak amplitude of

the displacements caused by tape motion in the lateral direction in an operating commercial tape system can be as large as $10 \mu\text{m}$ and the frequency can be above 1000 Hz [12][14][23][26].

3.2 Feedback Control

The block diagram of the current head positioning system is shown in Fig. 3.4. The plant G represents the dynamics of the tape head plant, as given in Equation (3.1). The transfer function from the lateral tape motion displacement w_h at the head to the position error e is represented by H . It can be a unity function. There exist other highly uncorrelated noise disturbances that cannot be addressed by the feedforward controller and they are not shown in the diagram.

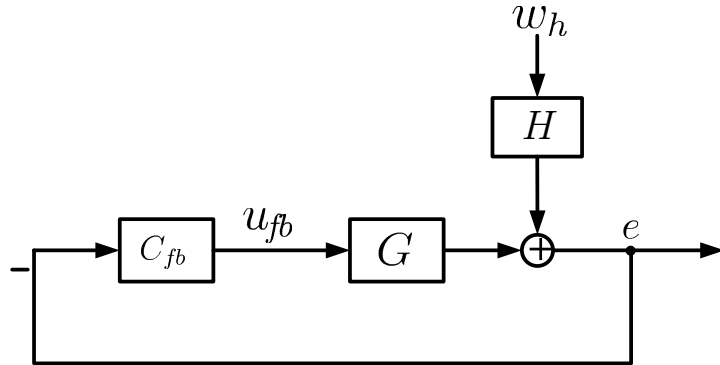


Figure 3.4: A typical head positioning system in a tape drive uses feedback control only.

3.2.1 Basic PID Controller

The feedback controller C_{fb} is usually a simple PID controller designed to guarantee system stability and address lower frequency components in the position error. In this study, we focus on developing feedforward control to further reduce the position error and use a basic PID controller

$$C_{PID} = \frac{0.01936z^3 - 0.04843z^2 + 0.0467z - 0.01701}{z^3 - 1.78z^2 + 1.449z - 0.4067}. \quad (3.2)$$

This C_{PID} yields a feedback loop with a gain margin of 5.57 dB at 859 Hz and a phase margin of 38.4 deg at approximately 390 Hz.

3.2.2 More Advanced Feedback Controller

A robust estimation and adaptive controller tuning (REACT) compensator that increases the bandwidth of the closed-loop tape head positioning servo system is developed in [6]. The REACT controller C_R is obtained by augmenting the basic PID controller C_{PID} with an additional feedback loop that can be tuned to minimize the output error, as shown in Equation (3.3),

$$C_R = \frac{C_{PID} + Q}{1 - \hat{G}Q}. \quad (3.3)$$

Here, \hat{G} is the model of the plant and Q is the tuning parameter. Theoretically, Q can be any stable transfer function. The higher order Q is, the higher order C_R would be and the better disturbance rejection performance C_R would provide.

We assume the model is perfect ($\hat{G} = G$) and design the basic PID controller as in Equation (3.2). The tuning parameter Q is chosen to be a 5th-order FIR filter that minimizes the system output e for a particular w_h signal. The obtained REACT controller is a 12th-order transfer function and creates a feedback loop with a gain margin of 3.5 dB at about 1100 Hz and a phase margin of 29.5 deg around 566 Hz. The Bode plots of the output sensitivity function of the closed-loop system with C_{PID} or C_R are shown in Fig. 3.5.

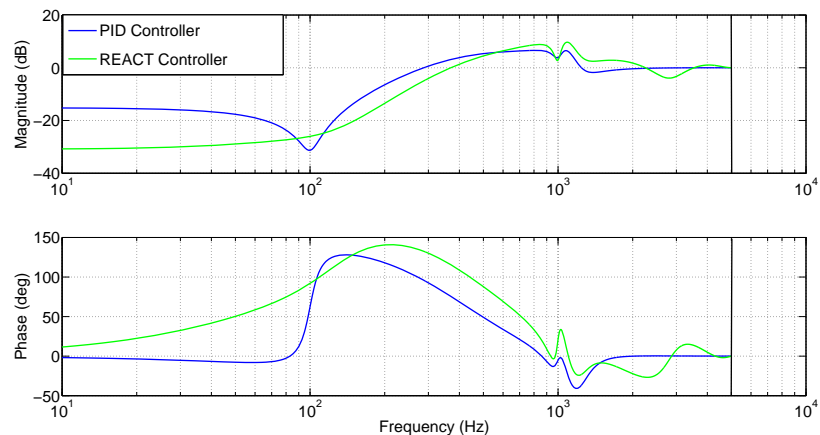


Figure 3.5: Bode plots of the output sensitivity function of the closed-loop head positioning system with C_{PID} or C_R .

3.3 Feedforward/Feedback Control Scheme

The proposed combined feedforward/feedback control architecture is illustrated in Fig. 3.6. The saturation block limits the size of the input to the plant. In this application, the magnitude of allowable current to the tape head actuator should be lower than 1 A. The feedforward controller C_{ff} generates a feedforward input u_{ff} that ideally would cancel the position error caused by the lateral tape motion disturbances. The input to the feedforward controller C_{ff} , \hat{w}_h , is the LTMD at the head estimated from the measured upstream LTMD w_u and downstream LTMD w_d near the head. The rest of this chapter focuses on controller design techniques and the LTMD estimation algorithms are discussed in Chapters 4 and 5.

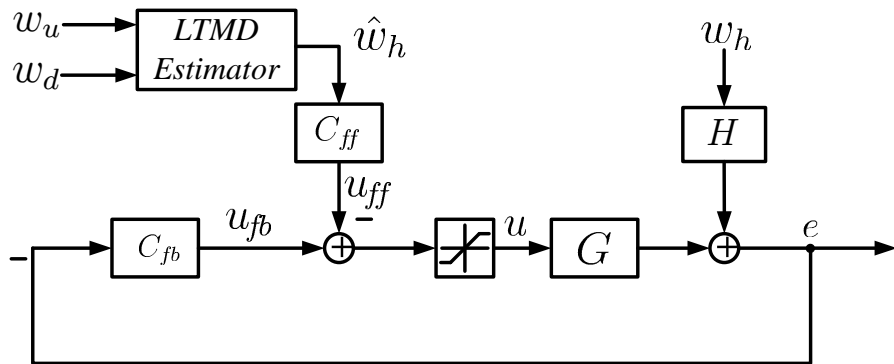


Figure 3.6: Block diagram of the combined feedforward/feedback control scheme for a tape head positioning system.

3.4 Feedforward Control Designs

To design the feedforward controller, the problem is simplified to the structure shown in Fig. 3.7 where the lateral tape motion disturbance w_h is assumed to be accessible. The focus of this section is designing the feedforward controller C_{ff} that minimizes the output position error e . In this architecture, the transfer function from the disturbance w_h to the position error e is

$$T_{ew}(z) = H(z) - G(z)C_{ff}(z). \quad (3.4)$$

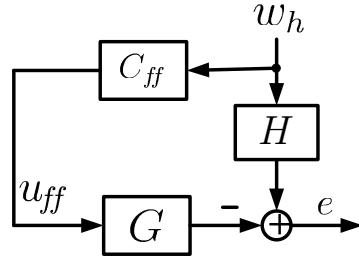


Figure 3.7: The feedforward controller C_{ff} aims to reduce the position error caused by the lateral tape motion disturbance.

Note that the transfer function G of the tape head actuator is stable and hence the feedback controller does not have to be included here. In applications where unstable plant dynamics are involved, a feedback controller is first designed to stabilize the plant (Fig. 3.8).

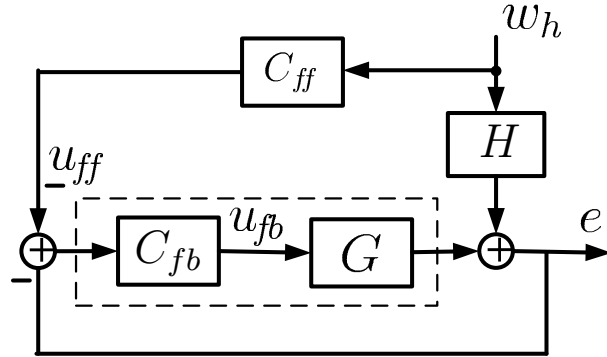


Figure 3.8: A feedback controller is included before the feedforward control is designed.

One typical design of the feedforward control is to approximate the inverse of G and compute a stable and causal approximation of $G^{-1}H$. Dynamic inversion and approximate dynamic inversion techniques have been widely studied for this purpose. Commonly used methods include the zero phase error tracking control (ZPETC) [36], the zero magnitude error tracking control (ZMETC) [30] (and references therein), and the non-causal Taylor series approximation method [22].

As an alternative to dynamic inversion, H_2 and H_∞ model matching methods can be used to find an optimal feedforward controller C_{ff} that minimizes the norm of the transfer function T_{ed} [7] [10]. A generic set of tools to solve H_2 or H_∞ preview control problems has been summarized in [11]. These different methods are investigated and compared for the studied application.

3.4.1 Approximate Dynamic Inversion Techniques

The system dynamics G includes a NMP zero at -9.52 as shown in Equation (3.1). The presence of NMP zeros complicates the inversion as the NMP zeros become unstable poles in the inverse system. Denote the numerator and denominator of the plant transfer function $G(z)$ as $b_G(z)$ and $a_G(z)$, respectively, and the relative degree of the transfer function as r_G . Denote the numerator as

$$b_n(z) = b_{sG}(z)b_{uG}(z),$$

where $b_{sG}(z)$ is the polynomial that contains all the zeros of $G(z)$ within the unit circle and $b_{uG}(z)$ is the polynomial of the NMP zeros, the plant dynamics then is

$$G(z) = \frac{b_{sG}(z)b_{uG}(z)}{a_G(z)}.$$

Approximate inversion techniques aim to seek an appropriate approximate inverse $\tilde{b}_{uG}^{-1}(z)$ of $b_{uG}(z)$ such that $b_{uG}(z)\tilde{b}_{uG}^{-1}(z) \approx 1$. The approximate inverse $\tilde{G}^{-1}(z)$ of G is then

$$\tilde{G}^{-1}(z) = \frac{a_G(z)\tilde{b}_{uG}^{-1}(z)}{b_{sG}(z)}$$

and the feedforward control becomes

$$C_{ff} = z^{-\vartheta}\tilde{G}^{-1}(z)H(z), \quad (3.5)$$

where ϑ represents the extra steps of delay that might be required to make the feedforward controller causal. In this chapter, we assume the dynamics of the disturbances are pure delays to better explain the concepts of the algorithms. The delays in $H(z)$ can (partly) fulfill the requirement of extra steps of delay ϑ . For simplicity, we consider the case where $G(z)$ contains only one NMP zero at

$z = z_0$ ($|z_0| > 1$) and $b_{uG}(z) = z - z_0$. The same techniques can be applied to find the approximate inversion of each NMP zero when the order of the polynomial $b_{uG}(z)$ is greater than one.

Besides the plant inverse, another commonly studied dynamic inversion architecture is the closed-loop inverse architecture [30] (and references therein), as shown in Fig. 3.9. In this ar-

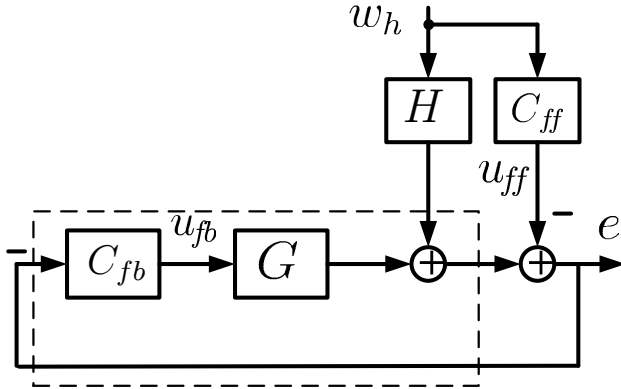


Figure 3.9: In this closed-loop inversion architecture, the feedforward controller is designed to be the (approximate) inversion of the output sensitivity function.

chitecture, the feedforward controller is designed to be the (approximate) inversion of the output sensitivity function. In the tape head positioning system application, the C_{fb} and G are both stable. Hence, the output sensitivity function is a minimum-phase system and a direct inverse can be found. It is found that the closed-loop inverse yields better disturbance rejection performance than the plant dynamic inversion architecture. However, the feedforward control input generated in this architecture is at least twice as large as that from the plant dynamic inversion architecture. To study different approximate dynamic inversion techniques, this dissertation focuses on plant dynamic inversion.

3.4.1.1 Zero Phase Error Tracking Control

The Zero Phase Error Tracking Control (ZPETC) inversion method is introduced in [36]. This method approximates the inverse by reflecting the NMP zero in the original plant about the

unit circle so as to cancel the phase shift due to the NMP zero, that is,

$$\tilde{b}_{uG}^{-1}(z) = \frac{1 - z_0 z}{(1 - z_0)^2}$$

and

$$\tilde{G}^{-1}(z) = \frac{a_G(z)(1 - z_0 z)}{b_{sG}(z)(1 - z_0)^2}.$$

Here, the gain $\frac{1}{(1-z_0)^2}$ is included to maintain unity DC gain of $G(z)\tilde{G}^{-1}(z)$. The resulting dynamic inverse is non-causal and an extra r_G+2 steps of delay needs to be added when the original plant has one NMP zero so as to form a causal feedforward controller. If the plant contains k_u NMP zeros, a total total number of r_G+2k_u extra steps of delay is needed. The phase response of $G(z)\tilde{G}^{-1}(z)$ is zero at all frequencies while the gain deviates from unity at higher frequencies.

3.4.1.2 Zero Magnitude Error Tracking Control

In contrast to the ZPETC where the NMP zero is converted to a stable zero in the inverse system, the Zero Magnitude Error Tracking Control (ZMETC) reflects the NMP zero about the unit circle and converts it to a stable pole in the inverse system [30]. Thus, the approximate inverse of $b_{uG}(z)$

$$\tilde{b}_{uG}^{-1}(z) = \frac{1}{(1 - z_0 z)}$$

and

$$\tilde{G}^{-1}(z) = \frac{a_G(z)}{b_{sG}(z)(1 - z_0 z)}.$$

To maintain the causality of the feedforward controller, an additional r_G steps of delay is needed and this number does not increase when there are more than one NMP in the plant dynamics. The product $G(z)\tilde{G}^{-1}(z)$ is

$$G(z)\tilde{G}^{-1}(z) = \frac{z - z_0}{1 - z_0 z}$$

and the magnitude response is always unity but there will be phase lag.

3.4.1.3 Non-causal Taylor Series Approximation

The non-causal Taylor series uses a non-causal, stable, Taylor series expansion to approximate the inverted unstable pole. Denote $p = \frac{z}{z_0}$,

$$b_{uG}^{-1}(z) = \frac{1}{z - z_0} = -\frac{1}{z_0} \cdot (1 - p)^{-1}.$$

Using a n_T^{th} -order Taylor series to approximate $(1 - p)^{-1}$, we have

$$\begin{aligned}\tilde{b}_{uG}^{-1}(z) &\approx -\frac{1}{z_0} \cdot (1 + p + p^2 + \cdots + p^{n_T}) \\ &= -\frac{1}{z_0} \cdot \frac{1 - p^{n_T+1}}{1 - p} \\ &= \frac{1 - (\frac{z}{z_0})^{n_T+1}}{z - z_0}\end{aligned}$$

and

$$\tilde{G}^{-1}(z) = \frac{a_G(z)}{b_{sG}(z)} \frac{1 - (\frac{z}{z_0})^{n_T+1}}{z - z_0}.$$

The resulting approximate inverse of $G(z)$ is a non-causal transfer function. The magnitude of $G(z)\tilde{G}^{-1}(z)$ is closer to unity as n_T increases and $1 - (\frac{z}{z_0})^{n_T+1}$ gets closer to 1. This algorithm requires $r_G + n_T + 1$ extra steps of delay for one NMP zero in $G(z)$. When there are k_u NMP zeros in the plant, a total number of $r_G + k_u(N_T + 1)$ extra steps of delay is required to make the feedforward controller causal.

3.4.2 Model Matching Methods

Rather than approximately inverting the plant dynamics, the model matching methods compute a feedforward controller such that either the H_2 or H_∞ norm on the transfer function $T_{ed}(z)$ (Equation (3.4)) is minimized. As our objective is to minimize the variance of the output error e (and not the maximum value) due to the disturbance w_h , we design the optimal feedforward controller $C_{ff}(z)$ by minimizing the H_2 norm¹ of the transfer function $T_{ed}(z)$, as described in the

¹ Alternatively, if the objective is to minimize the peak or maximum value of e , the feedforward control design problem can be formulated as an H_∞ norm minimization problem.

following equation [7][10][11]:

$$C_{ff}(z) = \arg \min_{C_{ff}(z) \in R\mathcal{H}_\infty} \|H(z) - G(z)C_{ff}(z)\|_2. \quad (3.6)$$

Here, $C_{ff}(z)$ is required to be stable ($\in R\mathcal{H}_\infty$) and we allow $C_{ff}(z)$ to be exactly proper. To save space, the discrete-time variable z is omitted in some of the equations discussed in the remainder of the chapter. An issue worthy of noticing here is when such an optimal feedforward controller exists.

Analytically, if $G(z)$ only has minimum-phase (MP) zeros and is exactly proper, $G(z)$ is invertible and the feedforward controller can be computed directly via

$$C_{ff}(z) = -G^{-1}(z)H(z). \quad (3.7)$$

When $G(z)$ only has MP zeros and is strictly proper, the inverse $G^{-1}(z)$ is stable but non-causal.

Denoting the relative degree of $H(z)$ as r_H , we can write

$$G(z) = G(z)z^{r_G}z^{-r_G} = \bar{G}(z)z^{-r_G},$$

where $\bar{G}(z) = G(z)z^{r_G}$ is invertible. Following (3.7), the feedforward controller is

$$C_{ff}(z) = -\bar{G}^{-1}(z)H(z)z^{r_G}$$

and $C_{ff}(z)$ is proper iff $H(z)z^{r_G}$ is proper, that is, the relative degree of $H(z)$ is greater or equal to that of $G(z)$. When $r_H \geq r_G$, the disturbance can be completely rejected for a MP system $G(z)$ as $T_{ed}(z) = 0$. In the special case of $r_G = 0$, the direct solution of the $C_{ff}(z)$ is given in (3.7). When $r_H < r_G$, whether the problem in Equation (3.6) has a non-zero solution is not that obvious.

To characterize when such a non-zero solution can be computed, we write the state-space realization of $G(z)$ and $H(z)$ as

$$G \triangleq \begin{bmatrix} A_G & B_G \\ C_G & D_G \end{bmatrix}$$

and

$$H \triangleq \begin{bmatrix} A_H & B_H \\ C_H & D_H \end{bmatrix}.$$

The transfer function $T_{ed}(z)$ in Equation (3.4) can be written in a lower Linear Fractional Transformation (LFT) formulation

$$T_{ed} = \mathcal{H}_l(P, C_{ff}) = P_{11} + P_{12}C_{ff}(I + P_{22}C_{ff})^{-1}P_{21}.$$

Here, P is the transfer function matrix that represents the augmented system of G and H in Fig. 3.7:

$$P = \begin{bmatrix} P_{11} & P_{12} \\ P_{21} & P_{22} \end{bmatrix} = \begin{bmatrix} H & G \\ -I & 0 \end{bmatrix}.$$

The state-space realization of P is

$$P \triangleq \begin{bmatrix} \begin{bmatrix} A_H & 0 \\ 0 & A_G \end{bmatrix} & \begin{bmatrix} B_H & 0 \\ 0 & B_G \end{bmatrix} \\ \begin{bmatrix} C_H & C_G \\ 0 & 0 \end{bmatrix} & \begin{bmatrix} D_H & D_G \\ -I & 0 \end{bmatrix} \end{bmatrix}.$$

The model matching methods convert the disturbance rejection problem to an optimization problem in which the feedforward controller minimizes the H_2 norm of the transfer function from the disturbance to the output.

The structures of a classic discrete-time H_2 -norm optimal control problem and the H_2 model matching problem are shown in Fig. 3.10. In the left block diagram, P_o is the plant and K_o is the optimal controller to be solved. γ_1 represents all exogenous inputs and the signal γ_2 is the control. y_1 is the controlled output and y_2 contains the measurement and reference signals. In this paper, we restrict ourselves to the full-information problem where the control signal γ_2 is generated from both the system states and the exogenous inputs. Thus, the measurements include not only the disturbance but also the states of the system. The right block diagram is topographically equivalent to the model matching problem depicted in Fig. 3.7.

The augmented system of G and H is annotated as P_f .

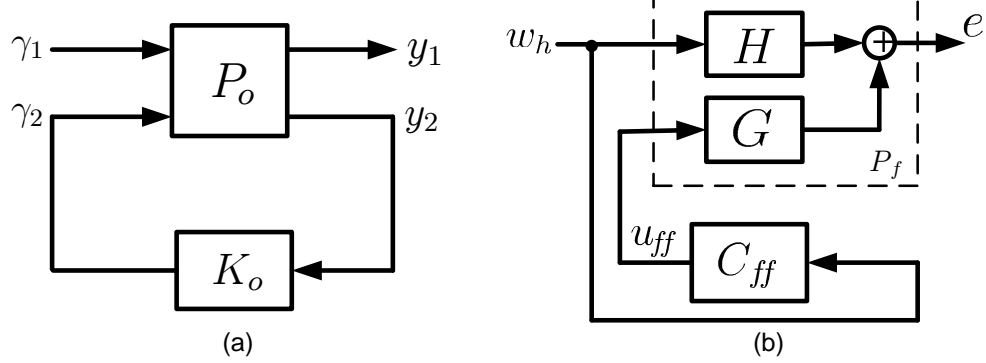


Figure 3.10: (a) The setup of the classic H_2 optimal control problem; (b) The model matching problem can be converted to an optimal control problem.

3.4.2.1 Review of H_2 Optimal Control Problem

With full-information, the state-space model of the plant P_o is

$$P_o \triangleq \begin{bmatrix} A & B_1 & B_2 \\ C_1 & D_{11} & D_{12} \\ I & 0 & 0 \\ 0 & I & 0 \end{bmatrix}. \quad (3.8)$$

The following two conditions are the necessary and sufficient conditions for existence of an H_2 optimal controller in the discrete-time domain [10][11]:

(1) (A, B_2) is stabilizable;

(2) $\begin{bmatrix} A - e^{j\theta}I & B_2 \\ C_1 & D_{12} \end{bmatrix}$ has full column rank for $\theta \in (-\pi, \pi]$.

In this structure, the control u is the combination of a state feedback and a feedforward gain over the exogenous disturbance w_h . Define the state feedback gain as K_{ox} and the disturbance feedforward gain as K_{ow} , then

$$K_{ox} = (B_2^T X B_2 + R)^{-1} (B_2^T X A + S^T) \quad (3.9)$$

and

$$K_{ow} = (B_2^T X B_2 + R)^{-1} (B_2^T X B_1 + D_{12}^T D_{11}). \quad (3.10)$$

Here, X is the solution to the Discrete Algebraic Riccati Equation (DARE):

$$X = Q + A^T X A - (A^T X B_2 + S)(B_2^T X B_2 + R)^{-1}(B_2^T X A + S^T),$$

where

$$\begin{cases} Q &= C_1^T C_1 \\ R &= D_{12}^T D_{12} \\ S &= C_1^T D_{12} \end{cases}.$$

When K_{ow} is non-zero, the feedforward control is non-trivial and it improves the disturbance rejection performance of the system.

3.4.2.2 Non-zero Solution to H_2 Model Matching Problem

In our application where the H_2 model matching method is applied, the exogenous input is the LTM disturbance d . The output position error e is the controlled output that we want to minimize. The disturbance d also plays the role of the measurement and reference. Similar to the classic H_2 optimal control problem, the model matching problem in Equation (3.6) has a solution when

- (1) $\left(\begin{bmatrix} A_H & 0 \\ 0 & A_G \end{bmatrix}, \begin{bmatrix} 0 \\ B_G \end{bmatrix} \right)$ is stabilizable;
- (2) $\left[\begin{array}{cc|c} A_H & 0 & 0 \\ 0 & A_G & B_G \\ \hline C_H & C_G & D_G \end{array} \right] - e^{j\theta} I$ has full column rank for $\theta \in (-\pi, \pi]$.

These are the generic standard conditions to compute an optimal solution.

Whether the feedforward control is non-trivial depends on the solutions of K_{ox} and K_{ow} of this problem. They can be solved by replacing the system matrices in P_o in Equation (3.9) and

(3.10) with those in P_f

$$P_f \triangleq \begin{bmatrix} \begin{bmatrix} A_H & 0 \\ 0 & A_G \end{bmatrix} & B_H & 0 \\ C_H & C_G & D_H & D_G \\ I & 0 & 0 \\ 0 & -I & 0 \end{bmatrix}.$$

The subscript f here stands for full-information.

The feedforward control has a non-trivial solution when Equation (3.10) is non-zero. Since the solution of the feedforward gain depends on the solution of the DARE equation, it is difficult to solve closed-form conditions that explicitly determine when K_{ow} is non-zero. We observe that the disturbance dynamics $H(z)$ affects the existence of the solution. More specifically,

- (1) When the disturbance dynamics $H(z)$ is more complex than a pure delay, the feedforward gain is always non-zero.
- (2) When $H(z)$ is a pure delay, the non-zero solution depends on the relative degrees of $G(z)$ and $H(z)$. Denoting the relative degree of $G(z)$ as r_G and that of $H(z)$ as r_H , then the feedforward gain is non-zero when $r_G < r_H$ [47].

Moreover, in the special case where both $H(z)$ and $G(z)$ are pure delays and $r_G < r_H$, it is obvious that the optimal solution of $C_{ff}(z)$ is $z^{r_G - r_H}$. In this case, the solution of the DARE yields a zero solution of K_{ow} while the feedback gain K_{ox} and the states actually form a feedforward controller. This situation does not apply to the tape head positioning system because the plant dynamics $G(z)$ is not a pure delay.

3.4.2.3 Augmented Model Matching

Similarly as the approximate dynamic inversion techniques, the feedforward controller in Equation (3.6) designed through the model matching method may lead to a large control signal u_{ff} that exceeds the input limit of the actuator as no penalty is imposed on the norm of $C_{ff}(z)$. To

avoid large inputs, a penalty on the control signal can be included in the design by augmenting the model matching technique with a minimization of a weighted norm of $C_{ff}(z)$. Thus, the feedforward controller is

$$C_{ff}(z) = \arg \min_{C_{ff}(z) \in R\mathcal{H}_\infty} \left\| \begin{array}{c} H(z) - G(z)C_{ff}(z) \\ C_{ff}(z)W(z) \end{array} \right\|_2. \quad (3.11)$$

Here, the stable discrete-time filter $W(z)$ acts as a weighting function for the feedforward control signal u_{ff} . By varying the weighting function, one can evaluate the trade-off between minimizing the variance of the output error e and the variance of the control signal u_{ff} .

3.5 Simulation Results

In the simulations, two sets of lateral tape motion displacement data that are measured near the head from two different industry tape drives are used as the lateral tape motion displacement w_h . These two data sets are referred as Meas. 1 and Meas. 2, respectively. The tape is running at a higher speed when obtaining Meas. 2 data set. Due to the proprietary nature of the data sets, the magnitudes are normalized so as not to divulge the actual LTMD measurements and we are not allowed to reveal the actual tape speed while the measurements are taken. Spectrum analysis shows the amplitude of w_h is on the order of 10 μm and the frequencies of the major components are within 500 Hz, as shown in Figs. 3.11 and 3.12.

3.5.1 Feedback Controller

The system shown in Fig. 3.4 is simulated with $H(z)$ being a pure delay. The PID feedback controller C_{PID} (Equation (3.2)) is enabled at 1 second and the REACT controller C_R replaces the PID feedback controller at 2 second. The simulation results of Meas. 1 data set is illustrated in Fig. 3.13. The PID controller reduces the magnitude of the position error caused by the LTM from 5 μm to about 1 μm and the root mean square (RMS) value of the position error signal is 0.33 μm . The magnitude of the PID feedback control input is about 0.01 A. The REACT feedback controller reduces the RMS value to 0.19 μm and the magnitude of the feedback control input is

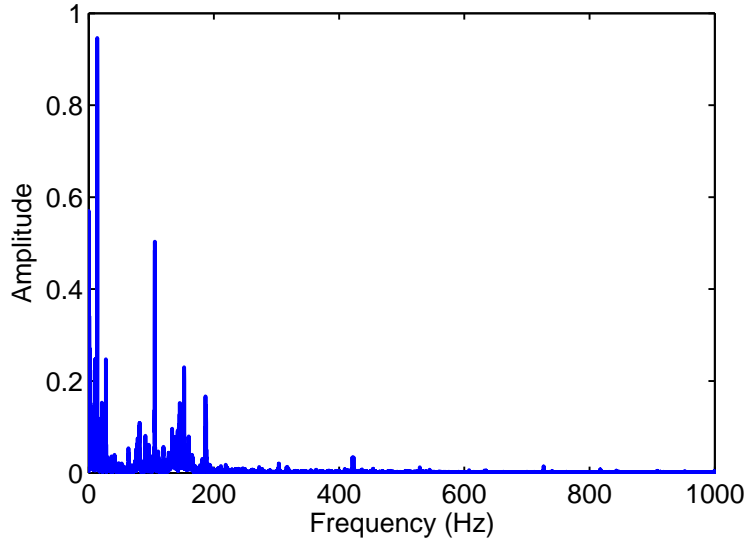


Figure 3.11: Amplitude spectrum of the first set of measured LTMD data near the head, Meas. 1.

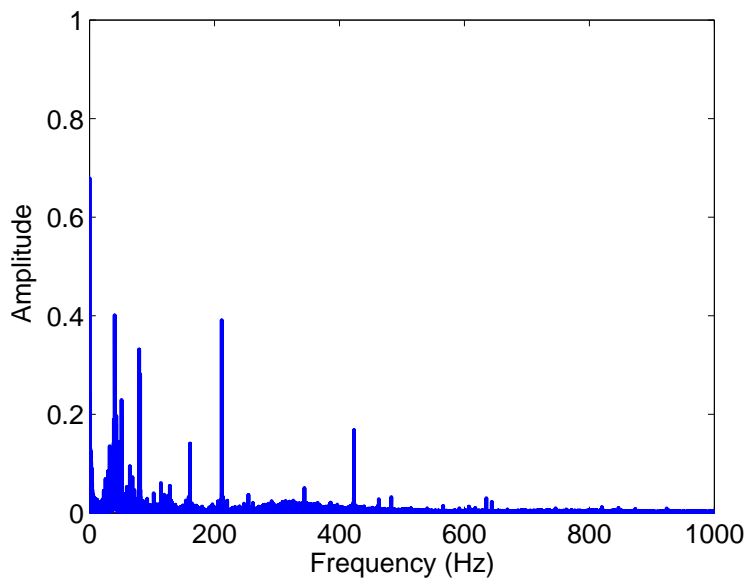


Figure 3.12: Amplitude spectrum of the second set of measured LTMD data near the head, Meas. 2. The tape is running at a higher speed than when Meas. 1 is taken.

about 0.38 A.

For the Meas. 2 data set, the PID feedback controller only reduces a small portion of the

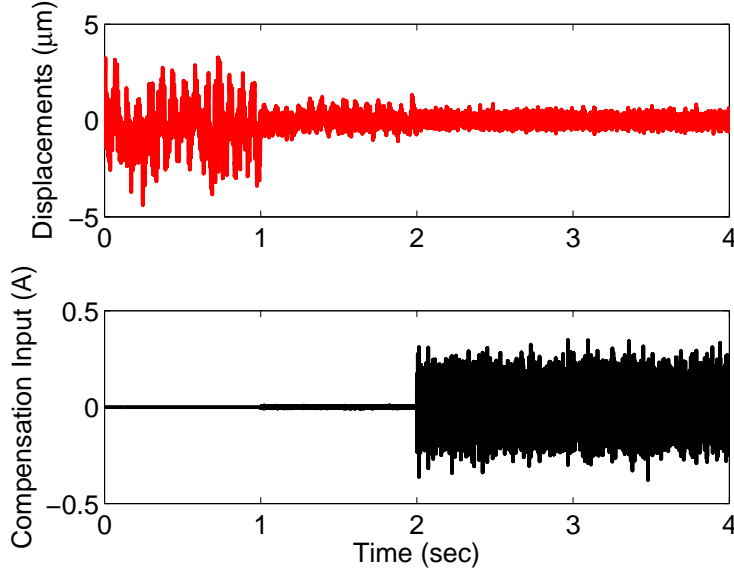


Figure 3.13: Meas. 1: The REACT feedback controller is introduced at 2 second and it further reduces the RMS of the position error signal from $0.33 \mu\text{m}$ to $0.19 \mu\text{m}$.

position error as the LTM disturbance contains a noticeable amount of energy in high frequency components that are beyond the crossover frequency at 200 Hz of the closed loop. The magnitude of the PID feedback control input is about 0.03 A and the RMS value of the position error signal is about $0.68 \mu\text{m}$. The REACT feedback controller reduces the RMS value to $0.63 \mu\text{m}$ and the magnitude of the control input is about 0.48 A. It is worthy to note that the REACT controller is designed to minimize the position error e for the Meas. 1 data set and hence its performance on the Meas. 2 data set is not as good.

3.5.2 Approximate Dynamic Inversion

To demonstrate the performance of the feedforward controller developed using different methods, we assume measurements of the lateral tape motion disturbances w_h are available in the simulations, as shown in Fig. 3.7. The disturbance dynamics $H(z)$ is a pure delay in the presented simulation results in order to demonstrate the effectiveness of the feedforward control and is chosen to be z^{-4} as an extra 4 steps of delay are needed for the second-order Taylor series approximation.

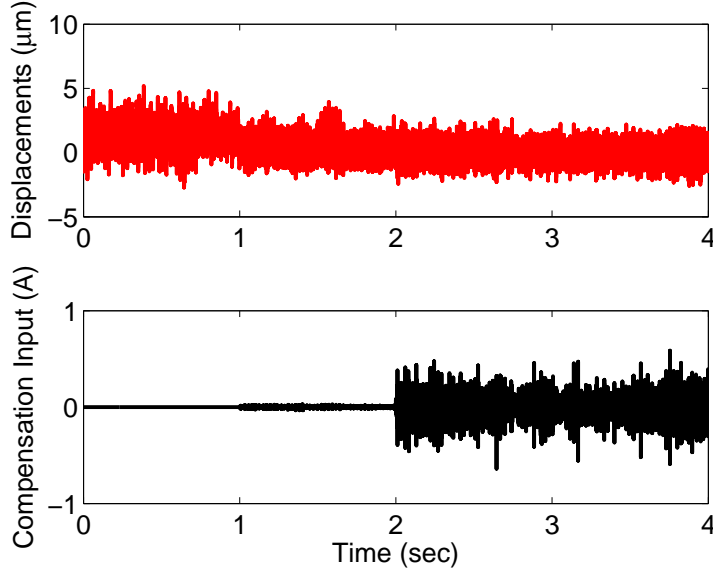


Figure 3.14: Meas. 2: Since the LTM data contains noticeable frequency content that is beyond the crossover frequency of the closed-loop, the position error is only reduced by a small proportion by the feedback controllers.

When $H(z)$ is more complex than a pure delay, C_{ff} includes the transfer function of $H(z)$ as shown in Equation (3.5). The relative degree r_G in the plant $G(z)$ (Equation (3.1)) is 1. As we discussed earlier, the feedforward controllers developed using approximate dynamic inversion techniques are non-causal and require the knowledge of the disturbance in the future. In the simulations, delays in $H(z)$ are an alternative to obtaining knowledge of the disturbance ahead of time. The feedforward controller is turned on at the time of 1 second.

Figs. 3.15, 3.16, and 3.17 illustrate the disturbance rejection performance and the control input of feedforward controllers on the Meas. 1 data set. The number of extra steps of delay required by the ZPETC controller is 3. The position error caused by the LTM is reduced by 1 order of magnitude. From Fig. 3.15, the peak-to-peak value of the generated feedforward control input is about 15 A for the ZPETC controller.

Fig. 3.16 shows that the ZMETC also reduces the disturbance by 1 order of magnitude. Unlike the ZPETC algorithm, only 1 extra step of delay is required by the ZMETC controller and

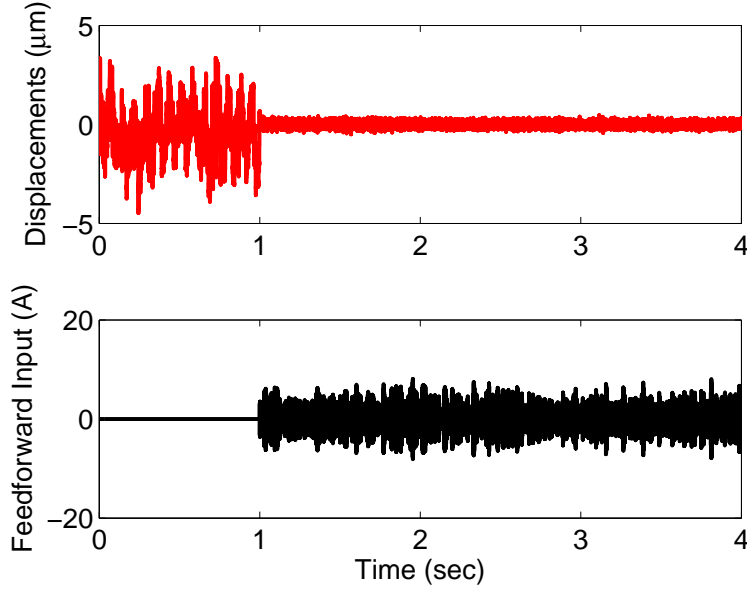


Figure 3.15: Meas. 1 data set: ZPETC feedforward controller reduces the position error to $10^{-1}\mu\text{m}$; 3 extra steps of delay are needed.

the peak-to-peak feedforward control input is in the range of 20 A.

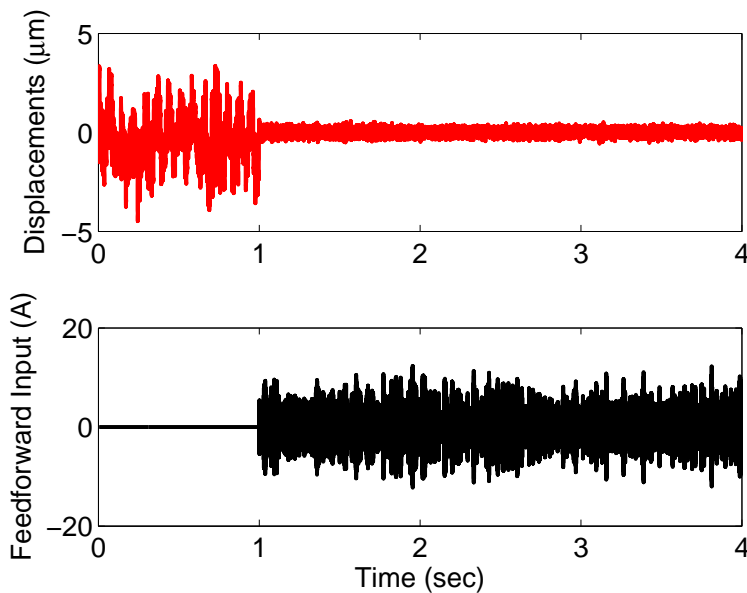


Figure 3.16: Meas. 1 data set: ZMETC feedforward controller requires 1 extra step of delay and reduces the position error to $10^{-1}\mu\text{m}$.

The simulation results of a second-order Taylor series approximation are presented in Fig. 3.17. A total number of 4 steps of extra delay is needed to make this feedforward controller causal. Comparing with the disturbance rejection when there is only a feedback controller (Fig. 3.13), this feedforward controller does not really improve the disturbance rejection performance at all while at the same time requiring large feedforward control inputs. A higher order Taylor series approximation is needed to achieve better disturbance reduction performance and more than 4 steps of extra delay will be needed.

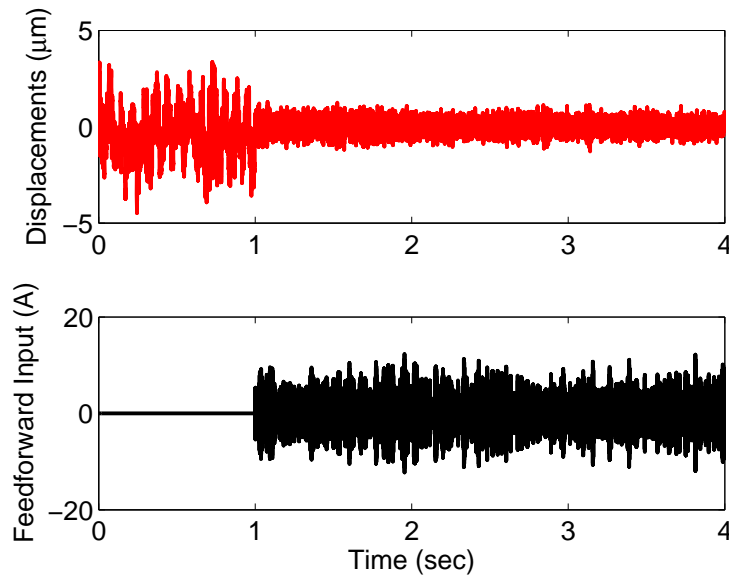


Figure 3.17: Meas. 1 data set: the feedforward controller designed using the Taylor series approximation requires large feedforward control input and does not improve the disturbance rejection performance.

The simulation results of the Meas. 2 data set are shown in Figs. 3.18, 3.19, and 3.20. Feedforward controllers improve the disturbance rejection performance when the disturbance is beyond the crossover frequency of the feedback loop.

To investigate the robustness of the approximate dynamic inversion techniques to uncertainties in the plant parameters, simulations have been run when the parameters in the plant contains a certain percentage of error. The simulation results of the ZMETC algorithm are shown in Figs.

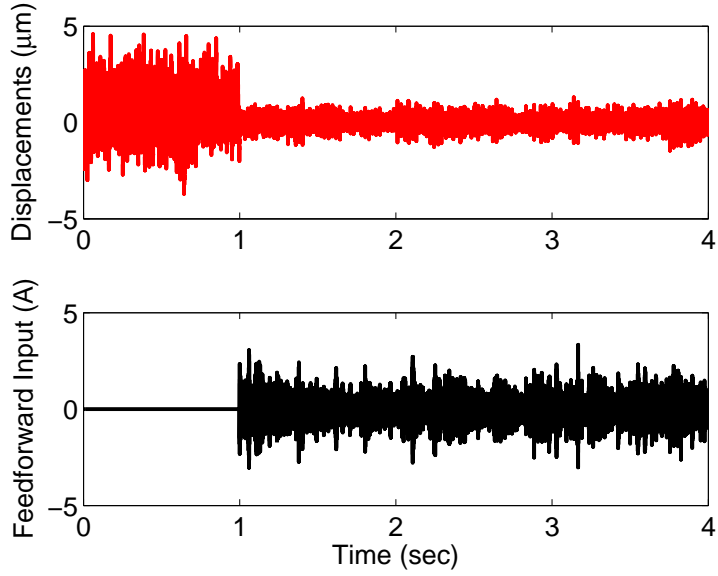


Figure 3.18: Meas. 2 data set: ZPETC feedforward controller.

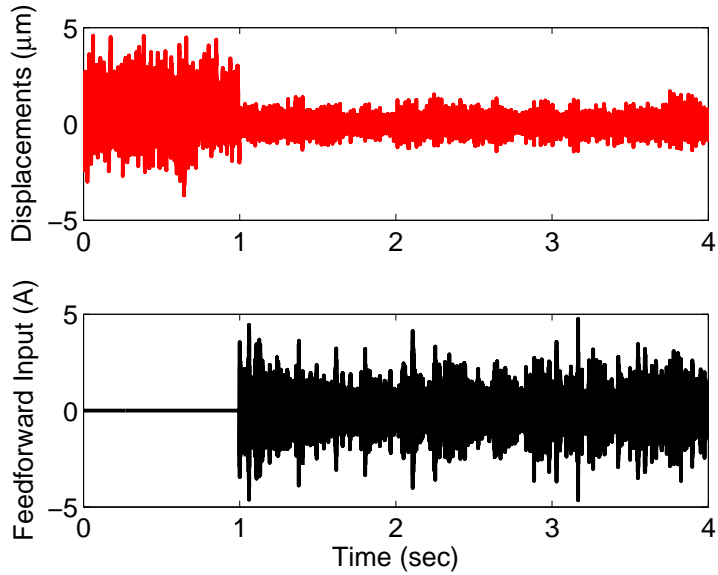


Figure 3.19: Meas. 2 data set: ZMETC feedforward controller.

3.21 and 3.22. Fig. 3.21 shows that the ZMETC algorithm reduces the disturbance by more than 80% when the gain and the zeros of the plant each contains a 10% error. However, the algorithm is

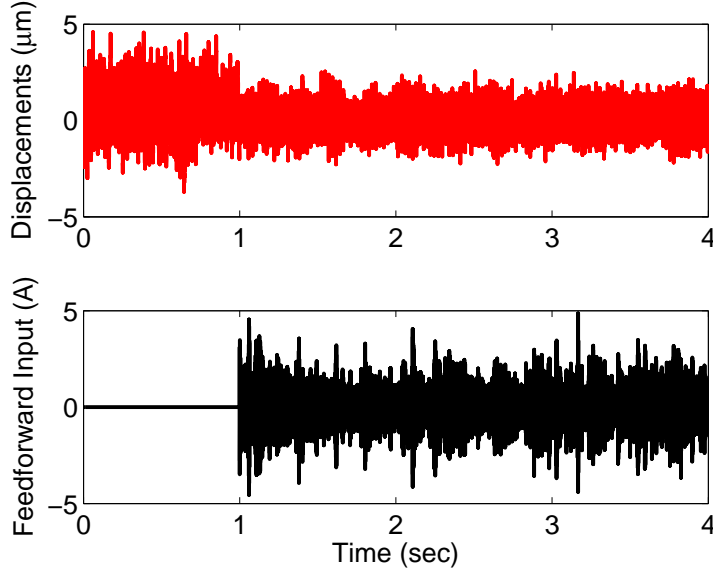


Figure 3.20: Meas. 2 data set: Taylor series approximation method.

more sensitive to uncertainties in the poles of the plant. Simulation results in Fig. 3.22 show that the feedforward controller still improves the disturbance rejection performance when the error in the plant poles is within 1%.

Approximate plant dynamic inversion techniques design the feedforward controller based on the plant dynamics. Without limiting the size of C_{ff} , the algorithms usually generate large feedforward control signals that might exceed the allowable limit (1 A in this application) to the actuator. The disturbance rejection performance will be degraded if the feedforward input is limited to not being greater than 1 A. As mentioned in Section 3.4.1, the closed-loop inverse technique generates a feedforward control input at least twice the size of the plant dynamic inversion techniques.

3.5.3 H_2 -norm Model Matching

Fig. 3.23 presents the result when the feedforward controller is solved by the model matching method in Equation (3.6) where the size of the control input is not included in the optimization.

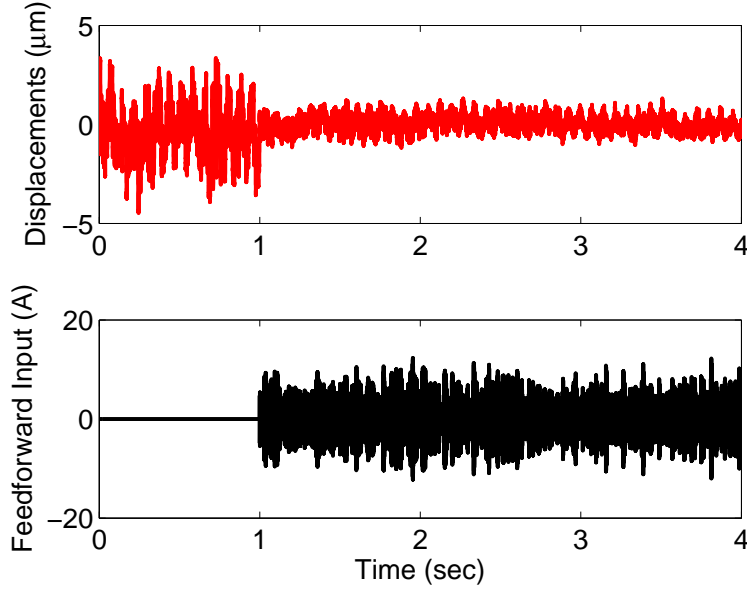


Figure 3.21: The ZMETC feedforward controller reduces the disturbance by more than 80% when the gain and the zeros of the plant contains a 10% error.

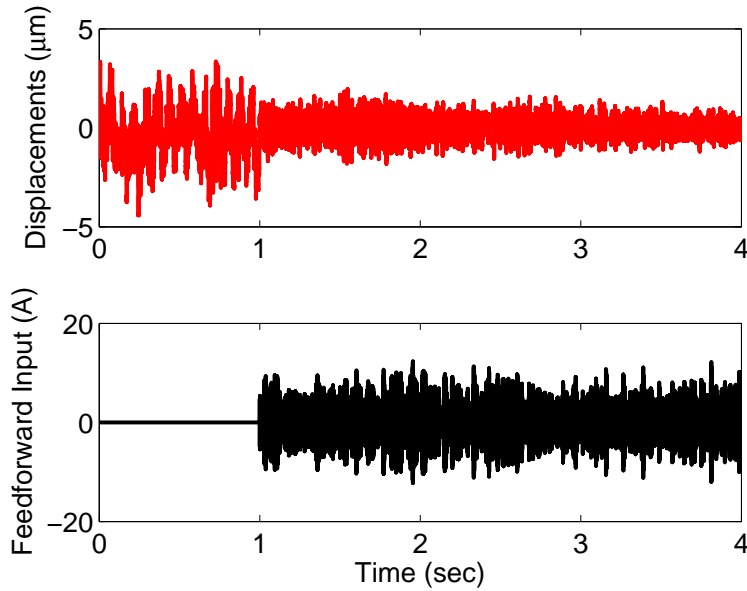


Figure 3.22: The ZMETC feedforward controller improves disturbance rejection performance when the poles of the plant each contains no more than 1% error.

The disturbance is the Meas. 1 LTM data set . The feedforward controller reduces the position error by three orders of magnitude. However, the feedforward motor current control input u_{ff} is nearly 10 A and exceeds the limit of the allowable input to the actuator.

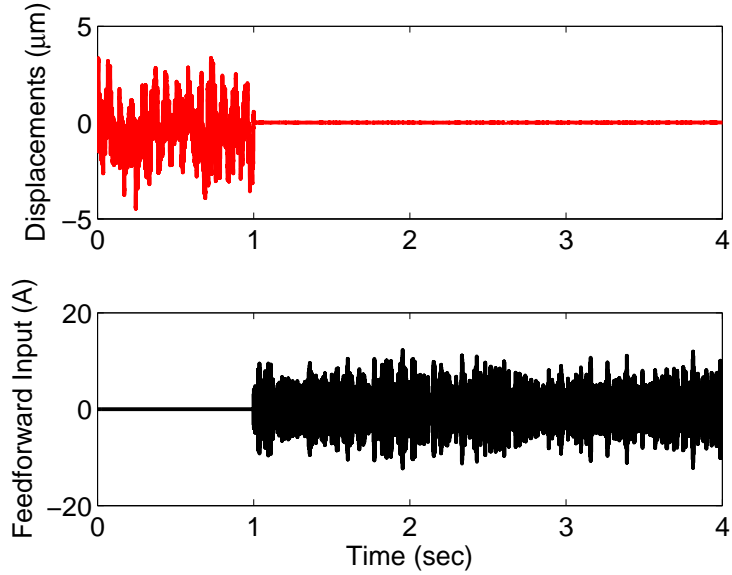


Figure 3.23: The feedforward controller is designed by the non-augmented H_2 model matching method and no penalty is imposed on the control input. The magnitude of the input current is on the order of 10 A.

To constrain the size of the feedforward input, the augmented model matching method described in Equation (3.11) is implemented. The weighting function $W(z)$ is chosen to be a second-order high-pass Butterworth filter with a cutoff frequency at 50 Hz:

$$W(z) = \frac{0.098(z-1)^2}{z^2 - 1.956z + 0.9565}.$$

The gain of the weighting function is a trade off between the size of the compensation input and the performance of the disturbance rejection.

The result in Fig. 3.24 shows the position error is reduced by more than one order of magnitude. In this case, the peak-to-peak feedforward current input is on the order of 1 A. The more penalty on the control input, the less reduction in the position error.

One possible way to offset the effects of limiting the control input is to preview the disturbance

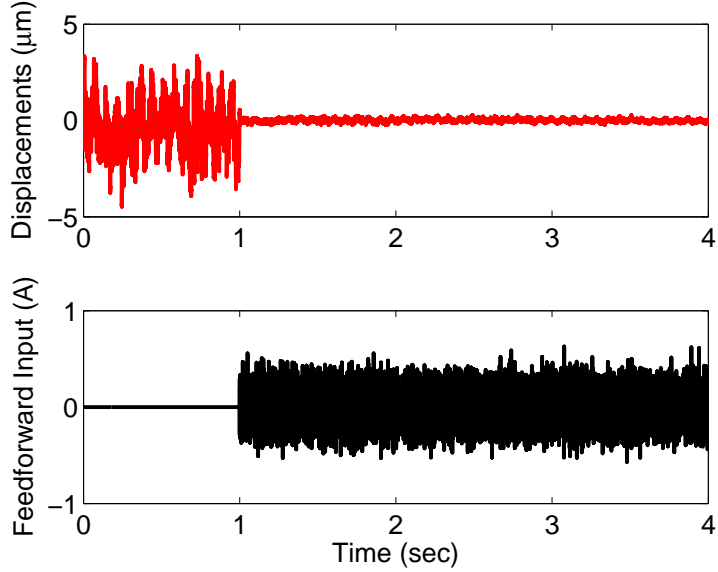


Figure 3.24: The augmented model matching method limits the size of the feedforward control input. The position error is reduced by more than one order of magnitude.

for a longer period. This is equivalent to having a larger amount of delay in the disturbance dynamics $H(z)$. Fig. 3.25 illustrates that when $H(z) = z^{-10}$, the feedforward control reduces the position error by two orders of magnitude. Here, the augmented model matching method uses the same weighting function as in the simulation of Fig. 3.24. The size of the feedforward control input is constrained to be on the order of 1 A.

The robustness of the model matching method is similar as that of the dynamic inversion techniques. The method is more robust to the uncertainties in the gain and zeros of the plant than in the poles of the plants. The simulation result in Fig. 3.26 is obtained in the same situation as in Fig. 3.24, except that the gain and the zeros of the plant each contains a 10% error. The feedforward controller still reduces the disturbance by more than one order of magnitude. The simulation results in Fig. 3.27 show that the feedforward controller improves the disturbance rejection performance of the system when the error in the plant poles is no more than 1%.

Similar simulations have been conducted on the second LTM data set Meas. 2. To restrict the size of the feedforward input, more penalty has to be imposed on the feedforward controller.

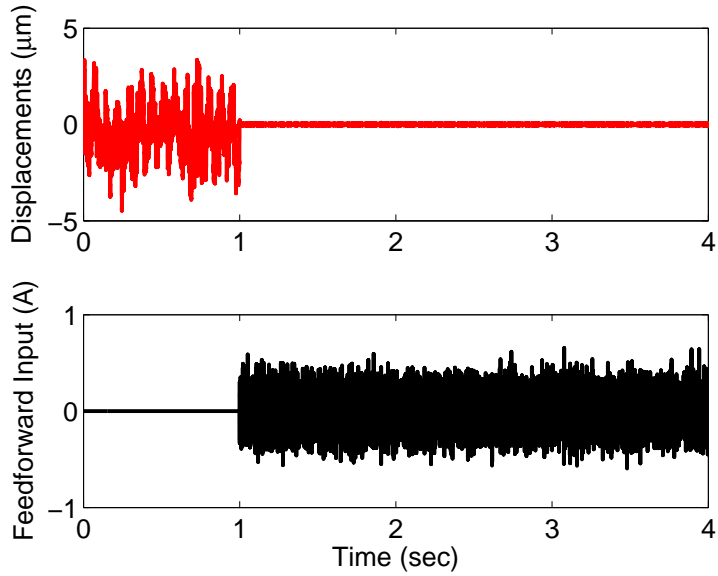


Figure 3.25: With a longer preview period, the feedforward controller reduces the position error by two orders of magnitude and the size of the control input is on the order of 1 A.

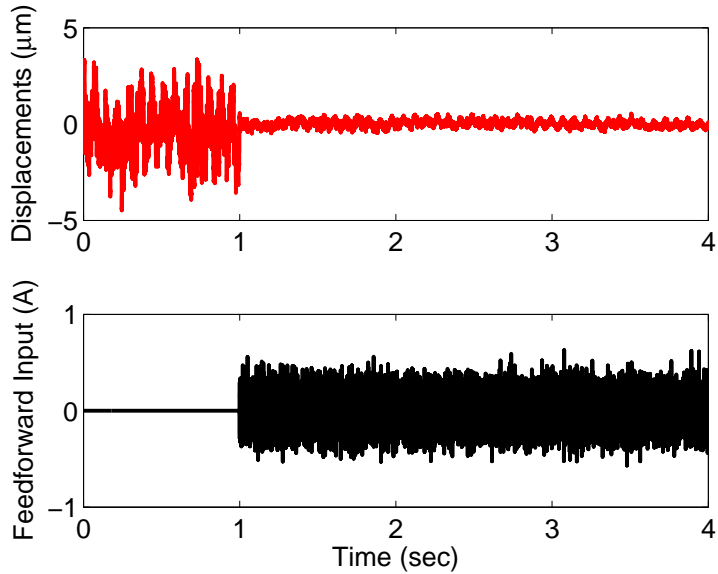


Figure 3.26: The feedforward controller solved by the augmented model matching method still reduces the position error caused by LTM disturbance when the gain and the zeros of the plant each contains a 10% error.

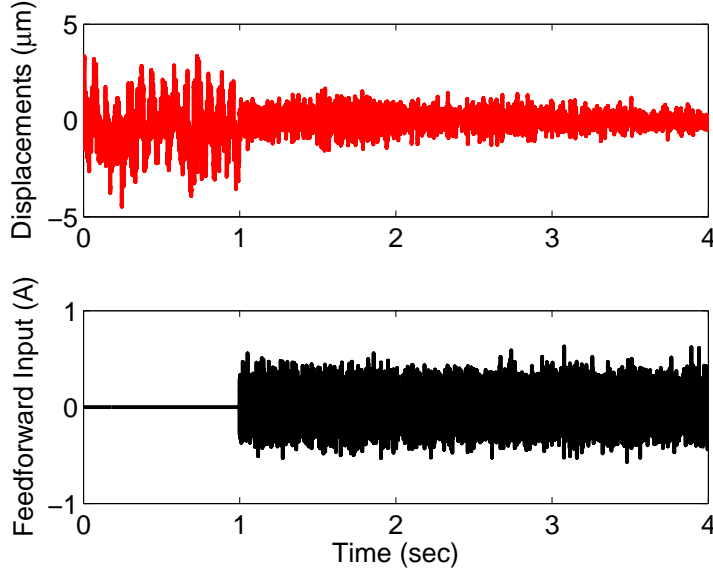


Figure 3.27: The feedforward controller reduces the position error when the poles of the plant each contains no more than 1% error.

The weighting function is similar as the one designed for the Meas. 1 data set with a larger gain.

$$W(z) = \frac{0.2445(z - 1)^2}{z^2 - 1.956z + 0.9565}.$$

As shown Fig. 3.28, the size of the feedforward input is within 1 A and the position error is reduced by more than 1 order of magnitude.

3.5.3.1 Combined Feedforward/Feedback Control

Assuming the LTM data set Meas. 1 is available, the performance of the combined feedforward/feedback control scheme is evaluated in simulation and the results are illustrated in Fig. 3.29. The PID feedback controller is enabled at 1 second and replaced by the REACT feedback controller at 2 second. The feedforward controller designed using the H_2 model matching method is added to closed-loop system at 3 second and further reduces the position error by one order of magnitude.

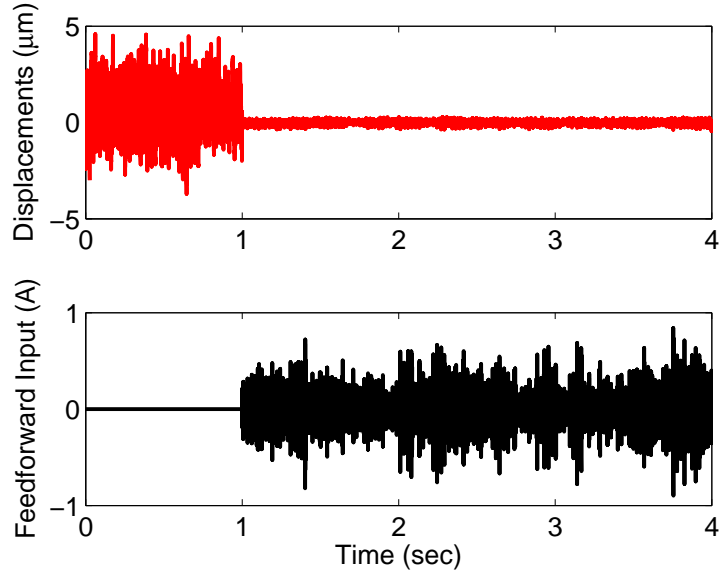


Figure 3.28: Meas. 2 data set: the feedforward controller reduces the position error by more than 1 order of magnitude while the feedforward input is restricted within the allowable range.

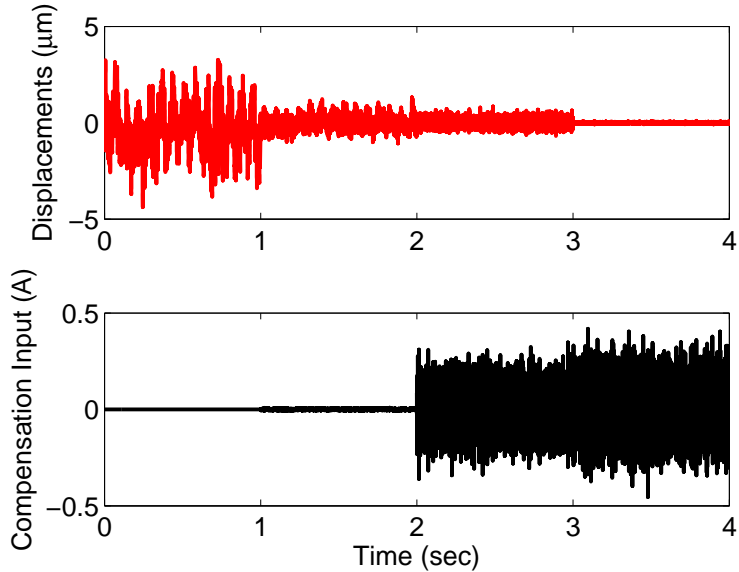


Figure 3.29: Simulation results of applying combined feedforward/feedback control scheme to Meas. 1 data set. The REACT feedback controller is designed to reduced the position error for this particular LTM data set. The feedforward controller further reduces position error by one order of magnitude.

3.6 Conclusions and Discussion

Simulation results demonstrate that if the measurements of the disturbance are available, properly designed feedforward controllers can effectively reject the lateral tape motion disturbance in the tape head positioning servo system, especially when the lateral tape motion displacement contains frequency components beyond the closed-loop crossover frequency.

Feedforward controllers designed by approximate dynamic inversion techniques are usually non-causal and yield large control inputs that might exceed the limit of allowable input to the actuator. The designs are independent of the disturbance dynamics.

The H_2 -norm model matching method converts the disturbance rejection problem to an optimization in which the feedforward controller minimizes the norm of the transfer function from the disturbance to the output. Moreover, by imposing a penalty on the norm of C_{ff} , the size of the feedforward control input can be constrained.

Chapter 4

Least Squares Algorithm to Estimate LTMD

The feedforward control requires an estimation of the LTMD at the head as its input to generate the feedforward control to the tape head that ideally would cancel the position error caused by the LTM. This chapter introduces a least squares based algorithm to estimate the LTMD w_h at the head from a history of the upstream w_u and downstream w_d LTMDs near the head. In practice, laser edge sensors may be placed at both upstream and downstream locations of the head to measure w_u and w_d , as shown in Fig. 4.1.

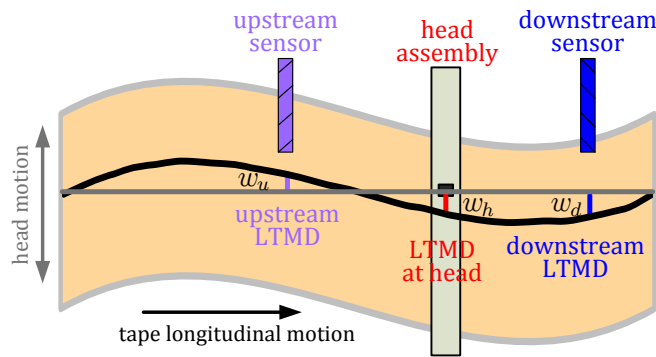


Figure 4.1: Edge sensors can be placed near the head to measure upstream and downstream lateral tape displacements.

4.1 Least Squares Algorithm

Define the vector of a sequence of k_p past upstream LTMD measurements at time step k as ${}^{k_p}\vec{w}_{u,k}$ and the vector of past downstream LTMD measurements as ${}^{k_p}\vec{w}_{d,k}$,

$${}^{k_p}\vec{w}_{u,k} = [w_{u,k-1}, w_{u,k-2}, \dots, w_{u,k-k_p}]$$

and

$${}^{k_p}\vec{w}_{d,k} = [w_{d,k-1}, w_{d,k-2}, \dots, w_{d,k-k_p}].$$

The estimation of w_h at q ($q \geq 0$) samples in advance can be computed from the history of the upstream and downstream LTMD measurements as

$$\hat{w}_{h,k+q} = \Phi_{udh} \left({}^{k_p}\vec{w}_{u,k}, {}^{k_p}\vec{w}_{d,k} \right). \quad (4.1)$$

The correlation between successive LTMDs is incorporated into the predicting function $\Phi_{udh}(\cdot)$.

We initially assume $\Phi_{udh}(\cdot)$ to be a linear function. To determine the linear predicting function $\Phi_{udh}(\cdot)$ that correlates w_u , w_d , and w_h in Equation (4.1), a least squares based algorithm is developed. Define the coefficient vectors

$$\vec{a}_u = [a_{u1}, a_{u2}, \dots, a_{uk_p}]^\top$$

and

$$\vec{a}_d = [a_{d1}, a_{d2}, \dots, a_{dk_p}]^\top,$$

where $[\cdot]^\top$ denotes the transpose of $[\cdot]$. The predicted LTMD at the head then is

$$\hat{w}_{h,k+q} = [{}^{k_p}\vec{w}_{u,k} \quad {}^{k_p}\vec{w}_{d,k}] \begin{bmatrix} \vec{a}_u \\ \vec{a}_d \end{bmatrix}. \quad (4.2)$$

Letting ${}^{k_p}\vec{w}_{ud,k} = [{}^{k_p}\vec{w}_{u,k} \quad {}^{k_p}\vec{w}_{d,k}]$ and $\vec{a}_{ud} = [a_{u1}, a_{u2}, \dots, a_{uk_p}, a_{d1}, a_{d2}, \dots, a_{dk_p}]^\top$, Equation (4.2) becomes

$$\hat{w}_{h,k+q} = {}^{k_p}\vec{w}_{ud,k} \vec{a}_{ud}.$$

The optimal value \vec{a}_{ud}^* of the coefficient vector is computed offline by

$$\begin{aligned}\vec{a}_{ud}^* &= \arg \min_{\vec{a}_{ud}} \sum_{i=0}^{M_t-1} [w_{h,k+q+i} - \hat{w}_{h,k+q+i}]^2 \\ &= \arg \min_{\vec{a}_{ud}} \sum_{i=0}^{M_t-1} \left[w_{h,k+q+i} - k_p \vec{w}_{ud,k+q+i} \vec{a}_{ud} \right]^2.\end{aligned}\quad (4.3)$$

Here, the LTMD data is measured synchronously. M_t is the total number of LTMD samples used for optimization. The least squares method minimizes the difference between the measured and predicted LTMD at the head, w_h and \hat{w}_h , respectively.

The prediction error w_{eh} is defined as

$$\begin{aligned}w_{eh,k} &= w_{h,k} - \hat{w}_{h,k} && (k > M_t + q). \\ &= w_{h,k} - k_p \vec{w}_{ud,k-q} \vec{a}_{ud}^*\end{aligned}$$

Denoting the maximum and minimum value of w_h as w_{hmax} and w_{hmin} , respectively, the normalized root mean square (NRMS) of the error then is

$$NRMS = \frac{\|w_{eh}\|_2}{\sqrt{M_s}(w_{hmax} - w_{hmin})}.$$

Here, $\|\cdot\|_2$ denotes the 2-norm and M_s is the number of samples evaluated. The NRMS of the prediction error is a metric we use to evaluate the performance of the algorithms.

It should be noted that this algorithm requires knowledge of M_t data samples of actual w_h . In general, more data points of actual w_h (larger M_t) used to solve for \vec{a}_{ud}^* and a longer history of the information vector $k_p \vec{w}_{ud,k}$ (larger k_p) lead to less prediction error. At the same time, larger M_t and k_p increases the computational complexity required to solve for the optimal value of the coefficient vector. Hence, there is a trade-off between the performance and cost of the algorithm.

4.2 Prediction Performance

We first evaluate the prediction performance of the coefficients computed by the least squares method on an artificially synthesized LTMD data set and then on an actual LTMD data set measured from an industrial tape system testbed.

4.2.1 Synthesized LTMD Data

The artificial LTMD data is synthesized by a number of sinusoidal components [5],

$$w(x, t) = \sum_{j=1}^{M_w} A_j \sin\left(\frac{2\pi}{\lambda_j}(x - vt)\right).$$

Here, x is the distance between the starting point of the tape path and the location of interest. The full length of the tape path is from the tangential point of the source reel to that of the take-up reel. $w(x, t)$ is the lateral tape motion displacement at location x and time t . v is the tape longitudinal velocity, M_w is the total number of sinusoidal components, and A_j and λ_j are the magnitude and wavelength of each component, respectively. Defining the distance between the head and the starting point of the tape path as x_h , the LTMD at the head $w_h(t)$ is then

$$w_h(t) = \sum_{j=1}^{M_w} A_j \sin\left(\frac{2\pi}{\lambda_j}(x_h - vt)\right).$$

The upstream LTMD $w_u(t)$ and downstream LTMD $w_d(t)$ can be determined in a similar way.

The synthesized LTMD data used here consists of a total of 20 different sinusoidal components, i.e., $M_w = 20$. The length of the tape path is 0.57 m, and the head is 0.27 m away from the starting point of the path, i.e., $x_h = 0.27$ m. The distance between the head and the upstream and downstream edge sensors is set to be 0.003 m, which is approximately the closest distance that photonic edge sensors can be placed next to the tape head. The tape longitudinal velocity v is 5 m/sec. The frequencies of the components are randomly chosen between 5 Hz and 1 KHz and the magnitudes are randomly picked between 0.05 and 1.

Fig. 4.2 illustrates the NRMS of the prediction error on synthesized LTMD data for different combinations of k_p and M_t values when $q = 10$. Generally speaking, larger M_t and k_p yield better prediction of the LTMD at the head. From these results, the NRMS of the prediction error is on the order of 10^{-7} when $M_t = 100$, $k_p = 10$, and $q = 10$.

4.2.2 Actual LTMD Data

The actual LTMD data set includes upstream and downstream LTMDs measured by photonic edge sensors placed near the head of an actual tape system. The data is borrowed from other

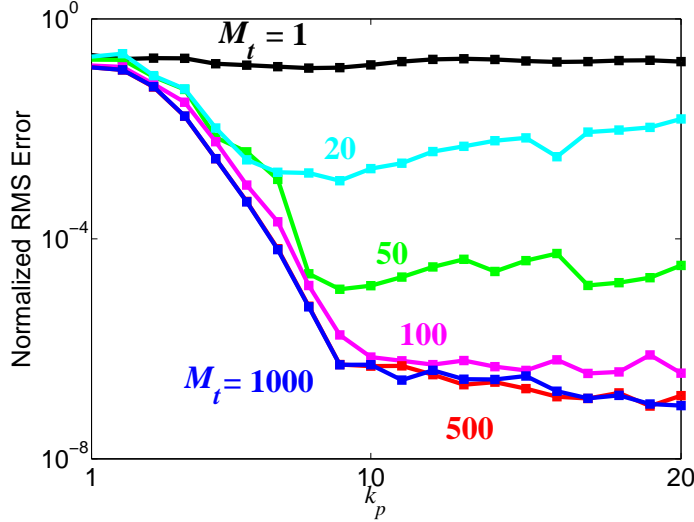


Figure 4.2: The performance of the prediction algorithm depends on M_t and k_p . From these results, $M_t = 100$ and $k_p = 10$ predicts \hat{w}_h 10 samples ahead of time reasonably well.

research and the sensors are not positioned for the purpose of estimating LTM. The purple line in the top plot of Fig. 4.3 is w_u and the blue line in the bottom plot depicts the downstream LTMD w_d . The LTMD at the head, however, is not available for the tape drive under investigation because there is not enough room to place an edge sensor at the head. Due to the proprietary nature of the data, its magnitude is normalized so as not to divulge the actual LTMD measurements. Results of spectrum analysis on the LTMD data set show that w_u and w_d contain the same frequency components.

Since the LTMD at the head of the tape drive under investigation cannot be measured at this time, the M_t samples of w_h required to solve the coefficient vector \vec{a}_{ud}^* are not available. To demonstrate the performance of the prediction algorithm, we evaluate the algorithm on actual LTMD measurements by predicting the downstream LTMD \hat{w}_d from the upstream LTMD w_u data. M_t samples of the available w_d data are used to solve for the correlation function $\Phi_{ud}(\cdot)$ for \hat{w}_d in a similar way as discussed in Section 4.2.1, using w_u only as the data vector. The prediction error w_{ed} is then computed based on the differences between the estimated \hat{w}_d and actual w_d data.

Fig. 4.4 depicts the NRMS prediction errors of using w_u data to predict the downstream

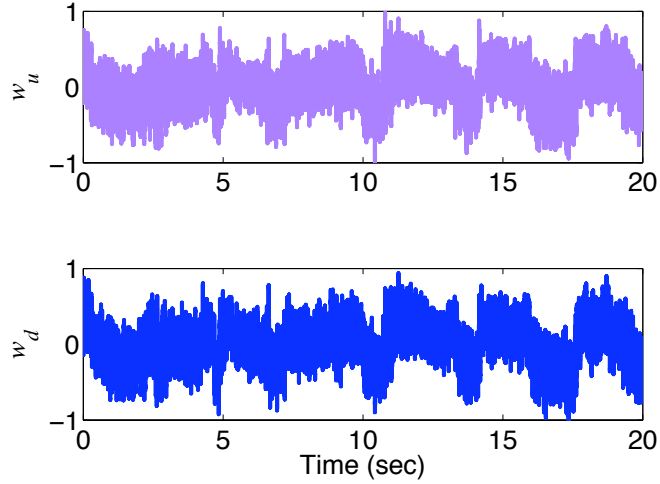


Figure 4.3: Actual upstream and downstream LTMD measurements from a tape drive system. The magnitude is normalized due to intellectual property protection reasons.

LTMD \hat{w}_d 10 samples ahead of time, with different combinations of M_t and k_p values. The NRMS of the prediction error is on the order of 10^{-2} . As seen before, larger M_t and k_p generally lead to better prediction. Considering computational efficiency, the combination of $M_t = 300$ and $k_p = 30$ yields a reasonably good predicted \hat{w}_d . When q equals 10, the NRMS is about 0.056. Fixing the values of M_t and k_p , the prediction error increases as q increases.

Note that the distance between the head and the upstream location is shorter than that between the upstream and downstream locations. Intuitively, w_h and w_u should be better correlated than w_d and w_u . Thus, the prediction algorithm should yield at least the same performance when predicting w_h from w_u , if M_t samples of w_h are available to solve for the coefficient vector.

4.3 Implementation Feasibility

There are a few concerns when implementing this algorithm on a tape drive. First, before accurate track following can occur, the least squares algorithm requires a certain length of tape to allow training data to be collected and used to determine the correlation for predicting the LTMD at the head. For the example tape system used in this dissertation in which the sampling frequency

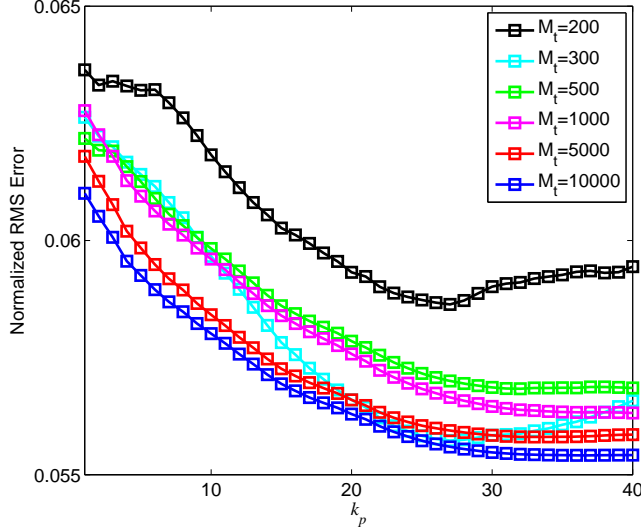


Figure 4.4: The NRMS of the prediction error w_{ed} decreases when M_t and k_p increase.

is 10 KHz and the longitudinal tape velocity is 5 m/sec, when $M_t = 300$, $k_p = 30$, and $q = 10$, the required length of tape to collect training data is about 0.15m.

Second, after collecting the training data set, the least squares problem described in Equation (4.3) is solved for \vec{a}_{ud}^* using batch processing. The total number of floating point operations needed to solve a least squares problem [37]

$$y^* = \arg \min_y \|Ay - b\|^2, \quad A \in \mathcal{R}^{m \times n} \quad (m > n)$$

is

$$flops = 2mn^2 + 2mn + n^2.$$

The computational complexity to determine \vec{a}_{ud}^* then is

$$flops = 8M_t k_p^2 + 4M_t k_p + 4k_p^2.$$

The required number of flops of the combination of M_t and k_p values depicted in Fig 4.4 are shown in Fig. 4.5.

When $M_t = 300$ and $k_p = 30$, it is about 2,200,000 flops. Assuming the speed of the DSP board used in the tape drive is 250 MHz, an approximate estimate of the calculation time is about 9 ms. This requires an additional 0.045m of tape.

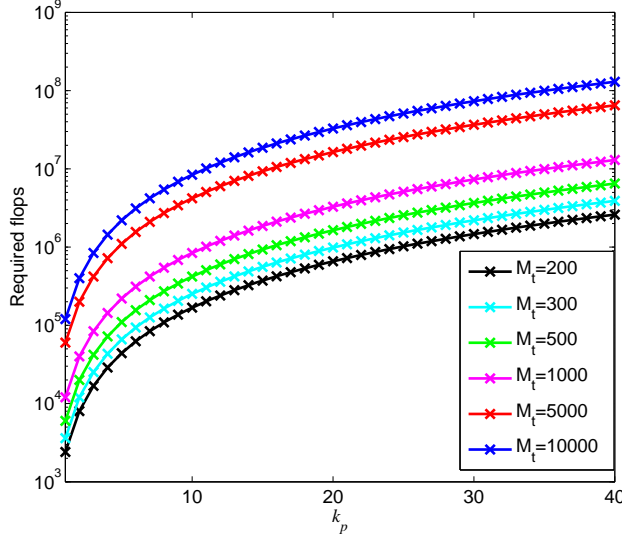


Figure 4.5: The required total number of floating point operations needed to solve the least squares problem with different combinations of M_t and k_p values.

Finally, the closer the edge sensors are placed to the head, the better correlated the successive LTMDs are. In practice, the distance between the head and the sensor is restricted by the physical size of the components. The optimal distance also depends on the online time the algorithms need to predict w_h from w_u and w_d measurements.

4.4 Polynomial Regression

Polynomial regression methods are also investigated to predict the downstream LTMD w_d from the upstream LTMD w_u . When higher-order terms of the training data are included in the regression equation, the prediction performance can be improved. At the same time, the computational complexity is significantly increased. Comparing the first-order regression and the polynomial regression including spatial quadratic and cubic terms, the prediction performance is improved by about 10% while the computational complexity is increased by 20 times. The trade-off between performance and complexity determines that polynomial regression methods are not worthwhile.

4.5 Conclusions and Discussion

The first-order least squares algorithm that predicts the LTMD at the head from a history of LTMDs measurements adjacent to the head performs well on the synthesized LTM data and it is feasible to implement on an actual tape drive system. However, the algorithm assumes the correlation between successive LTMDs are linear. In the tape system, the lateral tape motion is more complex and the correlation is a non-linear relationship. Hence, the equations of motion for lateral tape motion is worth studying to determine a more accurate correlation function to predict the LTMD at the head.

Chapter 5

Partial Differential Equation to Solve for LTMD

This chapter investigates the physical laws of lateral tape motion to solve the LTMD at the head from upstream and downstream LTMDs adjacent to the head. The partial differential equation describing the tape motion in the lateral direction for the entire tape path length is studied and modified to solve the LTMDs of a short tape segment near the head, using LTMD measurements at upstream and downstream positions as boundary conditions.

5.1 LTM Model

As discussed in Section 3.1.2, models of axially moving web have been intensively studied by researchers. In this study, we adopt the model developed in [5] [39] as it is approved and used by a number of tape industry companies. In this model, the motion of the tape in the lateral direction is modeled as a tensioned, axially moving, viscoelastic Euler-Bernoulli beam. Contributors to the lateral tape motion include disturbances from the packs, guides, and imperfectly straight tape edges.

The equation of motion is

$$\rho \left(\frac{\partial^2 w}{\partial t^2} + 2v \frac{\partial^2 w}{\partial x \partial t} + v^2 \frac{\partial^2 w}{\partial x^2} \right) - T \frac{\partial^2 w}{\partial x^2} + EI \frac{\partial^4(w - w_0)}{\partial^4 x} + \eta I \left(\frac{\partial^5(w - w_0)}{\partial^4 x \partial t} + v \frac{\partial^5(w - w_0)}{\partial^5 x} \right) = f \quad (5.1)$$

Here, w is the lateral displacement of the tape, x is the spatial position of the tape in the longitudinal direction relative to where the tape leaves the source reel, and t represents the time. ρ is the mass per unit length of the tape. EI is the bending stiffness and I is the second moment of area. η is the

loss modulus. v is the longitudinal velocity of the tape and T stands for the longitudinal tension across the tape. w_0 is the natural shape of the tape when it is stress-free.

The input of the partial differential equation, f , is the force distribution per unit of length from the guides, contact friction, and impact between the tape and any flange [5]. The friction forces between the tape and the heads are neglected since the tape almost flies over the head due to air bearing effects. In the industry, special lubrication is also applied to reduce the friction in the case when the tape touches the head.

To simulate the time dependent lateral tape motion for the tape span between the source reel and the take-up reel, a *Matlab*-based model LTMSim is developed in [5][39]. The boundary conditions are defined as the displacements and their first derivatives in the spatial domain of the two tangential points on the source reel and the take-up reel. The finite element method (FEM) is applied to discretize the equation in the spatial domain. In the time domain, the equation is integrated using the Wilson Theta method [40], an implicit integration scheme. In order to solve the LTMD at the head using upstream and downstream LTMD measurements, the model is modified to solve the lateral tape motion for a short segment of tape near the head.

5.2 Discretization in Spatial Domain - Finite Element Method

The continuous partial differential equation (5.1) is discretized in the spatial domain using the finite element method. The finite element method was first used to solve problems of stress analysis in the 1950s and has since been applied to cover a wide range of nonstructural applications like thermo-mechanics, fluid dynamics, electromagnetics, and many others [16]. It is a numerical method to determine the approximate solution of the distribution of a field variable that is difficult to obtain analytically, such as the displacements of a beam under stress. The method divides the problem domain into finite numbers of elements in a simple geometry and applies known physical laws to each element. In other words, it is a method of piece-wise approximation. All elements are then connected under proper principles. The original problem is converted to a finite number of linear algebraic simultaneous equations that can be solved numerically to yield an approximate

solution of the desired field variable.

Applications of the finite element method cover a wide range. The purpose of this section is to provide some basic knowledge about the finite element method. For a more comprehensive and in-depth understanding of FEM, one can refer to [29][17]. In this dissertation, we restrict ourselves to the specific tape drive application, where the tape is modeled as an Euler-Bernoulli beam and the desired field variable is the displacement of the tape in the lateral direction while the tape transports longitudinally. A standard procedure of applying FEM [16] is summarized and briefly discussed below.

5.2.1 Meshing

The first step in FEM is to discretize the domain, also called meshing as it generates a mesh for the problem. In this one-dimensional beam application, the tape is divided into N_e elements along the longitudinal direction, as shown in Fig. 5.1. Each element has two nodes and all the elements form the entire length of the tape path without any gap or overlap. Each node has two degrees of freedom (DOF): the lateral displacement of the tape and the first-order derivative of the displacement with respect to the longitudinal direction, also known as the rotation of the displacement. Hence, the total DOF of one element is $2 \times 2 = 4$. The density of the mesh is a

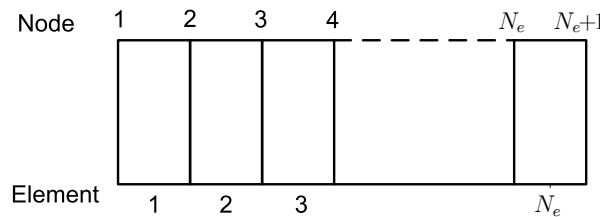


Figure 5.1: The tape path is divided into N_e elements and has $N_e + 1$ nodes. The numbers on the top of the schematic represent the nodes and at the bottom represent the elements.

trade off of the required accuracy and the available computational resources. It is common that the mesh is not uniform with a finer resolution in the area where accuracy is more critical for the analysis.

The tape path used in the simulations is illustrated in Fig. 5.2. The complete path begins at the tangential point of the source reel and ends at the tangential point of the take-up reel. In between the source reel and the take-up reel, the tape passes through roller R1, roller R2, head H1, head H2, roller R3, and roller R4, sequentially. The expanded length of the path is 57.04 cm. More details about the roller characteristics are included in Section 5.4.

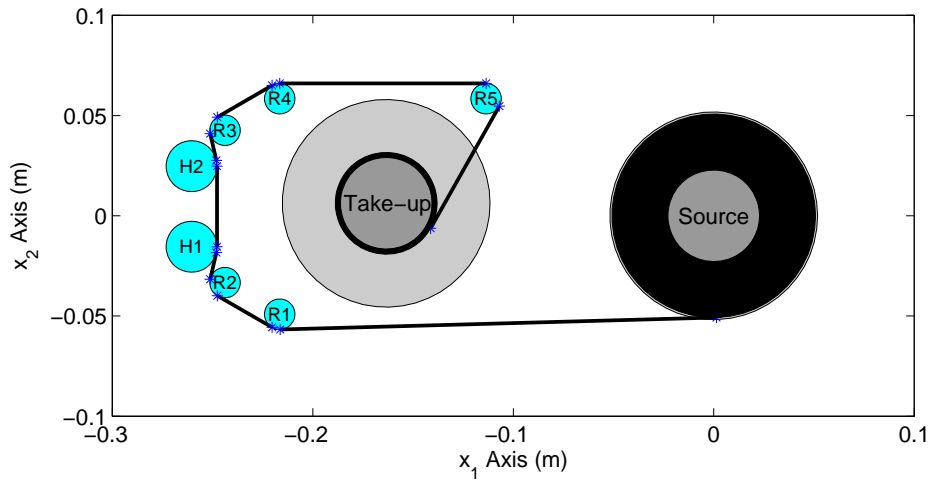


Figure 5.2: The tape path in the simulations include the source reel, the take-up reel, two head assemblies (labeled as H1 and H2 in the figure), and 5 rollers (labeled as R1, R2, R3, R4, R5).

5.2.2 Selecting Displacement Models

The finite element method converts a strong form of the problem, the governing partial differential equation (PDE) with boundary conditions, to a weak form by integrating both sides of the PDEs against a test function and applying the same boundary conditions. In other words, the problem in the strong form is converted to a weighted residual problem. Instead of finding the exact solution everywhere in the defined domain as requested by the strong form, the goal of the

weak form is to seek a solution that satisfies the strong form on average over the domain.

In our application, a trial function w is defined as the solution of the problem in the form of

$$w = \sum_{i=1}^N \alpha_i(t) \phi_i(x). \quad (5.2)$$

Here, $\phi_i(x)$ are the basis functions in the spatial domain and $\alpha_i(t)$ is the unknown function in time-domain. N is the number of nodes. The same basis functions are used to construct the test function

$$\kappa = \sum_{j=1}^N \phi_j(x). \quad (5.3)$$

The problem now is to solve the unknown variables $\alpha_i(t)$ and then find a solution of the displacements.

The displacement within an element is assumed to be a linear polynomial interpolation of the displacements at the two nodes. As mentioned earlier, one beam element contains four degrees of freedom. Subsequently, four basis functions are needed for each element: the tape deflection in the lateral direction w_i and the spatial derivative θ_i of the deflection at each of the two nodes. The basis functions are chosen to be a set of constant coefficient cubic basis functions commonly used in beam analysis. The characteristics of the basis functions are discussed in [16].

Define ξ as the spatial variable in the local coordinate of element i

$$\xi = \frac{x - x_i}{x_{i+1} - x_i}, x \in [x_i, x_{i+1}].$$

Here, x_i is the distance between the left node of the element of interest and the first node of the entire path and x_{i+1} the corresponding distance from the right node.

For one element, the trial function w^e can also be written as a polynomial of ξ in the form of

$$w^e(\xi) = c_0 + c_1\xi + c_2\xi^2 + c_3\xi^3 \quad (5.4)$$

and the first-order derivative in the spatial domain is

$$w^{e'}(\xi) = c_1 + 2c_2\xi + 3c_3\xi^2.$$

Note that $/$ indicates spatial derivative and \cdot indicates derivative in the time domain. The superscript e denotes element. At the same time, the displacement of the element is assumed to be a linear polynomial interpolation of the displacements at the two nodes. Define w_1^e as the first displacement at the beginning node of one element and w_2^e as the first-order spatial derivative of the beginning node. Define w_3^e as the first displacement at the ending node of the same element and w_4^e as the first-order spatial derivative of the ending node. Thus,

$$\begin{aligned} w_1^e &= w^e|_{\xi=0} = c_0 \\ w_2^e &= w^{e\prime}|_{\xi=0} = c_1 \\ w_3^e &= w^e|_{\xi=1} = c_0 + c_1 + c_2 + c_3 \\ w_4^e &= w^{e\prime}|_{\xi=1} = c_1 + 2c_2 + 3c_3 \\ \begin{bmatrix} c_0 \\ c_1 \\ c_2 \\ c_3 \end{bmatrix} &= \begin{bmatrix} 1 & 0 & 0 & 0 \\ 0 & 1 & 0 & 0 \\ 1 & 1 & 1 & 1 \\ 0 & 1 & 2 & 3 \end{bmatrix}^{-1} \begin{bmatrix} w_1^e \\ w_2^e \\ w_3^e \\ w_4^e \end{bmatrix}, \end{aligned} \quad (5.5)$$

Plugging Equation (5.5) into Equation (5.4) and re-arranging the components with respect to the vector $[w_1^e \ w_2^e \ w_3^e \ w_4^e]$ gives

$$w^e(\xi) = \begin{bmatrix} 1 & 0 & -3 & 2 \\ 0 & 1 & -2 & 1 \\ 0 & 0 & 3 & -2 \\ 0 & 0 & -1 & 1 \end{bmatrix} \begin{bmatrix} 1 \\ \xi \\ \xi^2 \\ \xi^3 \end{bmatrix} \quad (5.6)$$

The four basis functions are the coefficients for vector $[w_1^e \ w_2^e \ w_3^e \ w_4^e]$

$$\begin{aligned} \phi_1^e &= 1 - 3\xi^2 + 2\xi^3 \\ \phi_2^e &= \xi - 2\xi^2 + \xi^3 \\ \phi_3^e &= 3\xi^2 - 2\xi^3 \\ \phi_4^e &= -\xi^2 + \xi^3 \end{aligned}$$

5.2.3 Deriving Elemental Matrices

The partial differential equation in (5.1) can be applied to each element. Define the length of the element as d_e , the matrix form of the equation of motion of one element can be achieved by substituting the w in the equation with the formula in Equation (5.2) and integrating both sides of the equation against the test function in Equation (5.3) over the length of the element. Equation (5.1) of one element becomes

$$\rho \mathbf{M}^e \ddot{\boldsymbol{\alpha}}^e + (\eta I \mathbf{K}_{EI}^e + 2\rho_u v \mathbf{S}^e) \dot{\boldsymbol{\alpha}}^e + (EI \mathbf{K}_{EI}^e + (\rho_u v^2 - T) \mathbf{K}_T^e + \eta I \mathbf{H}^e) \boldsymbol{\alpha}^e = \mathbf{F}^e \quad (5.7)$$

Here, $\boldsymbol{\alpha}^e = [\alpha_1^e \ \alpha_2^e \ \alpha_3^e \ \alpha_4^e]$ is the nodal displacements vector corresponding to the basis functions $\phi_i^e (i = 1, 2, 3, 4)$. Since the equation has been discretized in the spatial domain, $\boldsymbol{\alpha}^e$ is a single variable function of t in the time domain. The equivalent force vector applied to the node is

$$\mathbf{F}_i^e = \int_0^{d_e} \left[f^e + EI \frac{\partial^4 w_0}{\partial^4 x} + \eta I \left(\frac{\partial^5 w_0}{\partial^4 x \partial t} + v \frac{\partial^5 w_0}{\partial^5 x} \right) \phi_i \right] dx, \quad i = 1, 2, 3, 4.$$

Here, f^e is the nodal force on the element and the natural shape w_0 of the tape is pre-defined and known. The elemental matrices in Equation (5.7) are obtained by integrating the higher-order derivative terms by parts [5].

$$\begin{aligned} \mathbf{M}_{i,j}^e &= \int_0^{d_e} \phi_i^e \phi_j^e dx, \\ \mathbf{K}_{EI,i,j}^e &= \int_0^{d_e} \phi_i^{e''} \phi_j^{e''} dx, \\ \mathbf{S}_{i,j}^e &= \int_0^{d_e} \phi_i^{e''} \phi_j^e dx, \\ \mathbf{K}_T^e &= \int_0^{d_e} \phi_i^{e'} \phi_j^{e'} dx, \\ \mathbf{H}_{i,j}^e &= \int_0^{d_e} \phi_i^{e'''} \phi_j^{e''} dx. \end{aligned}$$

5.2.4 Obtaining Global Matrices

The global matrices are formed from the elemental matrices based on the fact that two adjacent elements share one node and the displacement at a node is the same for both adjacent

elements. For example, node 2 is the common node of element one and element two (Fig. 5.1).

Define the elemental mass matrix M^e as

$$M^e = \begin{bmatrix} M_1^e & M_2^e \\ M_3^e & M_4^e \end{bmatrix}.$$

The first and second column corresponds to the displacement vector of the first and second node in the element, respectively.

In order to explain how the global mass matrix is formed from M^e , we work through an example in which the mesh contains only two elements. The first element has two nodes, annotated as Node 1 and Node 2. The first block column in M^e corresponds to the displacement vector of Node 1 and the second block column corresponds to that of Node 2. The two nodes in the second element are Node 2 and Node 3. The first block column in the elemental matrix of the second element corresponds to the displacement vector of Node 2 and the second block column corresponds to that of Node 3. Since both elements share Node 2, the global mass matrix for this mesh with 2 elements and 3 nodes is

$$\mathbf{M} \Big|_{3 \text{ Nodes}} = \begin{bmatrix} M_1^e & M_2^e & 0 \\ M_3^e & M_4^e + M_1^e & M_2^e \\ 0 & M_3^e & M_4^e \end{bmatrix}.$$

The vertical bar in the equation above is the evaluation symbol. Thus, the global mass matrix \mathbf{M} for a mesh that contains N nodes is

$$\mathbf{M} \Big|_{N \text{ Nodes}} = \begin{bmatrix} M_1^e & M_2^e & 0 & 0 & \cdots & \cdots & 0 \\ M_3^e & M_4^e + M_1^e & M_2^e & 0 & \cdots & \cdots & 0 \\ 0 & M_3^e & M_4^e + M_1^e & M_2^e & 0 & \cdots & 0 \\ \vdots & \ddots & \ddots & \ddots & \ddots & \ddots & \vdots \\ 0 & \cdots & 0 & M_3^e & M_4^e + M_1^e & M_2^e & 0 \\ 0 & \cdots & \cdots & 0 & M_3^e & M_4^e + M_1^e & M_2^e \\ 0 & 0 & \cdots & \cdots & 0 & M_3^e & M_4^e \end{bmatrix}.$$

The matrix has N block columns and each block column corresponds to the displacement of a node.

Other global matrices can be formed in a similar way. In this dissertation, the evaluation symbol is omitted when the matrix is for a mesh with N nodes.

The matrix form of the equation of motion for the entire tape path becomes:

$$\rho_u \mathbf{M} \ddot{\boldsymbol{\alpha}} + (\eta I \mathbf{K}_{EI} + 2\rho_u v \mathbf{S}) \dot{\boldsymbol{\alpha}} + (EI \mathbf{K}_{EI} + (\rho_u v^2 - T) \mathbf{K}_T + \eta I \mathbf{H}) \boldsymbol{\alpha} = \mathbf{F} \quad (5.8)$$

Here, $\boldsymbol{\alpha} = [\boldsymbol{\alpha}_1, \boldsymbol{\alpha}_2, \dots, \boldsymbol{\alpha}_N]$ includes the nodal displacements.

5.2.5 Solving for Unknown Displacements

The two boundary points of the entire tape path are the tangential points where tape contacts the source-reel and the take-up reel. The conditions of these two points are discussed and applied in [5] to solve the displacement of the entire tape path. In this dissertation, the goal is to solve the lateral tape displacement of a shorter segment around the head and the boundary points become the two ends of the segment. different. We will discuss more about this in Section 5.4.

5.3 Numerical Integration - Wilson Theta Method

Discretization of the equation in the spatial domain yields an ordinary differential equation in the time domain, as shown in Equation (5.8). The general form of the equations of motion for a multi-degree freedom system is

$$M \ddot{X} + C \dot{X} + K X = F(t). \quad (5.9)$$

Here, M is the mass matrix, C is the damping matrix, and K the stiffness matrix. F represents the sum of forces applied to the system.

A numerical procedure is applied to approximately solve the equation of motion when a closed-form solution cannot be obtained. The numerical solution satisfies the differential equation only at specified discrete time samples with an interval of Δt . Within the time interval Δt , a specific type of variation of X , \dot{X} , and \ddot{X} is assumed. The Wilson Theta method assumes that the

acceleration of the system varies linearly between two instants of time, as illustrated in Figure 5.3.

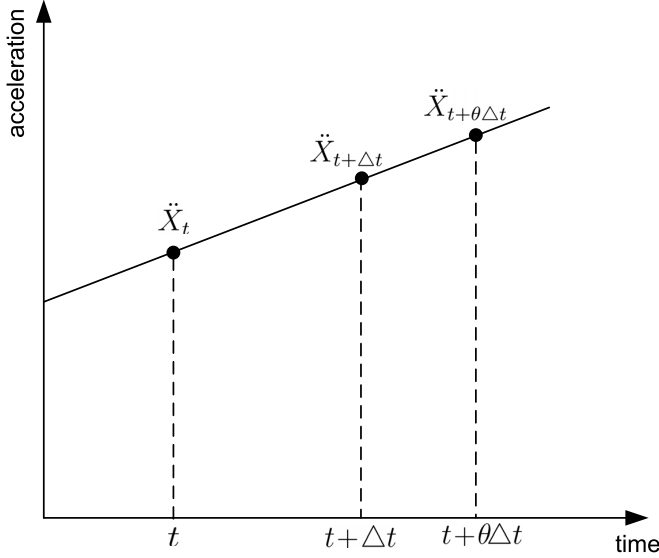


Figure 5.3: Wilson Theta method assumes that the acceleration of the system varies linearly between two instants of time.

Define τ ($\tau \in [0, \theta\Delta t]$, $\theta > 1$) as the time increment between time t and $t + \theta\Delta t$, then the acceleration between time interval t and $t + \theta\Delta t$ can be described in the following equation:

$$\ddot{X}_{t+\tau} = \ddot{X}_t + \frac{\tau}{\theta\Delta t} (\ddot{X}_{t+\theta\Delta t} - \ddot{X}_t). \quad (5.10)$$

Upon successive integration of this equation with respect to time, the first derivative of X at time $t + \tau$ is

$$\dot{X}_{t+\tau} = \dot{X}_t + \ddot{X}_t \tau + \frac{\tau^2}{2\theta\Delta t} (\ddot{X}_{t+\theta\Delta t} - \ddot{X}_t) \quad (5.11)$$

and X at time $t + \tau$ is

$$X_{t+\tau} = X_t + \dot{X}_t \tau + \frac{\tau^2}{2} \ddot{X}_t + \frac{\tau^3}{6\theta\Delta t} (\ddot{X}_{t+\theta\Delta t} - \ddot{X}_t). \quad (5.12)$$

Substituting X and \dot{X} in Equation (5.9) with Equations (5.12) and (5.11) and replacing τ with $\theta\Delta t$, Equation (5.9) at time $t + \theta\Delta t$ is

$$\ddot{X}_{t+\theta\Delta t} K_{eff} = F_{eff} \quad (5.13)$$

Here,

$$K_{eff} = M + C \frac{\theta \Delta t}{2} + K \frac{(\theta \Delta t)^2}{6}$$

and

$$F_{eff} = F_{t+\theta \Delta t} - K X_t - (C + K \theta \Delta t) \dot{X}_t - \left(C \frac{\theta \Delta t}{2} + K \frac{(\theta \Delta t)^2}{3} \right) \ddot{X}_t.$$

Once $\ddot{X}_{t+\theta \Delta t}$ is solved, the derivative of X at time $t + \Delta t$ is obtained through

$$\ddot{X}_{t+\Delta t} = \ddot{X}_t + \frac{1}{\theta} (\ddot{X}_{t+\theta \Delta t} - \ddot{X}_t).$$

By replacing the $t + \tau$ in Equations (5.11) and (5.12) with $t + \Delta t$, we obtain $\dot{X}_{t+\Delta t}$ and $X_{t+\Delta t}$, respectively.

5.4 Simulation Results

The lateral tape motion of the entire tape path length is first simulated in *LTMSim*. Using the simulated LTMDs at upstream and downstream positions adjacent to the tape as the boundary conditions, the partial differential equation of the lateral tape motion near the head is solved.

5.4.1 Full Path Simulation

The characteristics of the rollers in the path are chosen in a range that represents different types of rollers used in the industry. Due to intellectual property restrictions, no detailed descriptions are included in this thesis. The solution method generally works independently of these details. The five rollers shown in Fig. 5.2 are

- Roller R1: roller with a runout appearing at the roller rotating frequency.
- Roller R2: roller with an impulse runout lasting for 0.001 seconds.
- Roller R3: roller with a runout at the roller rotating frequency and its second and third harmonics.
- Roller R4: roller with an impulse runout lasting for 0.002 seconds where the force magnitude is 15 times of Roller 2.

- Roller R5: smooth roller that transmits no edge guiding force to the tape.

Generally, the smaller the element size is, the more accurate the simulation results are and the more complex the computation is. To investigate the trade-off of computational complexity and simulation accuracy, the LTMDs along the entire path are simulated when the number of elements N_e of the mesh varies from 50 to 200 and the mesh is uniform. Considering the simulated LTMDs when $N_e = 200$ as the most accurate results, the root mean square error of the LTMDs simulated with different N_e values are shown in Fig. 5.4. The root mean square error is not monotonic due

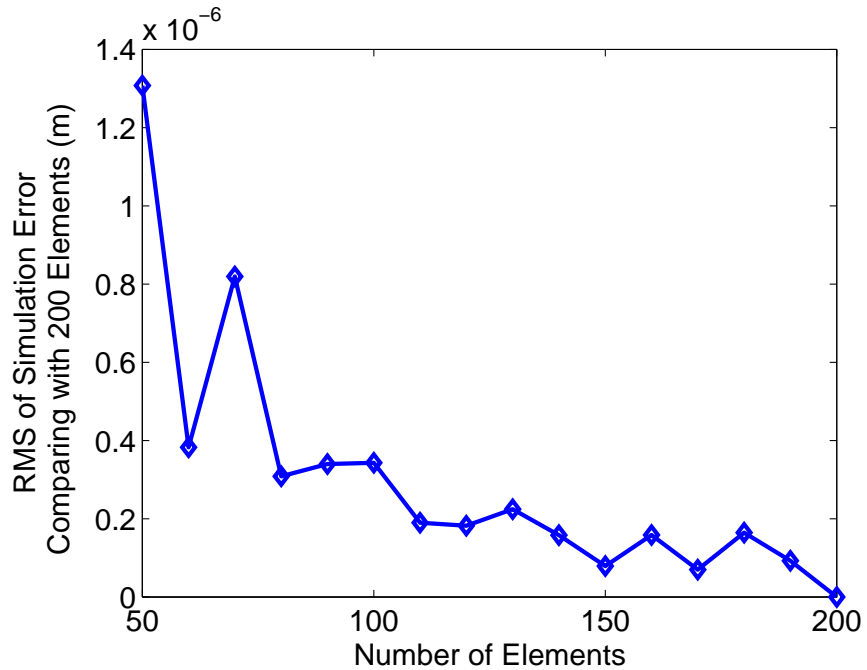


Figure 5.4: When the number of elements increases, the simulation is generally more accurate.

to the complexity of the physical process.

In this research, we initially choose $N_e = 130$ as the maximum number of elements of the tape path mesh. The evaluation of simulation errors versus number of elements was conducted after most of the analysis of the simulation results with $N_e = 130$ was completed. Though a larger number of elements yields less simulation errors, it does not change the analysis method of the simulation results. Hence, the results of $N_e = 130$ are included in this dissertation.

Since our ultimate focus is on LTMDs near the second of the two heads (labeled as H2 in Fig. 5.2), the mesh density of the short tape segment centered at the head is higher than other segments along the path for more accurate simulation results. More specifically, the entire tape span is discretized to 130 elements in a non-uniform mesh. The size of each element is shown in Fig. 5.5. The mesh is denser in the two tape spans adjacent to head H2. The RMS of the relative

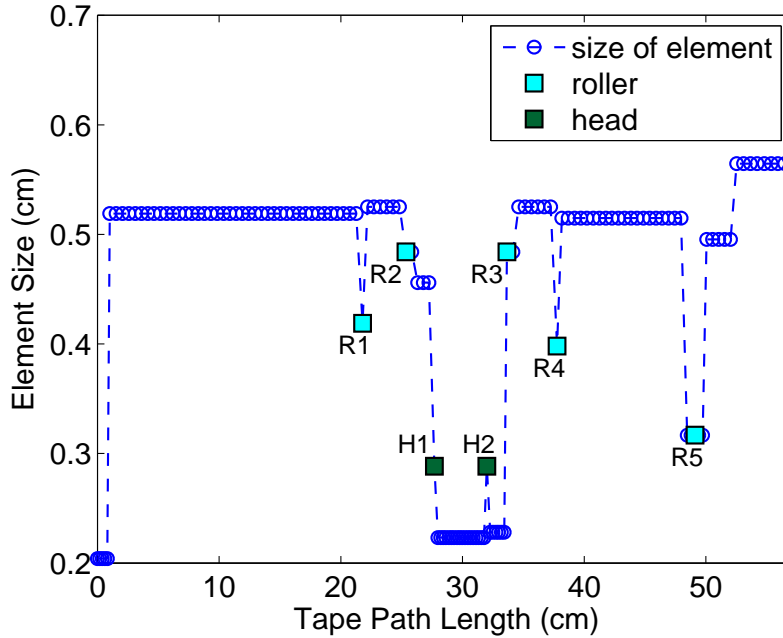


Figure 5.5: The non-uniform mesh contains 130 elements.

error between the non-uniform mesh of 130 elements and the uniform mesh of 200 elements is 1.96×10^{-7} m (not shown in Fig. 5.4).

Simulation results of the displacement at each node in the path as a function of time and position are shown in Fig. 5.6. Here, the tape is winding at a velocity of 5.4 m/sec with a tension of 1 N. The beginning and end of the tape path is at the tangential points of the source reel and the take-up reel, respectively. In this mesh configuration, the size of the element near head H2 is 0.0029 m. The simulated LTMDs w_h at the head, w_u at an upstream location, and w_d at a downstream location are illustrated in Fig. 5.7. Since the tape runs in both forward and reverse directions, the

distances between the head and the upstream and downstream locations are the same to create symmetry. To avoid including other components besides head H2 in the tape span between the upstream and downstream location, the number of elements between the head and the upstream and downstream locations is limited by the distance between head H2 and the nearest roller or head H1. In our tape path configuration, roller R3 is the nearest component to head H2 and the number of elements between them is 6.

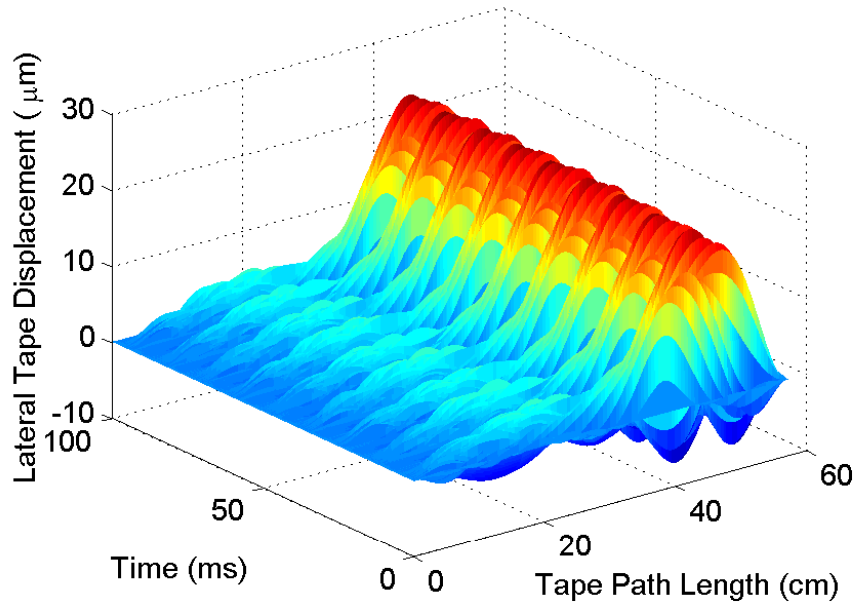


Figure 5.6: Lateral displacements of the entire tape span for a duration of 0.1 seconds.

5.4.2 Simulation of a Short Segment of Tape

Solving the partial differential equation of the short segment of tape near the head requires the LTMDs and the first derivative of the LTMD at each end of the segment in the spatial-domain. Hence, the LTMDs of two adjacent elements at both ends of the tape path are needed. The spatial derivative is approximated using first-order differences

$$\frac{dw_i}{dx} = \frac{w_{i+1} - w_i}{x_{i+1} - x_i}. \quad (5.14)$$

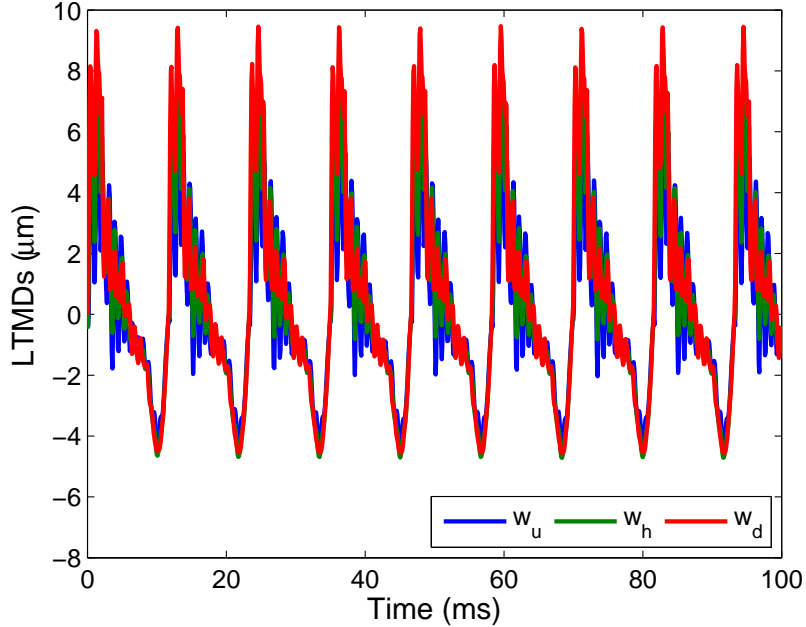


Figure 5.7: Successive LTMDs near the head.

Setting the boundary conditions to be the simulated LTMDs at the upstream and downstream locations, the partial differential equation in Equation (5.1) is solved for the short segment of the tape to yield an estimate of the LTMD at the head. In an actual tape system, lateral tape edge sensors can be placed at upstream and downstream locations to the head to measure w_u and w_d and provide real-time boundary conditions. To investigate the effects of the distance between the head and the sensor on the estimation performance, simulations are done to evaluate the estimation error when the number of elements between the head and the sensor varies. Fig. 5.8 shows that the RMS of the estimation error increases significantly when the number of elements exceeds 6 as a result of including roller R3 in the tape span. When the number of elements is less than 6, the estimation error does not vary much.

Considering that at least two edge sensors are needed to be placed on each side of the head so as to obtain the first derivative of the LTMD, we choose to place the two sensors at locations that are 2 and 4 elements away from the head. Fig. 5.9 shows the error in the estimated w_h from

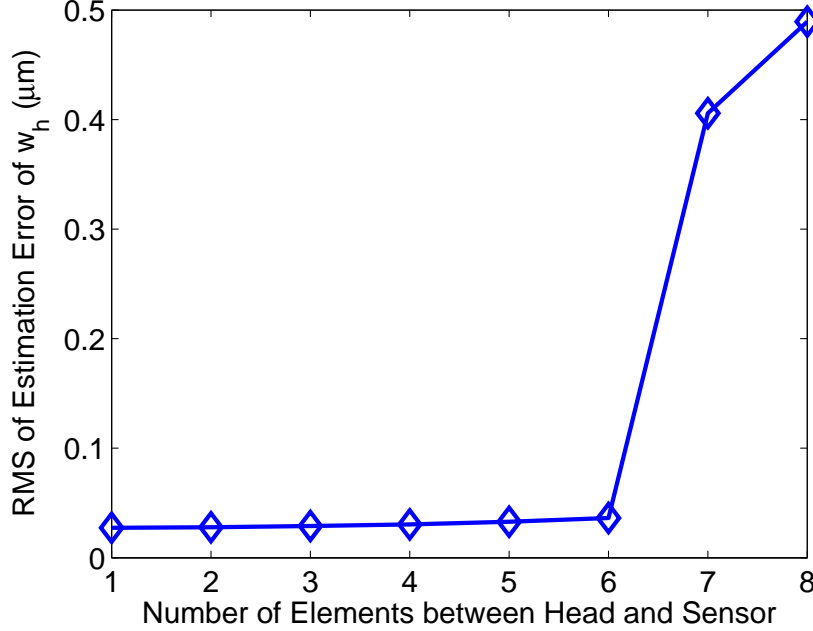


Figure 5.8: Estimation error increases significantly once the number of elements between the head and the sensor exceeds 6.

w_u and w_d in this configuration. The magnitude of the error is about 1% of the actual data.

Fig. 5.10 shows that when the boundary conditions have a 10% distortion, the magnitude of the estimation error is about 8% of the actual w_h values. When the distortion is 20%, the magnitude of the estimation error becomes about 15%.

5.4.3 Combined Feedforward/Feedback Control

The simulation results of applying the LTMD estimation algorithm to the combined feedforward/feedback control scheme (Fig. 3.6) are shown in Fig. 5.12. The PID feedback controller is enabled at 0.2 sec and replaced by the REACT controller at 0.4 sec. The RMS of position error signal is reduced from $0.96 \mu\text{m}$ to $0.61 \mu\text{m}$ with the introduction of the REACT controller. The feedforward controller is designed using the H_2 model matching method with a weighting function

$$W(z) = \frac{0.0489(z-1)^2}{z^2 - 1.956z + 0.9565}.$$

It is enabled at 0.6 sec and further reduces the RMS of the position error signal to $0.09 \mu\text{m}$.

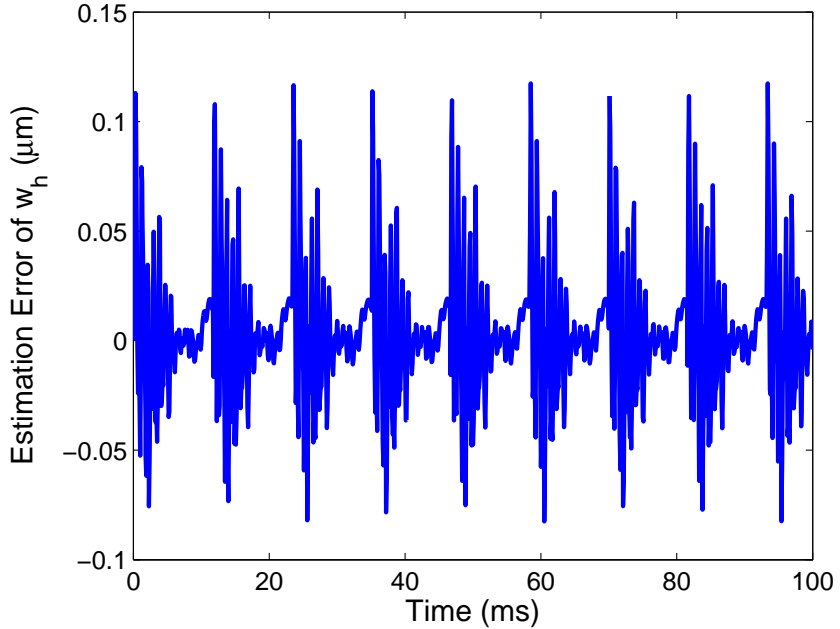


Figure 5.9: Estimation error at the head by solving the equation of motion a short segment of tape around the head.

5.5 Conclusions and Discussion

As the lateral tape motion dynamics involve nonlinearities, the linear regression method does not yield a good enough estimation of the LTMDs at the head from upstream and downstream LTMDs. Hence, the partial differential equation that describes the physical process of lateral tape motion is studied. A method is developed to calculate the LTMDs at the head using downstream and upstream LTMD information.

The lateral tape motion displacements can be measured using laser edge sensors. At least two edge sensors are needed to obtain the first derivative of the LTMD with respect to the longitudinal direction x . In the simulations, the derivative is computed using a ratio of first-order differences (Equation 5.14). The elements near the head of interest are about 0.3 cm wide and the probes of the edge sensors will need to be less than 0.3 cm. The physical size of photonic or laser edge sensors are within this range.

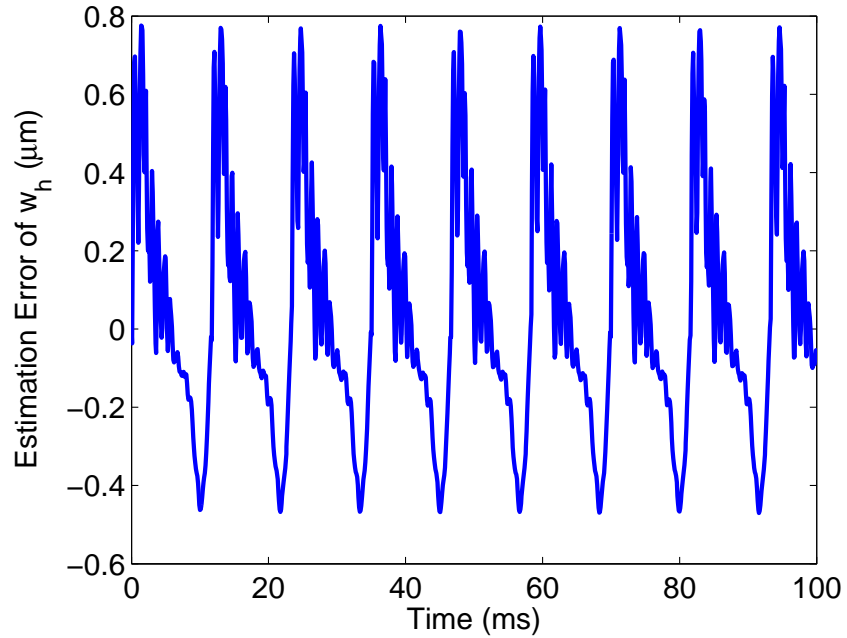


Figure 5.10: Estimation error of the LTMD at the head is about 8% of the actual data when the boundary conditions have a 10% distortion.

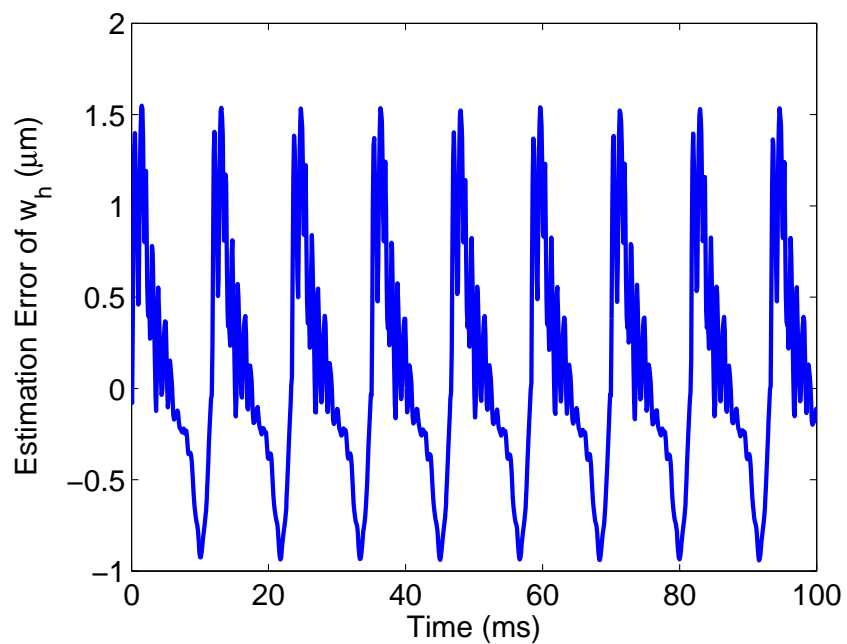


Figure 5.11: Estimation error of the LTMD at the head is about 15% of the actual data when the boundary conditions have a 20% distortion.

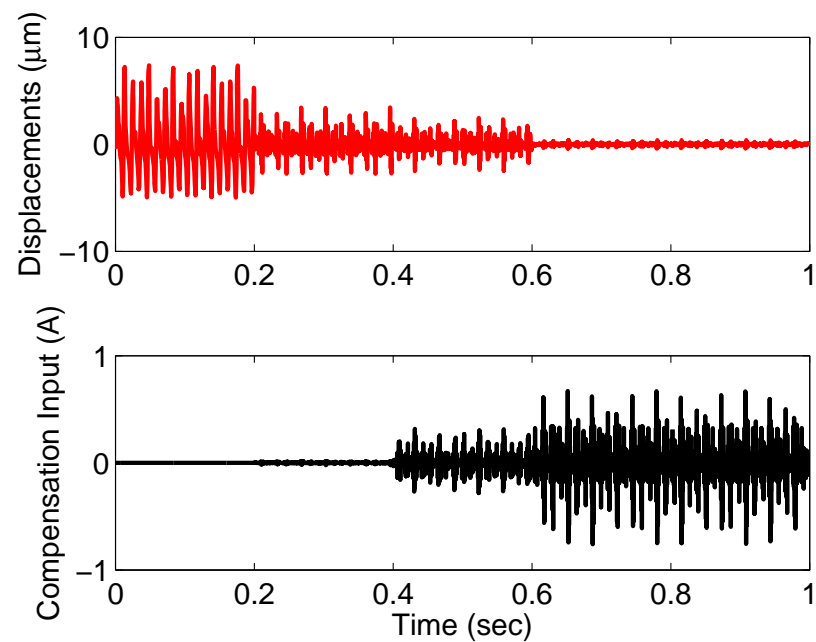


Figure 5.12: The feedforward controller designed using the H_2 model matching method is enabled at 0.4 sec. The input to the feedforward controller is the estimated LTMD at the head.

Chapter 6

Overall Conclusions and Future Work

As tape technology aims for higher data capacities to continue competing with the hard disk drive storage system, many challenging issues must be addressed. In the reel-to-reel servo system, the tension in the tape needs to be further regulated as thinner tapes are more fragile and more sensitive to tension fluctuation. In the head positioning servo system, the position error by the lateral tape motion must be further reduced to enable higher track densities and narrower track pitch. Motivated by the urgent needs of more advanced servo designs, we have performed several studies to improve the performance of the servomechanism in the tape drive.

To account for the tension errors caused by the variations in the reel radii, we developed a feedforward inspired control scheme to simultaneously address the nominal radius variation and the reel runout in Chapter 2. The designed controller can reduce the tension error caused by reel runout by three orders of magnitude.

Lateral tape motion causes displacements between the head and the data track. To account for the LTM disturbance in the position error signal, feedforward control schemes are studied and compared in Chapter 3. The H_2 model matching method surpasses the approximate dynamic inversion techniques for the following reasons:

- The feedforward control is designed to minimize the norm of the output error of the system. While the approximate dynamic inversion techniques design the controller solely based on the dynamics of the system.
- The augmented H_2 model matching method that imposes a penalty on the feedforward

control effectively constrains the size of the control input while yielding reasonable disturbance rejection. The approximate dynamic inversion techniques, however, do not have such capability.

A good estimation of the LTMDs at the head is critical to help the servo system to align the head assembly position with the desired track. In Chapter 4, linear regression method including polynomial regression is applied to estimate the LTMD at the head from upstream and downstream LTMD measurements, assuming the correlation is a linear function. Because, the lateral tape motion involves nonlinearity, the partial differential equation describing the motion of the tape in the lateral direction is studied and a methodology to solve the LTMD at the head using upstream and downstream LTMDs as the boundary conditions is developed in Chapter 5.

Combining the estimated LTMD and the feedforward controller designed through the H_2 model matching method, we demonstrate a proof of concept of applying feedforward control to address the position error caused by LTM in a tape system. To implement the control scheme in an actual tape system, there are a few practical issues worth mentioning. First, the estimation algorithm requires upstream and downstream LTMD measurements and the performance depends on the accuracy of the measurements. High-quality edge sensors are preferred for this application. Second, the size of the edge sensors limits how close two sensors can be placed side by side so as to approximate the first derivative of the LTMD. Finally, the computational complexity of the estimation algorithm and the available hardware computational resources in the tape drive are two additional factors that impact the feasibility of the algorithms on an actual tape system.

Future work include to verify the partial differential equation model in Chapter 5 using measured upstream and downstream LTMDs; to investigate the correlation of actual downstream and upstream LTMDs measurements; and to implement the algorithm in an actual tape system.

Bibliography

- [1] Matlab, Simulation and Model-Design Software Package. The MathWorks, Inc., Natick, MA.
- [2] A. Argumedo, D. Berman, R. Biskeborn, R. Cideciyan, E. Eleftheriou, W. Haberle, D. Hellman, R. Hutchins, W. Imaino, J. Jelitto, K. Judd, P. Jubert, M. Lantz, G. McClelland, T. Mittelholzer, C. Narayan, S. Olcer, and P. Seger. Scaling Tape-recording Areal Densities to 100 Gb/in^2 . *IBM J. Research and Development*, 52(4.5):513–527, July 2008.
- [3] M. Baumgart and L. Pao. Robust Control of Nonlinear Web-winding Systems with and without Tension Sensors. *ASME J. Dynamic Systems, Measurement, and Control*, 129(1):41–55, January 2007.
- [4] M. Bodson, J. Jensen, and S. Douglas. Active Noise Control for Periodic Disturbances. *IEEE Trans. Control Systems Technology*, 9(1):200–205, January 2001.
- [5] M. Brake. Lateral Vibration of Moving Media with Frictional Contact and Nonlinear Guides. PhD thesis, Carnegie Mellon University, 2007.
- [6] R. de Callafon and C. Kinney. Robust Estimation and Adaptive Controller Tuning for Variance Minimization in Servo Systems. *JSME J. Advanced Mechanical Design, Systems, and Manufacturing*, 4(1):130–142, January 2010.
- [7] John Doyle, Bruce Francis, and Allen Tannenbaum. Feedback Control Theory. Macmillan, 1992.
- [8] G. Franklin, J. Powell, and M. Workman. Digital Control of Dynamic Systems. Prentice Hall, 3rd edition, 1998.
- [9] S. Garimella and K. Srinivasan. Application of Iterative Learning Control to Coil-to-Coil Control in Rolling. *IEEE Trans. Control Systems Technology*, 6(2):281–293, March 1998.
- [10] M. Green and D. Limebeer. Linear Robust Control. Prentice Hall, 1995.
- [11] A. Hazell. Discrete-time Optimal Preview Control. PhD thesis, University of London, 2008.
- [12] Information Storage Industry Consortium (INSIC). International Magnetic Tape Storage Roadmap 2012. Technical report, INSIC, San Diego, 2012.
- [13] J. Jose, R. Taylor, R. de Callafon, and F. Talke. Characterization of Lateral Tape Motion and Disturbances in the Servo Position Error Signal of a Linear Tape Drive. *Tribology International*, 38(6-7):625–632, June-July 2005.

- [14] V. Kartik. In-plane and Transverse Vibration of Axially-Moving Media with Advanced Guiding and Actuation Elements. PhD thesis, Carnegie Mellon University, 2006.
- [15] V. Kartik, A. Pantazi, and M. Lantz. Track-following High Frequency Lateral Motion of Flexible Magnetic Media with Sub-100 nm Positioning Error. IEEE Transactions on Magnetics, 47(7):1868–1873, July 2011.
- [16] G. Liu and S. Quek. The Finite Element Method: A Practical Course. Butterworth-Heinemann, 1st edition, 2003.
- [17] D. Logan. A First Course in The Finite Element Method. Cengage Learning, 1st edition, 2011.
- [18] Y. Lu. Advanced Control for Tape Transport. PhD thesis, Carnegie Mellon University, 2002.
- [19] Y. Lu and W. Messner. Robust Servo Design for Tape Transport. In Proc. IEEE International Conference on Control Applications, pages 1014–1019, September 2001.
- [20] P. Mathur and W. Messner. Controller Development for a Prototype High-Speed Low-Tension Tape Transport. IEEE Trans. Control Systems Technology, 6(4):534–542, July 1998.
- [21] K. Ono. Lateral Motion of an Axially Moving Tape on a Cylindrical Guide Surface. ASME J. Applied Mechanics, 46:905–912, December 1979.
- [22] A. Oppenheim, A. Willsky, and S. Nawab. Signals and Systems. Prentice Hall, 2nd edition, 1996.
- [23] A. Pantazi. Lateral Tape Motion and Control Systems Design in Tape Storage. In E. Eleftheriou and S. Moheimani, editors, Control Technologies for Emerging Micro and Nanoscale Systems. Springer-Verlag Heidelberg, 2011.
- [24] A. Pantazi, J. Jelitto, N. Bui, and E. Eleftheriou. Track-following in Tape Storage: Lateral Tape Motion and Control. Mechatronics, 22(3):361–367, April 2012.
- [25] B. Raeymaekers and F. Talke. Lateral Motion of an Axially Moving Tape on a Cylindrical Guide Surface. ASME J. Applied Mechanics, 74(6):1053–1056, 2007.
- [26] B. Raeymaekers and F. Talke. Measurement and Sources of Lateral Tape Motion: A Review. ASME J. Tribology-Transactions, 131:65–68, January 2009.
- [27] B. Raeymaekers and F. Talke. Measurement and Sources of Lateral Tape Motion: A Review. Tribology International, 42(4):609–614, May 2009.
- [28] K. Åström, P. Hagander, and J. Sternby. Zeros of Sampled-data Systems. Automatica, 20(1):31–38, January 1984.
- [29] J. Reddy. Introduction To The Finite Element Method. McGraw-Hill College, 1st edition, 2004.
- [30] B. Rigney. Adaptive Settle-Optimal Control of Servomechanisms. PhD thesis, Univ. of Colorado Boulder, 2008.

- [31] S. Sastry and M. Bodson. *Adaptive Control, Stability, Convergence, and Robustness*. Prentice Hall, 1989.
- [32] J. Shelton and K. Reid. Lateral Dynamics of an Idealized Moving Web. *ASME J. Dynamic Systems, Measurement, and Control*, 93(1):187–192, September 1971.
- [33] J. Shelton and K. Reid. Lateral Dynamics of an Real Moving Web. *ASME J. Dynamic Systems, Measurement, and Control*, 93(1):180–186, September 1971.
- [34] R. Taylor and F. Talke. High Frequency Lateral Tape Motion and the Dynamics of Tape Edge Contact. *Microsystem Technologies*, 11(8):1166–1170, January 2005.
- [35] R. Taylor and F. Talke. Investigation of Roller Interactions with Flexible Tape Medium. *Tribology International*, 38(5):599–605, June 2005.
- [36] M. Tomizuka. Zero Phase Error Tracking Algorithm for Digital Control. *ASME J. Dynamics, System, Measurement, and Control*, 109:1–6, March 1987.
- [37] David Watkins. *Fundamentals of Matrix Computations*. Wiley, 2010.
- [38] J. Wen and B. Potsaid. An Experiment Study of a High Performance Motion Control System. In *Proc. American Control Conference*, pages 5158–5163, June 2004.
- [39] J. Wickert and M. Brake. Tape Path Guiding Simulation Distribution. Technical report, INSIC Report, 2007.
- [40] E. Wilson, I. Farhoomand, and K. Bathe. Nonlinear Dynamic Analysis of Complex Structures. *Earthquake Engineering and Structure Dynamics*, 1(3):241–252, 1972.
- [41] L. Xia and W. Messner. Active Tape Steering Control System. *Mechatronics*, 20(1):6–11, February 2010.
- [42] Y. Xu, M. Mathelin, and D. Knittel. Adaptive Rejection of Quasi-periodic Tension Disturbances in the Unwinding of a Non-Circular Roll. In *Proc. American Control Conference*, pages 4009–4014, May 2002.
- [43] H. Zhong and L. Pao. Feedforward control to attenuate tension error in time-varying tape systems. In *Proc. American Control Conference*, pages 105–110, June 2008.
- [44] H. Zhong and L. Pao. Regulating Web Tension in Tape Systems with Time-varying Radii. In *Proc. American Control Conference*, pages 198–203, June 2009.
- [45] H. Zhong and L. Pao. Combined Feedforward/Feedback Control for Tape Head Track-Following Servo System. In *Proc. IFAC World Congress*, pages 4040–4045, August 2011.
- [46] H. Zhong and L. Pao. H_2 Model Matching Feedforward Control for Tape Head Positioning Servo Systems. In *Proc. American Control Conference*, pages 4504–4509, June 2013.
- [47] H. Zhong, L. Pao, and R. de Callafon. Feedforward Control for Disturbance Rejection: Model Matching and Other Methods. In *Proc. Chinese Control and Decision Conference*, pages 3528–3533, May 2012.
- [48] H. Zhong, L. Pao, and V. Kulkarni. Adaptive Control For Rejecting Disturbances with Time-Varying Frequencies in Tape Systems. In *Proc. American Control Conference*, pages 533–538, June 2005.